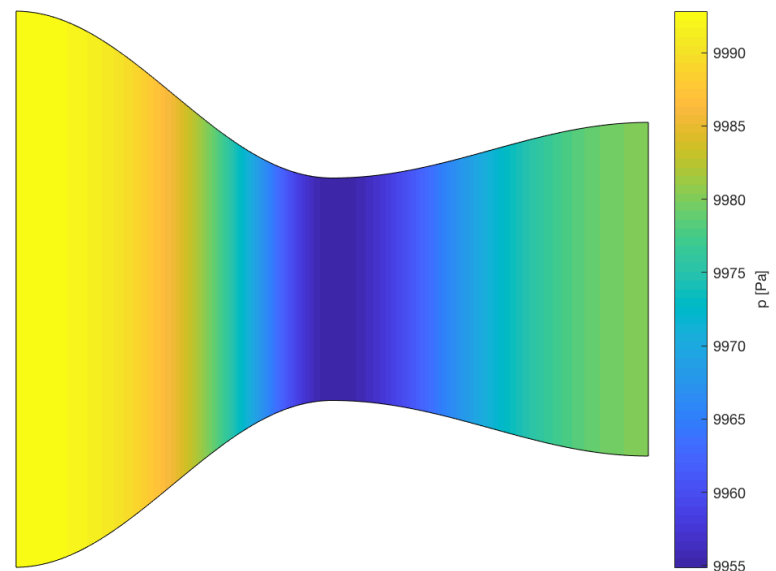Anna Helene Symington Hansen

Modeling and Simulation of Respiratory flow

Master's thesis in Energy and Environmental Engineering
July 2019

Master's thesis

NTNU
Norwegian University of
Science and Technology

Anna Helene Symington Hansen

Modeling and Simulation of Respiratory flow

NTNU

Norwegian University of
Science and Technology

Norwegian University
of Science and Technology

Department of Energy
and Process Engineering

EPT-M-2019-

MASTER THESIS

for

Student Anna Helene Symington Hansen

Spring 2019

Modeling and Simulation of Respiratory Flow
Modellering og simulering av respiratorisk strømning

Background and objective

Since respiration supplies the lungs with oxygen and removes carbon dioxide, it has been the prerequisite of human and animal life. Understanding respiration has been key for investigating respiratory diseases.

The goal of the project is to model and simulate respiratory flow using simplifying assumptions.

The following tasks are to be considered:

1. to get a basic understanding of respiratory flow, its modeling and simulation,
2. to devise a simplified model of respiratory flow including initial and boundary conditions,
3. to implement the simplified model of respiratory flow,
4. to compare the simulation results with the literature.

-- ” --

Within 14 days of receiving the written text on the master thesis, the candidate shall submit a research plan for his project to the department.

When the thesis is evaluated, emphasis is put on processing of the results, and that they are presented in tabular and/or graphic form in a clear manner, and that they are analyzed carefully.

The thesis should be formulated as a research report with summary both in English and Norwegian, conclusion, literature references, table of contents etc. During the preparation of the text, the candidate should make an effort to produce a well-structured and easily readable report. In order to ease the evaluation of the thesis, it is important that the cross-references are correct. In the making of the report, strong emphasis should be placed on both a thorough discussion of the results and an orderly presentation.

The candidate is requested to initiate and keep close contact with his/her academic supervisor(s) throughout the working period. The candidate must follow the rules and regulations of NTNU as well as passive directions given by the Department of Energy and Process Engineering.

Risk assessment of the candidate's work shall be carried out according to the department's procedures. The risk assessment must be documented and included as part of the final report. Events related to the candidate's work adversely affecting the health, safety or security, must be documented and included as part of the final report. If the documentation on risk assessment represents a large number of pages, the full version is to be submitted electronically to the supervisor and an excerpt is included in the report.

Pursuant to "Regulations concerning the supplementary provisions to the technology study program/Master of Science" at NTNU §20, the Department reserves the permission to utilize all the results and data for teaching and research purposes as well as in future publications.

The final report is to be submitted digitally in DAIM. An executive summary of the thesis including title, student's name, supervisor's name, year, department name, and NTNU's logo and name, shall be submitted to the department as a separate pdf file. Based on an agreement with the supervisor, the final report and other material and documents may be given to the supervisor in digital format.

☐ Work to be done in lab (Water power lab, Fluids engineering lab, Thermal engineering lab)
☐ Field work

Department of Energy and Process Engineering, 04. February 2019

_____
Bernhard Müller
Academic Supervisor

Abstract

In this master thesis, a simplified model for simulation of respiratory flow with initial and boundary conditions is derived, implemented, tested and discussed. Both steady and unsteady flow simulations are performed using corresponding boundary conditions.

The main simplifications and assumptions behind the model are the use of a simplified geometry, in this case a converging-diverging nozzle (CDN), the quasi-one-dimensional approach, and the assumptions of inviscid flow and perfect gas.

The governing equations of the model are the compressible quasi-1D Euler equations. The numerical model prescribes initial stagnation conditions and steady boundary conditions pertaining to the pressure relation driving the flow. The relation between the pulmonary pressure in the lungs and the surrounding ambient pressure is modeled by the relation between the nozzle exit pressure and the stagnation pressure. Oscillating flow is governed by unsteady boundary conditions modeling the respiratory cycle. A sinusoidal time-varying stagnation pressure condition describing the lungs is implemented.

The model is discretized using the finite volume method (FVM). For simulation, both first order and higher order discretization methods are implemented: the first order explicit Euler method with the Rusanov scheme and the third order SSP Runge-Kutta method with second order MUSCL extrapolation of the conservative variables.

The model with steady boundaries is tested for two cases applied to a CDN, one with transonic flow conditions and one with low Mach number flow conditions. The unsteady boundaries are tested for a constant cross-sectional area with low Mach number flow.

Results show that the model yields the expected flow phenomena for steady flow simulations in a CDN and may be verified against the exact analytical solution. Accurate results are obtained, especially for the low Mach number flow, with relative errors under 1% when compared with the exact analytical solution. For oscillating flow, the results show significant agreement with the expected flow features.

Verification of the model applied to steady transonic and low Mach number flow with a varying cross-sectional area is achieved by comparison to the exact analytical solution. However, some spatial resolution issues and stability issues are encountered. The proposed model simulates oscillating flow in satisfactory accordance with the reviewed literature. More testing is nevertheless required to obtain a verified solution for unsteady low Mach number flow, although this is dependent upon improving the complexity of the model.

For further improvement of the model, it is advised that one look into well-balanced methods for discretization of the source term to potentially resolve the encountered spatial resolution and stability issues. Furthermore, it is suggested to consider and compare different types of oscillating boundary conditions. Additionally, the model may be improved upon by taking transport phenomena and a more complex geometry into account, yielding a more comprehensive and realistic model for respiratory flow.

ii

Sammendrag

I denne masteroppgaven presenteres, implementeres, testes og diskuteres en forenklet modell for å simulere respiratorisk strømning. Initialbetingelser og grensebetingelser for både stabile og ustabile strømninger er lagt frem. Simuleringer blir gjennomført for både stabile og oscillerende strømninger med tilhørende grensebetingelser.

De viktigste forenklingene og antakelsene bak modellen er bruken av en forenklet geometri, i dette tilfellet en konvergerende-divergerende dyse (CDN), den kvasi-endimensjonale tilnærmingen, og antagelsene om ikke-viskøs strømning og ideell gass.

Modellen bygger på de kompressible kvasi-1D Euler-ligningene. Den numeriske modellen består av stagnasjons initialbetingelser og stabile grensebetingelser knyttet til trykkforholdet som driver strømningen. Forholdet mellom lungetrykket og omgivelsestrykket er modellert av forholdet mellom trykket ved utgangen til dysen og stagnasjonstrykket. Oscillerende strømning styres av ustabile grensebetingelser som modellerer den respiratoriske syklusen. Det er innført en sinusformet, tidsvarierende, stagnasjonstrykks grensebetingelse som representerer lungene.

Diskretisering av modellen er gjort ved hjelp av volummetoden (FVM). For å simulere modellen er både første ordens og hørere ordens diskretiserings-metoder implementert: første ordens eksplisitt Euler-metoden med Rusanov-metoden, og tredje ordens SSP Runge-Kutta-metoden med MUSCL ekstrapolering av de konservative variablene.

De stabile grensebetingelsene er testet for to caser på en konvergerende-divergerende dyse: en med transsonisk strømning, og en med strømning med lave Mach-tall. De ustabile grensebetingelsene er testet for et konstant areal med strømning med lave Mach-tall.

Resultatene viser de forventede strømningsforholdene for stabil strømning i en konvergerende-divergerende dyse, og modellen kan derfor verifiseres ved hjelp av den eksakte analytiske løsningen. Presise resultater er oppnådd, spesielt for strømning med lave Mach-tall, med relative feil på under 1% i forhold til den eksakte løsningen. For oscillerende strømning viser resultatene høy grad av overensstemmelse med de forventede strømningsforholdene.

Verifikasjon av modellen for transsonisk strømning og strømning med lave Mach-tall i en CDN er oppnådd ved sammenligning med den eksakte analytiske løsningen. Imidlertid støter modellen på noen problemer knyttet til stabilitet og romdiskretisering. Den foreslåtte modellen for oscillerende strømning viser god overensstemmelse med den gjennomgåtte litteraturen. Dog er det behov for en mer kompleks modell og ytterligere testing for å oppnå en verifisering av modellen for ustabil strømning med lave Mach-tall.

For videre forbedring av modellen tilrådes det å undersøke "well-balanced" metoder for diskretisering av kildeleddet som potensielt kan løse stabilitets- og rom-resolusjonsproblemene. Det er anbefalt å undersøke forskjellige typer oscillerende grensebetingelser. I tillegg kan det være hensiktsmessig å utvide modellen ved å ta hensyn til transportfenomener og en mer kompleks geometri, slik at modellen blir mer allsidig og realistisk.
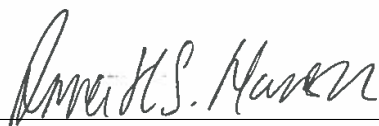
iv

Preface

The figure on the cover of this thesis shows the pressure distribution at steady state in a converging-diverging nozzle(CDN) with low Mach number flow. The pressure distribution in the nozzle is obtained from simulations performed using the proposed model for respiratory flow. The shape of the nozzle is the main simplified geometry implemented in the model presented in this work. The low Mach number is in keeping with the flow regime of respiratory flow. A rarefaction wave has traveled to the left and the flow is now at steady state after having simulated inspiration.

This master thesis marks the completion of my Master of Science in Energy and Environmental Engineering at the Norwegian University of Science and Technology (NTNU), Department of Energy and Process Engineering.

The decision to write about computational modeling of biofluid flow originated from a great interest in and appreciation for computational fluid dynamics (CFD) and a personal curiosity regarding the interface between medicine and technology.

I would like to express my deepest gratitude to my supervisor Bernhard Müller. His thoughtful and precise academic advice, as well as his honest and can-do approach, has been of great influence during this work.

Trondheim, July, 2019

Anna Helene Symington Hansen

Table of Contents

List of Tables

List of Figures

Nomenclature

Symbols

α	Angle
Δt	Temporal step size
Δx	Spatial step size
γ	Ratio of specific heats
ω	Angular frequency
Ω_j	Finite volume cell j
∂p	Pressure amplitude
ρ	Density
σ	Stress
τ	Viscous stress
$\mathbf{F(U)}$	Flux function
$\mathbf{S(U)}$	Vector of source terms
$\mathbf{U}$	Vector of conservative variables
$\mathbf{V}$	Vector of primitive variables
$\vec{n}$	Normal unit vector
$\vec{P}$	Pressure force
$\vec{u}$	Velocity vector
A	Cross-sectional area
C	Courant number
c	Speed of sound
c_p	Specific heat at constant pressure
E	Specific total energy

e	Specific internal energy
$E(x)$	Error of variable x
f	Frequency
$F_{j+\frac{1}{2}}$	Numerical flux
g	Gravitational acceleration
H	Total enthalpy
k	Grid convergence rate
M	Mach number
NJ	Number of cells in x-direction
NT	Number of time steps
p	Pressure
R	Specific gas constant
r	Radius
$R(U)$	Residual
$RE(x)$	Relative error of variable x
SR	Spectral radius
T	Temperature
t	Time
t_{end}	Numerical end time
U	Scalar conserved variable
u	Velocity

Abbreviations

CDN   Converging-diverging nozzle

CFD   Computational fluid dynamics

CT   Computed Tomography

FVM   Finite volume method

MUSCL Monotone   upwind   scheme   for conservation laws

ODE   Ordinary differential equation

OSA   Obstructive sleep apnea

PDE   Partial differential equation

RK   Runge-Kutta

SSP   Strong stability-preserving

TVD   Total variation diminishing

1 | Introduction

1.1 Motivation and background

Human life is dependent on respiratory flow. Successful treatment of respiratory diseases and disorders is therefore of great importance. To better understand the causes and symptoms of respiratory diseases, computational modeling of the flow in the human airways can help determine the flow features found in patients suffering from respiratory diseases and disorders. Furthermore, computational fluid dynamics (CFD) methods applied to the respiratory flow of a specific patient may help to better evaluate the various treatment options available.

Application of CFD to further research and treat respiratory diseases and disorders is dependent on a physical understanding of the respiratory system and a comprehensive understanding of the causes and symptoms of different respiratory issues. A review of the respiratory anatomy is thus presented, and one of the most common respiratory disorders, obstructive sleep apnea (OSA), its causes, symptoms, and prevalence are discussed.

1.1.1 Anatomy of the human respiratory system

The main purpose of the respiratory system is to provide the cardiovascular system with oxygen and remove carbon dioxide through gas exchange. Secondary functions of the respiratory organs include filtering, humidifying and warming inhaled air to protect the organs, and generation of sound by the larynx. The gas exchange happens on the surface area of all blind-ending pulmonary alveoli, which account for a significant part of the lungs. Inhaled air travels through the conducting airways to reach the pulmonary alveoli. The conducting airways consist of the upper and lower respiratory systems. The upper airways, mainly contained in the head, include the nose and nasal cavity, the paranasal sinuses and the pharynx. The lower airways, contained in the neck and thorax, consist of the larynx, the trachea and the bronchial tree [12]. Figure 1.1 depicts the main components of the respiratory system.

Breathing, or pulmonary ventilation, is controlled by the muscles of inhalation: the diaphragm and the external intercostal muscles, see figure 1.2. During inhalation the aforementioned muscles contract. When the diaphragm contracts, it descends causing the thoracic volume to increase. Movement of the rib cage also causes volume changes of the thorax. When the volume increases, the pressure drops and air flows into the lungs. During exhalation, the muscles relax and the lungs contract. Due to the decrease in volume, the pulmonary pressure rises and air is expelled. The inverse relationship between the volume and the pressure of a gas is stated by the Boyle-Mariotte law dating back to the 17th century.

When analyzing respiratory flow, the tidal volume and the frequency of breath are used to describe the inflow of air and the cyclic behavior of the flow. The tidal volume
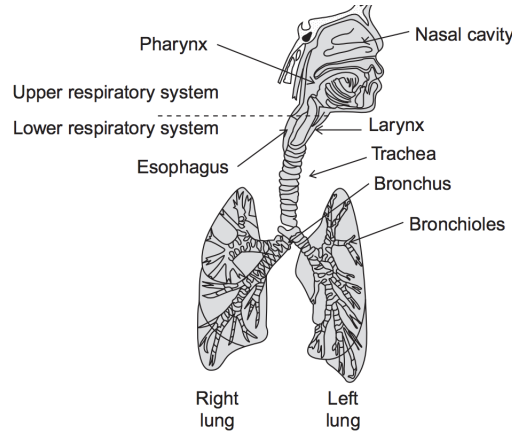
Figure 1.1: Anatomical arrangement of the human respiratory system [43].
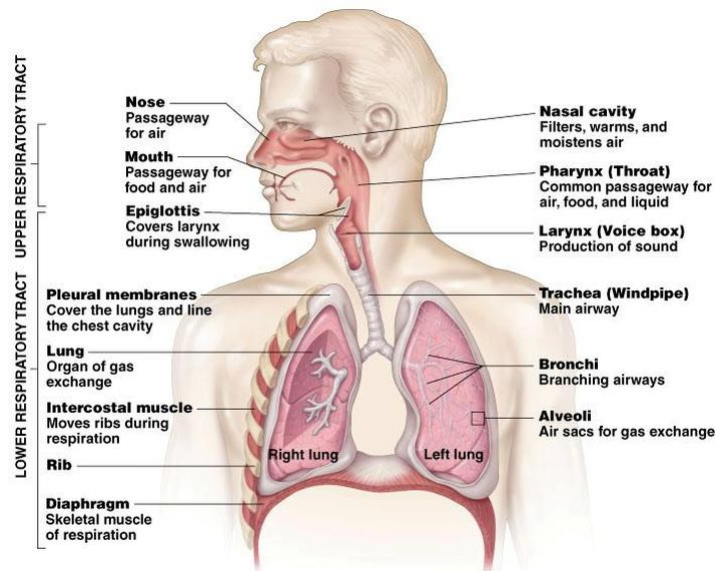
Figure 1.2: Detailed anatomy of the human respiratory system.
Copyright ©2003 Pearson Education, Inc. publishing as Benjamin Cummings [34].

is the volume of air inhaled during each breathing cycle, typically averaged as 500 ml per cycle. The breathing frequency refers to the number of respiratory cycles per minutes. Under normal breathing conditions, the frequency is assumed to be 12-15 cycles per minute. However, under extreme conditions such as highly strenuous exercise, the frequency of breath may reach 50 cycles per minute, moving up towards 4.8 l of air during one respiratory cycle [43].

For more detailed information regarding the anatomy of the respiratory system or the specific flow mechanics, the reader is referred respectively to the *Color Atlas of Human Anatomy* [12] or to the textbook *Biofluid Mechanics: An Introduction to Fluid Mechanics, Macrocirculation, and Microcirculation* [43].

1.1.2 Respiratory diseases and disorders

One of the most common respiratory disorders is sleep apnea, the cessation of breathing during sleep. There are two types of sleep apnea: obstructive sleep apnea (OSA) and central sleep apnea. The first is the most common sleep-related breathing disorder [25]. In North America, the estimated prevalence of OSA is up to 30 percent in adult males and up to 15 percent in adult females [50][40].

During sleep, the respiratory muscles relax, causing the upper airways to narrow. Normal airway functionality allows a person to breathe continuously despite the physical narrowing during sleep. A person with unfavorable upper airway anatomy, however, may experience cessation of breathing while sleeping due to partially or fully obstructed airways. OSA is characterized by recurring full obstructions of the airways during sleep.

When the airway is fully obstructed, no air is conducted through the respiratory system, and hence no gas exchange occurs. Reopening of the airway requires the affected person to awaken, activating the respiratory muscles. Recurring episodes of apnea during the night frequently interrupts sleep and reduces sleep quality. Accordingly, the main symptoms of OSA are loud nocturnal snoring, fatigue, and daytime sleepiness [26].

The most common cause of OSA is anatomic, and hence genetically determined. Patients often have a small unfavorable upper airway and surrounding bone structure. The main clinical risk factors for developing OSA are obesity, advancing age and male gender.

Treatment of OSA ranges from adjusted lifestyle choices and sleep positions to nightly breathing equipment, and in some cases surgery. The most effective treatment is the use of a medical device called continuous positive airway pressure (CPAP), designed to keep the airways open during sleep by increasing the airway pressure. When nonsurgical treatment, such as the use of CPAP or dental devices, does not suffice, surgery may be considered. Surgical procedures can reshape the upper airway structure or surgically reposition bones and soft tissue in the respiratory system thus improving upon unfavorable airway anatomy.

Other common respiratory disorders include central sleep apnea, asthma, and chronic obstructive pulmonary disease. Additionally, the inhalation of toxins and the layering of toxins in the respiratory system are also considered common respiratory diseases.

The computational modeling of respiratory flow may help to better understand the causes, symptoms and treatment options for different respiratory diseases and disorders.

1.1.3 Computational modeling of respiratory flow

Biofluid mechanics, also referred to as biofluid dynamics, is considered the discipline of biomedical engineering. This is a discipline under fluid mechanics concerning biological fluid systems such as the cardiovascular system and the respiratory system. Biofluid dynamics is a large and growing field of research. Using computational fluid dynamics (CFD) models for biofluids leads to a better understanding of the effects of various diseases on biofluid flow, the need for surgical treatment and the effects of surgery, and the transportation of toxins as well as medication in biofluid flow.

To introduce the ideas behind the computational modeling of respiratory flow, research detailing different numerical approaches and models are discussed. Firstly, respiratory models do not necessarily take the entire respiratory system into account; many models focus either on the nasal cavity or the lungs. The simulations may be performed using

numerical methods or CFD software, and the flow is often assumed incompressible. Some models only look at steady flow, that is only inspiration or expiration, while others consider unsteady flow, simulating the breathing cycle.

First off, studies of numerical models pertaining only to the nasal cavity are presented. Hörschler et al. in *Numerical simulation of the flow field in a model of the nasal cavity* 2003 [19], present a model based on steady flow simulation of the 3D compressible Navier-Stokes equations solved with an advective upstream splitting (AUSM) based method with a five-stage Runge-Kutta time-stepping method. At the outflow boundary, a non-reflecting boundary condition is applied, and the static pressure level is prescribed. The obtained results show good agreement with experimental data, and it is concluded by the authors that the model is a sound basis for further development of a flow solver for nasal cavities for various geometries.

Dealing with the complex geometry of the nasal cavity raises a number of issues. Some research is therefore focused on using lattice Boltzmann methods to deal with the complexity. Two examples of models using incompressible lattice Boltzmann methods are to follow.

Finck et al. in *Simulation of nasal flow by lattice Boltzmann methods* 2006 [9], compare solutions obtained using a lattice Boltzmann method for solving the incompressible steady flow at the inspiration and expiration phases with results obtained from conventional incompressible Navies-Stokes solvers. The authors state several found advantages of using lattice Boltzmann methods for biomedical flow with complex geometries, such as fast grid generation, flexibility for implementing complex boundary conditions, and additional transport equations. The geometries used in the study are obtained from Computed Tomography (CT) images.

Another example of models using lattice Boltzmann methods is Eitel et al. in *Numerical Simulation of Nasal Cavity flow Based on a Lattice-Boltzmann Method* 2010 [6]. The focus of the work is to analyze the flow field at steady inspiration and expiration. The geometry used is again extracted from CT images. Results show strong vortical structures yielding vortices along the throat for inspiration and only slight vortical flow for expiration.

Simulation software may also be used in respiratory flow simulation. An example is found in Riazuddion et al. in *Numerical Study of Inspiratory and Expiratory Flow in a Human Nasal Cavity* 2011 [42], where steady incompressible inspiratory and expiratory flow is simulated using the commercial CFD solver FLUENT. The geometry is extracted from CT images of one specific patient. The goal of the study is to analyze flow phenomena not seen when using rhinomanometry due to the complex geometries of the nasal cavity. The study finds that flow resistance is greater for inspiratory flow. Turbulence intensity is found to be more predominant for expiratory flow. Vortex formation, however, is only observed during inspiration, similar to the finding from Eitel et al. 2010 [6]. The reader interested in the phenomena of flow resistance is referred to Ishikawa et al. 2006 [21].

So far, all examples of respiratory flow models from literature have concerned only steady flow, that is flow with steady boundary conditions. However, respiratory flow is cyclic and unsteady, containing both inspiration and expiration. To fully understand the respiratory flow unsteady models must be considered.

Still only considering the nasal cavity, Kessler et al. present an unsteady incompressible flow simulation in *Simulation of the Flow in a Human Nose* 2010 [22]. The geometry is extracted from a series of CT images of one patient, and a numerical grid is obtained.

The simulations are performed using the DLR (The German Aerospace Center) code THETA for low Mach numbers. The flow is assumed laminar, similar to the work by Finck et al. 2007 [9], Eitel et al. 2010 [6], and Hörschler et al. 2003 [19], and thus no turbulence model is activated in the code. The results show steady flow regimes in the narrow part of the nasal cavity, whereas highly unsteady flow is observed after the cavity conjunction.

As seen, the presented models for nasal cavity flow are mostly laminar and steady. A study on the assumption of these two properties is found in Hörschler, Schörder et al. in *On the assumption of steadiness of nasal cavity flow* 2010 [20]. The study finds a clear hysteresis for the steady state and the unsteady state solutions, and that major differences of the models occur at increasing mass flux. However, for decreasing mass flux smaller discrepancies are observed. The unsteady results differ the most from the steady state solution at the transition from inspiration to expiration, that is for small mass fluxes.

Moving on from models that focus solely on the nasal cavity, two examples of models for the central airways are presented. Both models are part of studies in which the goal is to improve artificial lung ventilation.

Frederich et al. in *Towards Numerical Simulation and Analysis of the Flow in Central Airways* 2010 [10], present results for unsteady central airway flow simulated with the Immersed Boundary method together with the flow solver ELAN, in-house at TU Berlin. The geometry is extracted from CT images. A pressure boundary condition is applied to the lung surface. Additionally, the change in flow direction during the respiratory cycle is modeled by a sinusoidal curve for the temporal volume flux. The study provides results for both steady and unsteady simulation. It concludes that a volume flux, which is found appropriate for modeling tidal breathing, and a laminar inlet profile are reasonable boundary conditions.

Further along with respect to models for artificial lung ventilation, Krenkel et al. in *Protective Artificial Lung Ventilation: Impact of an Endotracheal tube on the Flow in a Generic Traches* 2010 [28], investigate the effect of an endotracheal tube on the flow in the trachea. The study presents results for steady incompressible tracheal flow with endotracheal tubes simulated with the DLR THETA code, cf. Kessler et al. 2010 [22], which are compared with experimental data. The study concludes that it is necessary to model both the tube ending and the bending of the tube which influences the development of secondary flows in the central airways.

It is clear, that also for central airways, research is done on both steady and unsteady flow. This division continues when looking at studies of models pertaining to the lower respiratory system.

An early study of the flow phenomena in the lungs is found in *Numerical simulation of respiratory flow patterns within human lung* by Calay et al. 2002 [2]. The study focuses on unsteady flow through the central and lower airways based on a 3D model of the trachea and bronchi. Unsteady flow simulations are carried out for normal breathing conditions and for maximal exercise conditions. The results for both conditions are found to be strongly dependent on both the convective and the viscous effect. The authors argue that the lack of information regarding the time-dependent pressure variation in the lung prevents the use of a pressure boundary condition. The variation of the tidal volume, however, may be measured. This leads the study to implement a sinusoidal velocity boundary condition at the inflow/outflow boundary. Nevertheless, some researchers such as Lee et al. in *Unsteady flow characteristics through a human nasal airway* 2010 [30],

tend toward using a varying pressure boundary condition.

Freitas and Schröder in *Numerical investigation of the three-dimensional flow in a human lung model* 2008 [11], perform steady state simulations of the airways spanning from the trachea to the sixth generation of the bronchial tree. Results computed using a lattice Boltzmann method are compared to and validated by experimental data. Findings show the impact of the asymmetry of the lung geometry on the air exchange mechanism of respiratory flow.

The numerical models discussed so far show the importance of the respiratory geometry and the impact on the flow features. The specific effects of different geometries on the respiratory flow are detailed in the next paragraphs.

Simulation of respiratory flow using CFD is leading to a more comprehensive understanding of the effect of the geometry of the respiratory system on the flow. Diseases such as OSA are often present due to the individual geometry of a patient's nasal configuration. Other rhinologic pathologies such as a diminished sense of smell and taste, impaired heating capabilities, and dry mucous membranes are also dependent upon the nasal geometry.

Lintermann et al. in *Fluid mechanics based classification of the respiratory efficiency of several nasal cavities* 2013 [32], investigate the effect of nasal cavity geometry on the flow, where the geometry is extracted from CT images from three individual patients. Simulations of inspiratory flow are performed using a Lattice-Boltzmann method for the different geometries. The study concludes that the geometries may be categorized as poor, medium and good due to various flow phenomena analyzed from the simulation, corresponding to an initial classification by a rhinologist.

An earlier study, *Investigation of the impact of the geometry on the nose flow* by Hörscheler et al. 2005 [18], compares numerical simulation of flow through the nasal cavities with and without turbinates, the nasal bone shelves found in the nasal cavity. The numerical method is verified using experimental results obtained from experiments performed on physical models based on CT images. The numerical results for several nasal geometries show that inspiratory flow is more sensitive to the geometry than expiratory flow, and that the lower turbinate significantly affects the flow structure, especially during inspiration.

Surgical treatment of the upper airways is often necessary when respiratory disease due to geometric issues occur. The effects of rhinosurgery may be better understood, and the decision to perform surgery may be improved, by using CFD to model the respiratory flow for specific patients.

Zachow et al. in *CFD simulation of nasal airflow: Towards treatment planning for functional rhinosurgery* 2006 [51], address the importance of computational modeling based on patient specific nasal geometries to better plan potential surgical treatment. Simulations are performed using ANSYS CFX, and turbulence is modeled by the Shear-Stress-Transport model. Findings show detailed flow resolution for the complex geometry.

A particularly common nasal geometry issue is that of a deviated septum. As a step towards using patient specific CFD simulations to determine whether a patient will benefit from septoplasty or not, Garcia et al. in *Septal deviation and nasal resistance: An investigation using virtual surgery and computational fluid dynamics* 2010 [13], present a study performing CFD simulations on models with septal deviations. The study looks at how septal deviations affect the flow resistance and finds that CFD simulations performed to predict the nasal resistance mimic in vivo observations using rhinomanometry.

Almost all literature discussed so far has used respiratory geometries extrapolated from CT images. For the interested reader, Kharat et al. in *Development of Human Airways Model for CFD Analysis* 2018 [23] discuss in detail how such geometries can be modeled based on CT scan data. On the same topic, Zwicker et al. in *Validated reconstructions of geometries of nasal cavities from CT scans* 2018 [53] discuss the automated process of obtaining patient specific geometries and how the geometries may be validated in a step toward objective analysis of nasal airflow based on CT images. Furthermore, Kim et al. in *Patient specific CFD models of nasal airflow: Overview of methods and challenges* 2013 [24] detail existing methods and specifically the challenges associated with patient specific geometries, such as standardization of the segmentation and grid generation processes. An overview of the development of the use of patient specific geometries is detailed by Lintermann and Schröder in *A Hierarchical Numerical Journey Through the Nasal Cavity: from Nose-Like Models to Real Geometries* 2017 [33].

Moving on from general simulation of respiratory flow and the generation of geometries from CT images, the transport phenomena in respiratory flow are also a field of interest. Naftali et al. in *Transport Phenomena in the Human Nasal Cavity: A Computational Model* 1998 [38] perform and present a 2D study of transport phenomena in the nasal cavity at inspiration under different ambient conditions. The findings suggest that during normal breathing frequency there is ample time for equilibration of heat and water exchange to near interalveolar conditions. Additionally, it is found that the nose can maintain this equilibrium under extreme conditions such as hot and humid or cold and dry. It is also found that abnormal blood supply or mucous generation may reduce the heat or moisture flux of inspired air.

Kleinstreuer and Zhang in *Airflow and Particle Transport in the Human Respiratory system* 2010 [27] investigate the deposition of micron particles and nanoparticles in the airways. It is found that the geometry of the airways, as well as the history of airflow fields and particle distributions, may significantly affect particle deposition in the airways. The potential harm of toxins ingested as nanoparticles is additionally discussed.

It is possible to use particle deposition in the airways to deliver pharmaceuticals. This is discussed by Engelhardt et al. in *First Steps to Develop and Validate a CFDP Model in Order to Support the Design of Nose-to-Brain Delivered Biopharmaceuticals* 2016 [7].

A look at turbulent respiratory flow which occurs during rapid inhalation, i.e. a sniff, is detailed by Celmet et al. in *Large-scale CFD simulations of the transitional and turbulent regime for the large human airway during rapid inhalation* 2016 [3]. The study is performed for the incompressible steady case using patient specific geometry and simulations done using a highly parallel finite element code solving the transient incompressible Navier-Stokes equations on unstructured meshes generated by ANSYS.

Lastly, Oeltze-Jafra et al. in *Generation and Visual Exploration for Medical Flow Data: Survey, Research Trends and Future Challenges* 2019 [39], provide the interested reader with an up-to-date overview of the research front for CFD modeling of nasal airflow and other biomedical fluids. One important finding is that although a large part of nasal airflow research assumes incompressible flow due to the low Mach numbers, recent simulations for low temperatures, where the temperature differences become more significant, show that the density variations should be considered, thus requiring a compressible model.

1.2 Scope

A simple model for respiratory flow is derived, implemented and tested. In contrast to a substantial part of the discussed literature, the flow is assumed compressible. In addition, the flow is assumed inviscid.

Due to the large influence of the airway geometry on respiratory flow, it is reasonable to apply governing equations containing a geometric term. Thus, for the simple model presented, the compressible quasi-1D Euler equations are chosen as appropriate governing equations.

For first investigations, a converging-diverging nozzle is chosen as a simple and well-known geometry to model the physical system of the airways from the inlet at the nasal cavity to the closed boundary at the lungs.

Initial and both steady and unsteady boundary conditions closing the modeling equations are presented. The steady boundary conditions are simplified by approximating the characteristic equations of the eigenvalues. The unsteady boundary conditions describing the breathing cycle are determined by a sinusoidal time-varying stagnation pressure condition at the nozzle exit representing the lung.

Steady one directional flow modeling inspiration or expiration with steady boundary conditions is analyzed and simulated for flow in a converging-diverging nozzle, and the solutions are compared with the exact analytical solution for the Laval nozzle.

Oscillating flow with unsteady boundaries modeling the respiratory cycle is simulated applied to a constant cross-sectional area. Results are compared with empirically expected flow phenomena and reviewed literature.

1.3 Outline

In chapter 2, the governing equations are presented. The derivation of the quasi-1D Euler equations, the governing equations for the proposed model, is outlined in section 2.2. Finite volume method is detailed in chapter 3, and all relevant discretization methods are addressed. In chapter 4, the proposed numerical model for respiratory flow simulation is outlined. The discretization using the finite volume method is detailed, and the numerical initial and boundary conditions are discussed. The numerical results from four different test cases are presented and discussed in chapter 5. The model's ability to simulate respiratory flow under varying simplifying assumptions is also discussed. A summary of the thesis and concluding remarks are given in chapter 6. Finally, suggestions for future work are outlined in chapter 7.

2 | Governing equations

Modeling and simulation of fluid flow are dependent on a set of equations that describe the flow problem and its boundary conditions. In this chapter, the one-dimensional compressible Euler equations and the compressible quasi-one-dimensional Euler equations of gas dynamics are presented. The systems of equations are outlined, and the necessary assumptions and boundary conditions are discussed. The exact analytical solution for nozzle flows is outlined.

2.1 Compressible Euler equations

This section, 2.1, is an adaption of work presented in the author's project work Hansen 2018[16].

The Euler Equations are a reduced set of flow equations only valid in the inviscid parts of a flow field. The equations are obtained by neglecting the viscous terms and the heat-transfer terms in the Navier-Stokes equations. In other words, the flow is assumed to be inviscid and containing no external heat sources [41].

 The conservation of mass is not affected by the given assumptions, and therefore the continuity equation for the Euler equations is identical to the general continuity equation. In 1D in differential form, the continuity is expressed as

$$\frac{\partial \rho}{\partial t} + \frac{\partial (\rho u)}{\partial x} = 0 \,, \tag{2.1}$$

where ρ is the fluid density and u the velocity.

 The general momentum equation for fluid flow is obtained from Newton's second law of motion applied to a fluid passing through an infinitesimal control volume. In one-dimensional differential form it reads as

$$\frac{\partial (\rho u)}{\partial t} + \frac{\partial (\rho u^2)}{\partial x} = \rho g + \frac{\partial \sigma}{\partial x} \,, \tag{2.2}$$

where σ represents the stress, $\sigma = -p + \tau$, expressed by the pressure p and viscous stress τ, and g is the gravitational acceleration acting in the positive x-direction. Taking the assumption of inviscid flow into consideration, that is $\tau = 0$, the momentum equation for the compressible Euler equations yields

$$\frac{\partial (\rho u)}{\partial t} + \frac{\partial (\rho u^2 + p)}{\partial x} = \rho g \,. \tag{2.3}$$

 The energy equation for fluid flow is derived from the first law of thermodynamics. Similar to the continuity and momentum equations, the conservation law is applied to a

fluid passing through an infinitesimal, fixed control volume. Here, E denotes the total energy per unit mass. In 1D this yields

$$\frac{\partial \rho E}{\partial t} + \frac{\partial \left(\rho E u\right)}{\partial x} = \frac{\partial Q}{\partial t} - \frac{\partial q}{\partial x} + \rho g u + \frac{\partial \sigma u}{\partial x} \,, \tag{2.4}$$

where Q and q are the heat produced by external agencies and the heat flux by conduction, respectively. By applying the assumption of no external heat sources, i.e. $Q = 0$, the first term of the right-hand side, describing the rate of heat produced per unit volume by external heat sources, is neglected. The second term, $\frac{\partial q}{\partial x}$, describing the rate of heat lost by conduction per unit volume through the control surface, is also neglected. The stress σ, as for the momentum equation, contains a viscous term which is neglected due to the inviscid flow assumption. This yields the energy equation in differential form as

$$\frac{\partial \rho E}{\partial t} + \frac{\partial \left(\left(\rho E + p\right) u\right)}{\partial x} = \rho g u \,. \tag{2.5}$$

2.1.1   Equations of state

In order to fully determine the flow problem and close the Euler equations, equations of state are needed. These equations describe the relationship between different thermodynamic variables, i.e. ρ, p, T and e, where T is the temperature and e the specific internal energy. Relations for the transport properties are not required for the Euler equations due to the applied assumptions.

The specific total energy, i.e. total energy per unit mass, is defined by

$$E = e + \frac{1}{2} u^2 \,. \tag{2.6}$$

In plain English, the specific total energy is equal to the specific internal energy plus the specific kinetic energy.

From thermodynamics, the definition of total enthalpy H is

$$H = E + \frac{p}{\rho} \,. \tag{2.7}$$

Assuming perfect gas, the pressure p and the temperature T can be expressed as

$$p = (\gamma - 1)\rho e \,, \tag{2.8}$$

$$T = \frac{(\gamma - 1)e}{R} \,. \tag{2.9}$$

Here, R expresses the specific gas constant, typically $R = 287 \, \mathrm{m^2 \, s^{-2} \, K^{-1}}$ for air at standard conditions. The ratio of specific heats, γ, is constant for perfect gas and holds the value 1.4 for air at standard conditions.

2.1.2   Boundary conditions

To account for and correctly mathematically describe the boundaries of a flow problem, boundary conditions must be imposed. The boundaries can be both physical and/or artificial. A physical boundary is typically a solid impermeable wall, whereas an artificial

boundary is the far-field boundary of the control volume of a given flow problem. At an artificial boundary, there will typically be some in- and/or outflow across it. All boundaries impose restrictions on the flow and must be modeled by appropriate equations [37].

For a solid impermeable stationary wall, the boundary condition states that the flow cannot pass through the wall. This is written as $u_w = 0$, where u_w is the velocity at the wall.

For an artificial boundary, boundary conditions must only be provided for the incoming characteristic variables.

2.1.3 The compressible 1D Euler Equations

Applying the equations of state (2.6)-(2.9) to the reduced conservation equations (2.1),(2.3) and (2.5), one obtains the full 1D hyperbolic compressible Euler equations in differential conservation form:

$$\frac{\partial \mathbf{U}}{\partial t} + \frac{\partial \mathbf{F}(\mathbf{U})}{\partial x} = \mathbf{b}\,, \tag{2.10}$$

with

$$\mathbf{U} = \begin{bmatrix} \rho \\ \rho u \\ \rho E \end{bmatrix}\,, \quad \mathbf{F}(\mathbf{U}) = \begin{bmatrix} \rho u \\ \rho u^2 + p \\ \rho H u \end{bmatrix}\,, \quad \mathbf{b} = \begin{bmatrix} 0 \\ \rho g \\ \rho g u \end{bmatrix}\,, \tag{2.11}$$

where $\mathbf{U}$ is the state vector of conservative variables, $\mathbf{F}(\mathbf{U})$ is the flux vector and $\mathbf{b}$ is the vector of external sources. The pressure p can be expressed as a function of the conservative variables $\mathbf{U}$, $p = (\gamma - 1)\left(\rho E - \frac{1}{2}\frac{(\rho u)^2}{\rho}\right)$. Using this relation, (ρH) can also be expressed as a function of $\mathbf{U}$, i.e. $\rho H = \rho E + p$.

2.2 Nozzle equations

2.2.1 The Laval nozzle
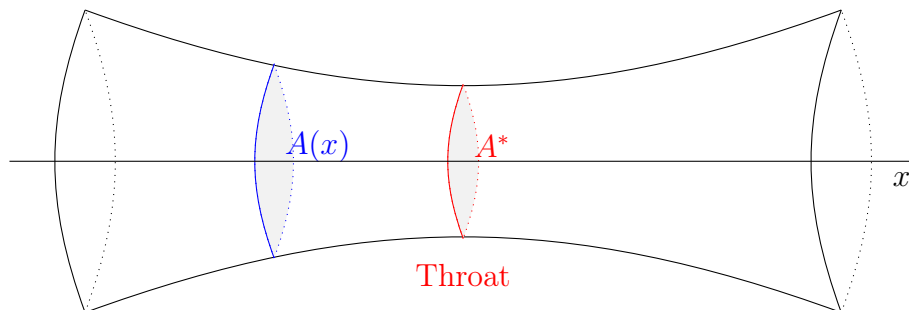
Figure 2.1: The Laval nozzle.

In 1893 the Swedish inventor Gustaf de Laval (1845-1913) developed the first converging-diverging nozzle, later termed Laval nozzle [4] in connection with a steam turbine. Contrary to Venturi nozzles, which are only applied to incompressible flow, the Laval nozzle

is used for compressible flow. The idea is to accelerate gaseous fluid through the nozzle to supersonic conditions.

A converging-diverging nozzle is simply a cylindrical pipe that first converges, that is the area of the pipe decreases, and then diverges, i.e. the area increases. A symmetric Laval nozzle has the same area at the inlet and outlet, as seen in figure 2.1.

At the throat of a nozzle, the section of minimum area denoted by superscript *, the largest achievable Mach number is unity [48]. Therefore, a simply converging nozzle cannot achieve supersonic flow conditions, because the maximum velocity at the exit corresponds to the sonic throat condition, $M^* = 1$. In order to accelerate the flow to supersonic conditions, a complete converging-diverging nozzle is required. Flow accelerated through a Laval nozzle does, however, not necessarily reach supersonic speed. The flow condition is dependant on the back pressure, p_b, and its relation to the stagnation pressure, p_0. The different cases of flow development dependant on $\frac{p_b}{p_0}$ are illustrated in figure 2.2, where the first vertical dashed line corresponds to the throat of the nozzle, and the second vertical dashed line correspond to the nozzle exit.
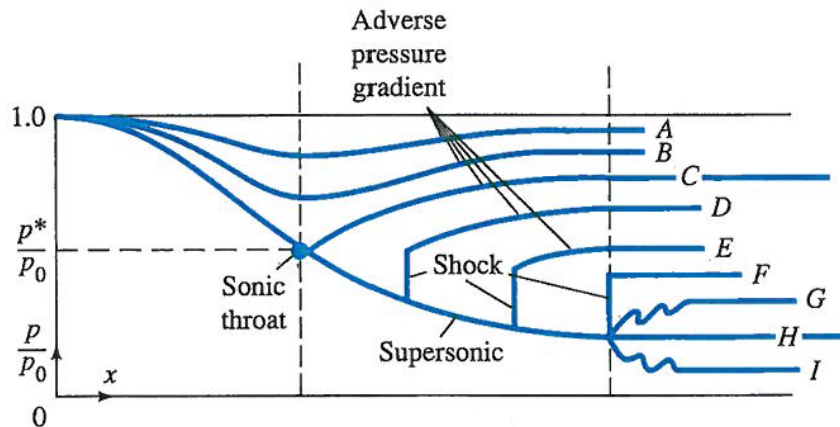
Figure 2.2: Pressure distribution $\frac{p_b}{p_0}$ along a Laval nozzle [5].

In case A and B, that is $p_b = p_A$ and $p_b = p_B$, the flow remains subsonic throughout the nozzle. In both cases, the velocity of the fluid increases in the converging section, reaches a maximum at the throat, and then decreases in the diverging section. However, the flow does not reach the sonic condition at the throat, i.e. $M^* < 1$. When $p_b = p_C$, that is case C, the flow reaches the sonic condition exactly at the throat. However, in order to reach the given ambient pressure, the flow must be decelerated in order to increase the pressure, and thus the diverging section acts as a diffuser. As the sonic condition has been reached at the throat, $M^* = 1$, and consequently the lowest obtainable pressure, p^*, has been achieved, lowering the back pressure further will not influence the flow in the converging section of the nozzle. In case D and E, that is $p_b = p_D$ and $p_b = p_E$, the sonic condition is reached at the throat, and the flow continues to accelerate in the diverging section, subsequently reaching supersonic conditions. However, in both cases, a normal shock develops in between the throat and the exit, bringing the flow back to subsonic conditions before the exit to match the given ambient pressure. If $\frac{p_b}{p_0}$ is further reduced, the normal shock travels downstream towards the exit, and in case F, $p_b = p_F$, the shock occurs precisely at the exit of the nozzle. In this case, the flow is supersonic throughout

the diverging section of the nozzle, only returning to subsonic conditions when crossing the normal shock at the exit. In the last three cases, G, H and I, there is no shock occurring in the nozzle and the flow exits the nozzle at supersonic conditions. However, for $p_b = p_G$, the pressure must increase after the flow exits the nozzle, causing an oblique shock to occur in the wake of the nozzle outlet. For case G, $p_b = p_G$, the given pressure relation is already achieved at the exit and the flow variables remain constant after leaving the nozzle. In the last case, $p_b = p_I$, expansion waves occur downstream of the exit, lowering the pressure of the fluid to match the ambient pressure.

The uniqueness of the sonic throat condition for converging-diverging nozzles, combined with the flow features being dependent on a given ambient back pressure, allows an exact analytical solution of the flow in a Laval nozzle to be derived.

2.2.2 Exact solution

For converging-diverging nozzles, exact flow solutions can be found through the isentropic flow relations. Because the sonic condition can only be achieved exactly at the throat of a Laval nozzle with steady, isentropic flow, flow relations specifically with respect to the sonic condition can be given. Combining the specific sonic condition, isentropic flow and an assumption of perfect gas, complete exact solutions for flow through a nozzle can be determined. In the following equations, the subscript $_0$ refers to stagnation conditions, and the superscript * refers to the sonic throat conditions.

Compressible fluid flow theory [52][45], states the isentropic relations for a perfect gas as

$$\frac{p}{p_0} = \left(\frac{\rho}{\rho_0}\right)^{\gamma} , \qquad \frac{p}{p_0} = \left(\frac{T}{T_0}\right)^{\frac{\gamma}{\gamma-1}} , \tag{2.12}$$

where p is the pressure, ρ is the density, T is the temperature and γ is the ratio of specific heats.

For steady inviscid flow the enthalpy is assumed constant, yielding $H_0 = H$ [4]. Using the assumption of perfect gas with $c_p = \frac{\gamma R}{\gamma-1}$, inserting equations (2.8) and (2.9) into the definition of enthalpy (2.7), yields $H = c_p T + \frac{u^2}{2}$. The Mach number is defined as $M = \frac{u}{c}$, where $c = \sqrt{\gamma \frac{p}{\rho}}$ is the speed of sound for perfect gas. Combining one obtains the temperature relation

$$\frac{T_0}{T} = 1 + \frac{\gamma - 1}{2} M^2 , \tag{2.13}$$

where M is the Mach number.

Inserting the relation (2.13) into the isentropic relations given in (2.12), the following relations are found:

$$\frac{p}{p_0} = \left[1 + \frac{\gamma - 1}{2} M^2\right]^{-\frac{\gamma}{\gamma-1}} , \tag{2.14}$$

$$\frac{\rho}{\rho_0} = \left[1 + \frac{\gamma - 1}{2} M^2\right]^{-\frac{1}{\gamma-1}} . \tag{2.15}$$

By considering the sonic throat condition where $M^* = 1$, one obtains the following relations for the thermodynamic quantities at the sonic condition:

$$\frac{T^*}{T_0} = \frac{2}{\gamma + 1}, \qquad \frac{p^*}{p_0} = \left(\frac{2}{\gamma + 1}\right)^{\frac{\gamma}{\gamma - 1}}, \qquad \frac{\rho^*}{\rho_0} = \left(\frac{2}{\gamma + 1}\right)^{\frac{1}{\gamma - 1}}. \qquad (2.16)$$

The ratio of the mass flux, ρu, and the critical mass flux $\rho^* u^*$ with $u^* = c^*$ for $M^* = \frac{u^*}{c^*} = 1$, may be written as

$$\frac{\rho u}{\rho^* u^*} = \frac{\rho_0}{\rho^*} \frac{c_0}{c^*} M \frac{\rho}{\rho_0} \frac{c}{c_0}, \qquad (2.17)$$

where c is the speed of sound and u is the flow velocity.

Making use of the isentropic relations in (2.12), the sonic relations in (2.16) and employing $\frac{c_0}{c} = \left(1 + \frac{\gamma - 1}{2} M^2\right)^{\frac{1}{2}}$ due to $c^2 = \gamma R T$ and equation (2.13), one obtains for the continuity $\rho u A = \rho^* u^* A^*$

$$\frac{A}{A^*} = \frac{1}{M} \left[1 + \frac{\gamma - 1}{\gamma + 1}\left(M^2 - 1\right)\right]^{\frac{\gamma + 1}{2(\gamma - 1)}}, \qquad (2.18)$$

where A is the cross-sectional nozzle area and A^* is the critical area [48]. This equation relates specific geometries to the Mach number and is critical for solving nozzle flow exactly.

When implementing the exact solution numerically, the critical area is first found using equation (2.18) with the given exit area A_e of the nozzle and the exit Mach number M_e computed from the given exit pressure and the initial stagnation condition making use of relation (2.14). Once the critical area is obtained, the Mach number for all values of x in the domain are found iteratively using the bisection method for equation (2.18). Now, the temperature, pressure, and density along the x-axis may be found using the isentropic relations (2.13)-(2.15), and the velocity is determined by the definition of the Mach number $u = cM$. Thus, all flow properties may be obtained and the exact analytical solution is complete.

2.2.3   The compressible quasi-1D Euler equations

The compressible quasi-1D Euler equations are obtained by applying conservation laws for compressible flow to a control volume Ω of a domain with varying flow area, such as a nozzle. The control volume Ω consists of three surfaces: the two cross-sectional surfaces Γ_1 and Γ_2 placed at x_1 and x_2, respectively, and the wall surface Γ_c spanning the outer casing of the nozzle between x_1 and x_2, as seen in figure 2.3.

As for the compressible 1D Euler equations, the flow is assumed to be inviscid and containing no external heat transfer.

The general conservation of mass for a control volume in integral form is given by

$$\int_\Omega \frac{\partial \rho}{\partial t} dV + \int_{\partial \Omega} \rho \vec{u} \cdot \vec{n} dA = 0, \qquad (2.19)$$

where Ω denotes the control volume, $\partial \Omega$ denotes the control surface, $\vec{u}$ is the velocity vector, and $\vec{n}$ is the outer unit normal vector.
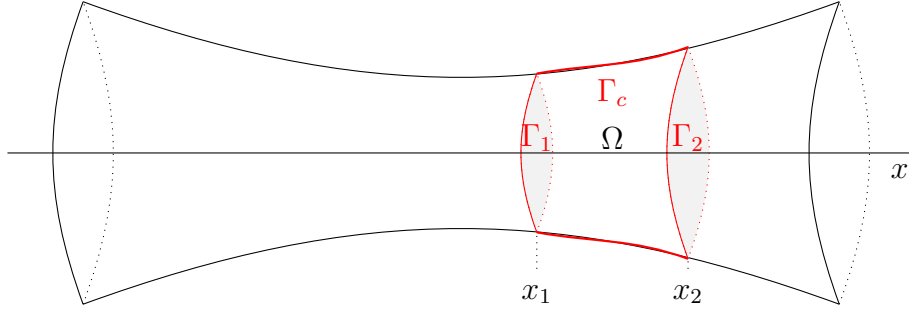
Figure 2.3: Control volume of a converging-diverging nozzle.

There is no penetration through the nozzle casing Γ_c, whereas there is mass transfer through the two control surfaces Γ_1 and Γ_2. Applying the conservation of mass to the converging-diverging nozzle in figure 2.3, one obtains

$$\int_\Omega \frac{\partial \rho}{\partial t} dV - \int_{\Gamma_1} \rho u \, dA + \int_{\Gamma_2} \rho u \, dA = 0 \,. \tag{2.20}$$

The differential volume is $dV = A(x)dx$. Furthermore, the flow variables are assumed constant for each cross-section. For this reason, equation (2.20) may be written as

$$\int_{x_1}^{x_2} \frac{\partial \rho}{\partial t} A(x) dx - (\rho u A)_1 + (\rho u A)_2 = 0 \,. \tag{2.21}$$

Following the fundamental theorem of calculus it is shown that

$$-(\rho u A)_1 + (\rho u A)_2 = \int_{x_1}^{x_2} \frac{\partial (\rho u A)}{\partial x} dx \,. \tag{2.22}$$

The cross-sectional area A(x) does not depend on time. Thus, inserting the relation (2.22) into equation (2.21) yields

$$\int_{x_1}^{x_2} \left(\frac{\partial (\rho A)}{\partial t} + \frac{\partial (\rho u A)}{\partial x} \right) dx = 0 \,. \tag{2.23}$$

Considering that the choice of the locations x_1 and x_2 of the control volume is arbitrary, the integrand in (2.23) must be zero. Consequently, the conservation of mass may be written in differential form as

$$\frac{\partial (\rho A)}{\partial t} + \frac{\partial (\rho u A)}{\partial x} = 0 \,. \tag{2.24}$$

The momentum equation is obtained from Newton's second law of motion, cf. section 2.1 , which states that the rate of change of momentum is equal to the net force acting on the control volume. In integral form for a general control volume for inviscid flow where gravity is neglected the law may be written as

$$\int_\Omega \frac{\partial (\rho \vec{u})}{\partial t} dV + \int_{\partial \Omega} \rho \vec{u} (\vec{u} \cdot \vec{n}) dA = -\int_{\partial \Omega} p \vec{n} \, dA \,. \tag{2.25}$$

Applying the conservation law (2.25) to the Laval nozzle yields the x-momentum in integral form

$$\int_{\Omega} \frac{\partial(\rho u)}{\partial t} dV - \int_{\Gamma_1} \rho u^2 dA + \int_{\Gamma_2} \rho u^2 dA = + \int_{\Gamma_1} p dA - \int_{\Gamma_2} p dA - \int_{\Gamma_c} p \vec{n}_c dA \,. \qquad (2.26)$$

Following the arguments of differential volume and constant flow variables for a given cross-section which were used to derive equation (2.23), the x-momentum equation (2.26) may be written as

$$\int_{x_1}^{x_2} \frac{\partial(\rho u)}{\partial t} A(x) dx - ((\rho u^2 + p)A)_1 + ((\rho u^2 + p)A)_2 = - \int_{\Gamma_c} p n_x dA \,, \qquad (2.27)$$

where n_x is the x-component of the normal unit vector $\vec{n}_c$.

In order to complete equation (2.27), the integral term on the right-hand side describing the pressure force acting on the outer casing of the nozzle Γ_c must be resolved. The pressure force on the casing acts inwards toward the center of the nozzle, that is in the negative normal direction, i.e. $-\vec{n}_c$. To find the pressure force components in the $x - y$ domain at $z = 0$, the pressure force $\vec{P} = -p\vec{n}dA$ is decomposed into an x-component and a y-component as shown in figure 2.4.
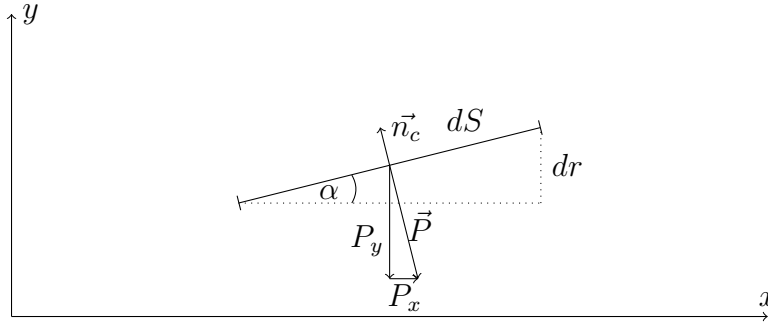
Figure 2.4: Pressure force $\vec{P} = -p\vec{n}dA$ acting normal to the nozzle casing Γ_c.

Because the nozzle is axis-symmetric around the x-axis, the pressure force component in the y-direction cancels itself. Consequently, only the pressure force component in the x-direction P_x needs to be considered. In order to rewrite the integral over Γ_c in (2.27) in terms of x, the geometry of the pressure force vectors must be considered. The angle between the horizontal x-direction and the control surface dS is denoted by α. This angle is again found between $\vec{P}$ and the unit vector in the negative y-direction due to the orthogonality of $\vec{P}$ and a vector parallel to dS, and P_y and the unit vector in the x-direction. This yields the following geometric relation for the pressure

$$P_x = |\vec{P}| \sin(\alpha) \,. \qquad (2.28)$$

From the geometry given in figure 2.4 and general cylinder geometry, it is given that

$$A = \pi r^2 \,, \qquad dA = 2\pi r dS \,, \qquad \sin(\alpha) dS = dr \,,$$
$$2\pi r = \frac{d\pi r^2}{dr} \,, \qquad dr = \frac{dr}{dx} dx \,, \qquad (2.29)$$

where r is the radius of the nozzle.

Applying the relation given in (2.28) and the geometric relations given in (2.29) to the x-component of the integral over Γ_c, it can be rewritten as

$$-\int_{\Gamma_c} pn_x dA = \int_{\Gamma_c} P_x dA = \int_{\Gamma_c} p\sin(\alpha) dA = \int_{s_1}^{s_2} p\sin(\alpha)2\pi r dS =$$
$$\int_{r_1}^{r_2} p2\pi r dr = \int_{r_1}^{r_2} p\frac{d\pi r^2}{dr} dr = \int_{x_1}^{x_2} p\frac{d\pi r^2}{dr}\frac{dr}{dx} dx = \int_{x_1}^{x_2} p\frac{dA}{dx} dx .$$

(2.30)

Using that $A = A(x)$, the fundamental theorem of calculus as in equation (2.22) applied to the corresponding terms in (2.27), and the resolved x-component of the integral over Γ_c from (2.30), the quasi-1D momentum equation in integral form is obtained.

$$\int_{x_1}^{x_2} \left(\frac{\partial(\rho u A)}{\partial t} + (\rho u^2 + p)A(x) \right) dx = \int_{x_1}^{x_2} p\frac{dA}{dx} dx$$

(2.31)

Again using the argument that the choice of the locations x_1 and x_2 of the control volume integrands is arbitrary, such as for (2.24), the differential form of the the quasi-1D momentum equation becomes

$$\frac{\partial(\rho u A)}{\partial t} + \frac{\partial((\rho u^2 + p)A)}{\partial x} = p\frac{dA}{dx} .$$

(2.32)

With the assumption of inviscid fluid and no external heat sources, the general integral form of the energy equation applied to a control volume yields

$$\int_{\Omega} \frac{\partial(\rho E)}{\partial t} dV + \int_{\partial\Omega} \rho E(\vec{u} \cdot \vec{n}) dA = -\int_{\partial\Omega} p\vec{u} \cdot \vec{n} dA ,$$

(2.33)

where, as in section 2.1.1, E is the total specific energy.

Applied to the Laval nozzle in figure 2.3, and noting that $\vec{u} \cdot \vec{n} = 0$ on the casing, the energy equations reads as

$$\int_{\Omega} \frac{\partial(\rho E)}{\partial t} dV - \int_{\Gamma_1} \rho E u dA + \int_{\Gamma_2} \rho E u dA = +\int_{\Gamma_1} p u dA - \int_{\Gamma_2} p u dA .$$

(2.34)

As for the mass equation and the momentum equation, the differential volume is $dV = A(x)dx$ and the flow variables at each cross-section are assumed to be constant, thus leading to

$$\int_{x_1}^{x_2} \frac{\partial(\rho E)}{\partial t} A(x) dx - ((\rho E + p)uA)_1 + ((\rho E + p)uA)_2 = 0 .$$

(2.35)

Again using the fundamental theorem of calculus and the fact that the area is independent of time $A = A(x)$, the quasi-1D energy equation in integral form is given as

$$\int_{x_1}^{x_2} \left(\frac{\partial(\rho E A)}{\partial t} + (\rho E + p)uA \right) dx = 0 .$$

(2.36)

Due to x_1 and x_2 being arbitrary, the quasi-1D energy equation may be written in differential form as

$$\frac{\partial(\rho E A)}{\partial t} + \frac{\partial((\rho E + p)uA)}{\partial x} = 0 .$$

(2.37)

Combined, the equations (2.24), (2.32) and (2.37) yield the complete compressible quasi-1D Euler equations:

$$\frac{\partial \mathbf{U}}{\partial t} + \frac{\partial \mathbf{F}(\mathbf{U})}{\partial x} = \mathbf{S}(\mathbf{U}) \,, \tag{2.38}$$

where

$$\mathbf{U} = \begin{bmatrix} \rho A \\ \rho u A \\ \rho E A \end{bmatrix} \,, \qquad \mathbf{F}(\mathbf{U}) = \begin{bmatrix} \rho u A \\ (\rho u^2 + p)A \\ (\rho E + p)u A \end{bmatrix} \,, \qquad \mathbf{S}(\mathbf{U}) = \begin{bmatrix} 0 \\ p\frac{dA}{dx} \\ 0 \end{bmatrix} \,. \tag{2.39}$$

2.2.4   Boundary conditions

To complete the governing flow equations, boundary conditions must be given. Both physical and artificial boundary conditions are required to close the flow problem described by the quasi-1D Euler equations.

The model has a physical no penetration boundary condition all along the axis-symmetric casing of the nozzle described as $u_w = 0$.

At the inlet and exit of the nozzle domain, artificial boundary conditions must be provided.

Inflow boundary

At the inflow boundary, for subsonic flow, only two physical boundary conditions must be given describing the two incoming waves on the characteristics. For the outgoing wave, the characteristic equation for the eigenvalue may be prescribed [37].

The constant enthalpy property obtained from the continuity equation and the energy equation is imposed by setting the total enthalpy equal the total stagnation enthalpy, $H = H_0$, where H_0 is the initial stagnation enthalpy. Accordingly, the entropy is also set constant equal the stagnation condition $s = s_0$. Thus yielding

$$H = H_0 \,, \qquad \frac{p}{p_0} = \left(\frac{\rho}{\rho_0} \right)^{\gamma} \,, \tag{2.40}$$

typical for internal flow [37].

The characteristic equation for the outgoing wave, $\partial p - \rho c \partial u = 0$, is approximated by

$$\frac{\partial p}{\partial x} = 0 \,, \tag{2.41}$$

which is a reasonable assumption for steady flow.

Outflow boundary

At the outflow boundary for subsonic flow, the two outgoing waves on the characteristics detailed as, $\partial p + \rho c \partial u = 0$ and $\partial p - c^2 \partial \rho = 0$, are approximated by

$$\frac{\partial \rho}{\partial x} = 0 \,, \qquad \frac{\partial \rho u}{\partial x} = 0 \,. \tag{2.42}$$

Again, this is a reasonable assumption for steady flows.

For the incoming wave, that is information coming from the exterior, a boundary condition must be provided. Here, the ambient pressure is prescribed yielding

$$p_{out} = p_{amb} \,. \tag{2.43}$$

3 | Finite volume method

Sections 3.1, 3.2.2, 3.3.2 and 3.3.3 are adaptions and modifications of work presented in the author's project work, see Hansen 2018 [16].

3.1   Basics of finite volume method
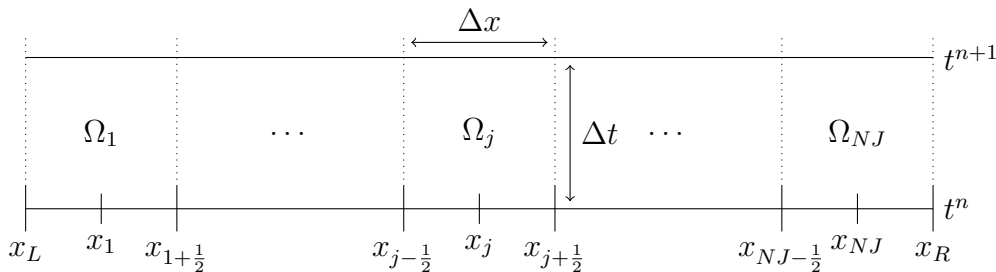
Figure 3.1: Discretization grid for the finite volume method.

A finite volume method, FVM, is a numerical discretization method for solving conservation laws. The principle of FVM is to apply conservation laws in integral form to a fixed region in space, i.e. a control volume, and then solve the integral equations [41]. The flow domain Ω, is divided into finite volumes Ω_j, that is control volumes, known as cells, see figure 3.1.

For a domain $[x_L, x_R]$ with NJ uniform cells, the spatial step size Δx, that is the length of each cell, is defined as $\Delta x = \frac{x_R - x_L}{NJ}$. The finite volumes are then defined by

$$\Omega_j = [x_{j-\frac{1}{2}}, x_{j+\frac{1}{2}}], \tag{3.1}$$

where the grid points $x_{j\pm\frac{1}{2}}$ define the faces of the finite volumes. Accordingly, each cell has two grid points taken at the left and right faces, written as

$$x_{j+\frac{1}{2}} = x_L + j\Delta x\,, \qquad x_{j-\frac{1}{2}} = x_L + (j-1)\Delta x\,, \qquad for \quad j = 1, 2, \ldots, NJ\,. \tag{3.2}$$

The midpoint of a cell Ω_j with length Δx is denoted by

$$x_j = \frac{1}{2}(x_{j-\frac{1}{2}} + x_{j+\frac{1}{2}}) = x_L + (j - \frac{1}{2})\Delta x\,, \qquad for \quad j = 1, 2, \ldots, NJ\,. \tag{3.3}$$

To discretize the computational domain in time, a temporal step size Δt is defined, and time instants are then computed by $t^n = n\Delta t$, where n denotes the specific time level.

When applying the conservation laws to each individual cell, FVMs approximate the integrals to consider the average values of conservative variables in each cell over the

19

complete spatial domain at time level n. The aim is then to update the cell averaged unknown at new time levels. Hence, the cell averaged value in cell j at time level t^{n+1}, that is U_j^{n+1}, is computed by approximating the respective conservation law in space and time [35].

In the following section, the finite volume method is derived for the quasi-1D Euler equations. For the vector of the conservative variables $\mathbf{U}$, the cell average $\mathbf{U}_j^n$ in cell Ω_j at time level n is defined as an approximation of the exact cell average at the same time level:

$$\mathbf{U}_j^n \approx \frac{1}{\Delta x} \int_{x_{j-\frac{1}{2}}}^{x_{j+\frac{1}{2}}} \mathbf{U}(x, t^n) dx \,, \tag{3.4}$$

where $\mathbf{U}(x, t)$ is the exact solution of the compressible quasi-1D Euler equations given in (2.38).

The source term $\mathbf{S}(\mathbf{U})$ is similarly approximated by

$$\mathbf{S}_j^n \approx \frac{1}{\Delta t \Delta x} \int_{t^n}^{t^{n+1}} \int_{x_{j-\frac{1}{2}}}^{x_{j+\frac{1}{2}}} \mathbf{S}(\mathbf{U}) dx dt \,. \tag{3.5}$$

The numerical fluxes are defined as approximations of the convective flux vector $\mathbf{F}(\mathbf{U})$

$$\mathbf{F}_{j\pm\frac{1}{2}}^n \approx \frac{1}{\Delta t} \int_{t^n}^{t^{n+1}} \mathbf{F}(\mathbf{U}(x_{j\pm\frac{1}{2}}, t)) dt \,. \tag{3.6}$$

The finite volume scheme is obtained by integrating the conservation law, in this case equation (2.38) over the domain $[x_{j-\frac{1}{2}}, x_{j+\frac{1}{2}}] \times [t^n, t^{n+1}]$, yielding:

$$\int_{t^n}^{t^{n+1}} \int_{x_{j-\frac{1}{2}}}^{x_{j+\frac{1}{2}}} \mathbf{U}_t dx dt + \int_{t^n}^{t^{n+1}} \int_{x_{j-\frac{1}{2}}}^{x_{j+\frac{1}{2}}} \mathbf{F}(\mathbf{U})_x dx dt = \int_{t^n}^{t^{n+1}} \int_{x_{j-\frac{1}{2}}}^{x_{j+\frac{1}{2}}} \mathbf{S}(\mathbf{U}) dx dt \,. \tag{3.7}$$

Integrating in space, thus utilizing the cell average approximations, yields

$$\int_{t^n}^{t^{n+1}} \Delta x (\mathbf{U}_j)_t dt + \int_{t^n}^{t^{n+1}} \left[\mathbf{F}(\mathbf{U}(x_{j+\frac{1}{2}}, t)) - \mathbf{F}(\mathbf{U}(x_{j-\frac{1}{2}}, t)) \right] dt = \int_{t^n}^{t^{n+1}} \Delta x \mathbf{S}_j dt \,, \tag{3.8}$$

where the integral of the derivative $\mathbf{F}(\mathbf{U})_x$ is solved using the fundamental theorem of calculus.

Solving the integration in time, thus inserting the numerical fluxes (3.6) into equation (3.8) and the temporal approximation for the source term yields the finite volume scheme:

$$\frac{\mathbf{U}_j^{n+1} - \mathbf{U}_j^n}{\Delta t} + \frac{\mathbf{F}_{j+\frac{1}{2}}^n - \mathbf{F}_{j-\frac{1}{2}}^n}{\Delta x} = \mathbf{S}_j^n \,. \tag{3.9}$$

3.2 Temporal discretization

3.2.1 Explicit Euler method

The explicit Euler method is the simplest numerical time-stepping scheme.

Applied to the quasi-1D Euler equations (2.38), the explicit Euler method reads

$$\mathbf{U}_j^{n+1} = \mathbf{U}_j^n + \Delta t \mathbf{R}_j(\mathbf{U}^n), \tag{3.10}$$

where $\mathbf{R}_j(\mathbf{U})$ is the residual, defined as $\mathbf{R}(\mathbf{U}) = -\frac{1}{\Delta x}\left[\mathbf{F}_{j+\frac{1}{2}}^n - \mathbf{F}_{j-\frac{1}{2}}^n\right] + \mathbf{S}_j^n$, scilicet the spatial terms found in the definition of the finite volume method (3.9).

The method is of first order accuracy with a truncation error of $\mathcal{O}(\Delta)t$ [41].

3.2.2 SSP Runge-Kutta method

The strong stability-preserving (SSP) Runge-Kutta (RK) method, previously called total variation diminishing (TVD) RK method, is a third order numerical time-stepping scheme.

In general, Runge-Kutta methods are used to solve ODEs, yet they may also be applied to PDEs. In order to use a RK method to solve a PDE, the PDE must first be converted into a system of ODEs [41], i.e.,

$$\frac{d\mathbf{U}}{dt} = \mathbf{R}(\mathbf{U}), \tag{3.11}$$

where $\mathbf{U} = [\mathbf{U}_1, ..., \mathbf{U}_{NJ}]$ is the vector of the cell averaged approximations $\mathbf{U}_j$ in all cells, cf. section 3.1, and $\mathbf{R} = [\mathbf{R}_1, \ldots, \mathbf{R}_{NJ}]$ is the vector of the residuals defined following equation (3.10). The residual must separately be discretized in space.

The simplest first order Runge-Kutta method corresponds to the explicit Euler method presented in section 3.2.1.

The temporal accuracy of Runge-Kutta methods is decided by the number of stages the method utilizes to achieve a solution at the new time level $n + 1$ and by the choice of the coefficients of the method. A three-stage Runge-Kutta scheme will first calculate $U^{(1)}$, then $U^{(2)}$, and then lastly U^{n+1}. The SSP Runge-Kutta method is a three-stage method of third order accuracy.

When applying the SSP RK method, the PDE in questions is rewritten as a semi-discrete equation, $\mathbf{U}_t = \mathbf{R}(\mathbf{U})$, corresponding to the finite volume definition. For the vector of conserved variables $\mathbf{U}$, the 3rd order SSP RK scheme is given by:

$$\mathbf{U}^{(1)} = \mathbf{U}^n + \Delta t \mathbf{R}(\mathbf{U}^n) \tag{3.12}$$

$$\mathbf{U}^{(2)} = \frac{3}{4}\mathbf{U}^n + \frac{1}{4}\mathbf{U}^{(1)} + \frac{1}{4}\Delta t \mathbf{R}(\mathbf{U}^{(1)}) \tag{3.13}$$

$$\mathbf{U}^{n+1} = \frac{1}{3}\mathbf{U}^n + \frac{2}{3}\mathbf{U}^{(2)} + \frac{2}{3}\Delta t \mathbf{R}(\mathbf{U}^{(2)}), \tag{3.14}$$

where n is the time level and $\mathbf{R}(\mathbf{U})$ is the residual.

Besides being of higher order than the explicit Euler method, the SSP Runge-Kutta method also has a larger stability domain [37]. The domain contains part of the imaginary axis supporting imaginary units in the Fourier stability analysis, which may occur from e.g. central differences.

3.3   Spatial discretization

The spatial residual $\mathbf{R}(\mathbf{U})$ must be discretized in space. The general definition of the residual, as previously stated, reads

$$\mathbf{R}(\mathbf{U}) = -\frac{1}{\Delta x}\left[\mathbf{F}^n_{j+\frac{1}{2}} - \mathbf{F}^n_{j-\frac{1}{2}}\right] + \mathbf{S}^n_j\,, \tag{3.15}$$

following the finite volume method definition for the quasi-1D Euler equations. Additionally, the source term $\mathbf{S}^n_j$ must be discretized.

In order to obtain solutions using finite volume method, the numerical fluxes $\mathbf{F}_{j+\frac{1}{2}}$ and $\mathbf{F}_{j-\frac{1}{2}}$ must be defined. This is done by spatial discretization methods which detail the numerical flux functions. This means that the Riemann problems defined by the cell averages at every interface need to be solved [35]. This can be done exactly, as in the Gudunov scheme, or approximately. An approximate solution can be used in the definition of the numerical flux yielding an approximate Riemann solver. See Toro 2009 [49] for an introduction to Riemann problems and numerical solvers.

The source term must also be discretized. In the scope of this thesis, the source term is discretized directly at the cell center with the area derivative made up of the area at the cell faces and the spatial step size. However, the source term may be discretized using different numerical approaches, herein fractional-step methods and Strang splitting methods [31]. Well-balanced methods have been developed to deal specifically with quasi-1D hyperbolic systems with spatially dependent source terms. More information on source term discretization can be found in Gosse 2013 [14].

Three approximate Riemann solvers are detailed below.

3.3.1   Lax Friedrichs scheme

The Lax-Friedrichs scheme is a simple, first order approximate Riemann solver. The method consists of a centered flux discretization and a numerical diffusion term. For the numerical flux vector $\mathbf{F}^n_{j\pm\frac{1}{2}}$, this yields the Lax-Friedrichs scheme

$$\mathbf{F}^n_{(j+\frac{1}{2}),LF} = \frac{1}{2}\left[\mathbf{F}(\mathbf{U}^n_j) + \mathbf{F}(\mathbf{U}^n_{j+1}) - \frac{\Delta x}{\Delta t}(\mathbf{U}^n_{j+1} - \mathbf{U}^n_j)\right]\,, \tag{3.16}$$

for which $\frac{\Delta x^2}{2\Delta t}$ is the numerical viscosity coefficient.

The scheme is more diffusive than the Gudonov method, especially for small time steps Δt, and exhibits a stair-step pattern when solving the inviscid Burgers' equation [31].

3.3.2   Rusanov scheme

The Rusanov scheme, also known as local Lax-Friedrichs scheme, is also a first order numerical flux function. The scheme improves upon the Lax-Friedrichs scheme by choosing the numerical viscosity coefficient locally at each Riemann problem [31]. The coefficient is thus taken as the largest local wave speed, ensuring stability of the scheme through convergence toward the vanishing-viscosity solution. This yields the Rusanov flux function

$$\mathbf{F}^n_{(j+\frac{1}{2}),Rus} = \frac{1}{2}\left[\mathbf{F}(\mathbf{U}^n_j) + \mathbf{F}(\mathbf{U}^n_{j+1}) - |\boldsymbol{\lambda}_{j+\frac{1}{2}}|(\mathbf{U}^n_{j+1} - \mathbf{U}^n_j)\right]\,, \tag{3.17}$$

with

$$|\boldsymbol{\lambda}_{j+\frac{1}{2}}| = max\left[\boldsymbol{\rho}(\mathbf{F}'(\mathbf{U}_j^n)), \boldsymbol{\rho}(\mathbf{F}'(\mathbf{U}_{j+1}^n))\right], \qquad (3.18)$$

where $\boldsymbol{\rho}(\mathbf{F}'(\mathbf{U}))$ is the spectral radius of the Jacobian matrix $\mathbf{F}'(\mathbf{U}) = \frac{\partial \mathbf{F}((\mathbf{U})}{\partial \mathbf{U}}$. That is, $\boldsymbol{\rho}(\mathbf{F}'(\mathbf{U})) = max_l\{|\boldsymbol{\lambda}_l|\} = |u| + c$, where $c = \sqrt{\gamma\frac{p}{\rho}}$ is the speed of sound and $\lambda_1 = u - c$, $\lambda_2 = u$, $\lambda_3 = u + c$ are the eigenvalues of $\boldsymbol{\rho}(\mathbf{F}'(\mathbf{U}))$.

The Rusanov method is total variation diminishing for scalar hyperbolic equations when used with the explicit Euler method as the temporal discretization scheme.

The total variation diminishing property ensures that the total variation of the solution does not increase for scalar conservation laws $U_t + F(U)_x = 0$, where U is the conserved scalar. This means that no new extrema are generated, making shock resolution smoother, i.e. with fewer oscillations, than when applying non-TVD methods [8]. However, the TVD property only holds mathematically for hyperbolic, scalar equations. Nevertheless, TVD methods for scalar conservation laws, such as the Rusanov method with explicit Euler time-stepping, may heuristically be applied to solve hyperbolic systems of equations. TVD methods have proved to give good results for hyperbolic equation systems such as the Euler equations [31][49].

Furthermore, a numerical time-stepping scheme applied to a scalar conservation law is TVD if used with a spatial discretization scheme that is TVD when combined with the explicit Euler method [31]. Therefore, the SSP Runge-Kutta method applied to scalar conservation laws is TVD when used with the Rusanov method which is TVD when used with the explicit Euler method. The heuristic application of TVD methods for hyperbolic systems also applies to TVD temporal discretization schemes.

3.3.3 MUSCL scheme

The TVD property for first order TVD methods, such as the Rusanov scheme with explicit Euler method in time, yields the resolution of discontinuities without oscillations [37]. However, as mentioned in subsection 3.3.1, the methods experience numerical dissipation. Higher order TVD methods hence seek a second order, or higher, accuracy for smooth flow, while keeping the non-oscillatory resolution of discontinuities.

First order TVD discretization methods in space may be extended to higher order to achieve a higher order of accuracy in space. One well-known extension is Van Leer's monotone upwind-centred scheme for conservation laws, abbreviated MUSCL [17]. Applied to a scalar conservation law, the finite volume concept is used. However, instead of approximating U_j as the cell average, see equation (3.4), linear approximations of $U_j(x,t)$ in cell Ω_j are taken. For a general finite volume method, this yields the higher order residuals

$$R_j = -\frac{1}{\Delta x}[F_{j+\frac{1}{2}}(U_{j+\frac{1}{2}}^L, U_{j+\frac{1}{2}}^R) - F_{j-\frac{1}{2}}(U_{j-\frac{1}{2}}^L, U_{j-\frac{1}{2}}^R)], \qquad (3.19)$$

where $U_{j\pm\frac{1}{2}}^L$ and $U_{j\pm\frac{1}{2}}^R$ are the linear extrapolations of the conserved variables at the cell faces $x_{j\pm\frac{1}{2}}$. Explicitly written as

$$U_{j+\frac{1}{2}}^L = U_j + \frac{\Delta x}{2}\frac{\partial U(x_j, t)}{\partial x}, \qquad U_{j+\frac{1}{2}}^R = U_{j+1} - \frac{\Delta x}{2}\frac{\partial U(x_{j+1}, t)}{\partial x}. \qquad (3.20)$$

The slopes introduced in equation (3.20) must be resolved so that a complete solution using the MUSCL approach may be achieved. Additionally, a limit on the slope must be

introduced in order to maintain the TVD property of the numerical flux. This is done by
using a limiter function.

In the scope of this thesis, a minmod limiter has been chosen. Thus, the extrapolated
variables with slope limited MUSCL approach with a minmod limiter yield:

$$U^L_{j+\frac{1}{2}} = U_j + \frac{1}{2} minmod \left[U_j - U_{j-1}, U_{j+1} - U_j \right] \tag{3.21}$$

$$U^R_{j+\frac{1}{2}} = U_{j+1} - \frac{1}{2} minmod \left[U_{j+1} - U_j, U_{j+2} - U_{j+1} \right] , \tag{3.22}$$

where the minmod limiter is defined as

$$minmod(a, b) = \begin{cases} a & , if \quad |a| \le |b| \quad and \quad ab > 0 \\ b & , if \quad |a| > |b| \quad and \quad ab > 0 \\ 0 & , if \quad ab \le 0 \end{cases} \tag{3.23}$$

$$= sign(a) \cdot max \left\{ 0, min\{|a|, sign(a) \cdot b\} \right\} . \tag{3.24}$$

The limiter ensures that if the slopes are of the same sign, the least steep slope is chosen,
otherwise it is set to zero.

The MUSCL scheme is of second order accuracy for a smooth flow away from extrema,
and of first order at extrema. Here, the MUSCL extrapolation is applied to the conser-
vative scalar variable U. Although, similarly as for the Rusanov scheme with explicit
Euler time-stepping, the MUSCL scheme is also used to discretize hyperbolic systems of
equations although the TVD property does not hold for non-scalar equations.

4 | Numerical Model

4.1 Assumptions and simplifications

As seen in section 1.1.1, the respiratory system is governed by a complex and intricate geometry. Therefore, any numerical model intended to compute solutions modeling respiratory flow must take geometry into account, i.e. include a geometric variable. Ideally, a full 3D model with a complete and realistic geometry is best suited to simulate respiratory flow. However, a complex three-dimensional model is outside the scope of this thesis. It is reasonable to assume that any 1D model may later be extended into two or three dimensions. A one-dimensional model with an area component, i.e. quasi-1D, is therefore a suitable first model for respiratory flow.

The flow medium in respiratory flow is air. From gas dynamics it is known that air is a compressible gaseous fluid, hence taking compressibility into account is reasonable. Following the scope of this thesis discussed in section 1.2, it is reasonable to limit the model with the assumption of inviscid flow.

In accordance with the discussed simplifications and assumptions, the numerical model is to be to a compressible, inviscid quasi-one-dimensional model. Henceforth making the compressible quasi-1D Euler equations, detailed in section 2.2.3, applicable as the main governing equations.

Respiratory flow is, as discussed in section 1.1.1, driven by the pressure forces that are generated by the respiratory muscles when breathing. Specifically, the pressure-volume-velocity relationship described by the Boyle-Mariotte law. However, when modeling, there are no muscles to initiate the flow. Therefore, the flow must be initiated as well as driven by the pressure forces alone.

In section 2.2.1, the flow through a converging-diverging nozzle is discussed. The nozzle flow is determined by the pressure relationship between the stagnation pressure and the ambient outlet pressure at the exit of the nozzle. This relationship determines the flow features.

Respiratory flow and nozzle flow hence have similar flow features where pressure forces are the main driving forces. In both cases, the relationship between the inner and outer pressure, for nozzles the exit and stagnation pressure, and for respiratory systems the pulmonary and surrounding ambient pressure, determines the direction of the flow and other features. Although converging-diverging nozzles have supersonic flow potential, this is not required for this model as the respiratory flow is strictly subsonic. The exact solution available for the Laval nozzle, detailed in section 2.2.2, yields the possibility for verification of the numerical model when applied to the same geometry. With this in mind, a suitable simple and well-known structure that may serve as a rudimentary representation of the respiratory geometry is that of the converging-diverging nozzle.

4.2   Finite volume discretization

The governing equations for the numerical model are the compressible quasi-1D Euler equations with a geometrically determined source term as presented in section 2.2.3. In conservation form this yields, as seen in equation (2.38),

$$\mathbf{U}_t + \mathbf{F}(\mathbf{U})_x = \mathbf{S}(\mathbf{U}) \,, \tag{4.1}$$

with

$$\mathbf{U} = \begin{bmatrix} \rho A \\ \rho u A \\ \rho E A \end{bmatrix} \,, \qquad \mathbf{F}(\mathbf{U}) = \begin{bmatrix} \rho u A \\ (\rho u^2 + p)A \\ (\rho E + p)u A \end{bmatrix} \,, \qquad \mathbf{S}(\mathbf{U}) = \begin{bmatrix} 0 \\ p\frac{dA}{dx} \\ 0 \end{bmatrix} \,. \tag{4.2}$$

In order to perform simulations on the numerical model, the governing equation system must be numerically discretized in time and space. This is done using the finite volume method.

Applying the finite volume scheme to the conservation equation (4.1), yields

$$\int_{t^n}^{t^{n+1}} \int_{x-\frac{1}{2}}^{x+\frac{1}{2}} \mathbf{U}_t \, dx \, dt + \int_{t^n}^{t^{n+1}} \int_{x-\frac{1}{2}}^{x+\frac{1}{2}} \mathbf{F}(\mathbf{U})_x \, dx \, dt = \int_{t^n}^{t^{n+1}} \int_{x-\frac{1}{2}}^{x+\frac{1}{2}} \mathbf{S}(\mathbf{U}) \, dx \, dt \,, \tag{4.3}$$

thus, cf. equation (3.9),

$$\frac{\mathbf{U}_j^{n+1} + \mathbf{U}_j^n}{\Delta t} + \frac{\mathbf{F}_{j+\frac{1}{2}}^n - \mathbf{F}_{j-\frac{1}{2}}^n}{\Delta x} = \mathbf{S}_j^n \,, \tag{4.4}$$

where $\mathbf{F}_{j\pm\frac{1}{2}}^n$ are the numerical fluxes in vector form, $\mathbf{U}_j^n$ is the approximation of the vector of conservative variables $\mathbf{U}$ in cell j, and $\mathbf{S}_j^n$ is the approximation of the source term in cell j. See section 3.1 for a more comprehensive derivation.

The conservative variables are discretized directly as they are defined at the cell centers. The numerical fluxes are approximations of the flux function in equation (4.2) and are discretized at the cell faces by spatial discretization schemes. The primitive and conservative variables are defined at the cell centers, which is taken into account in the various flux functions. However, the area is defined at all points of the spatial domain along the x-axis, and may therefore be taken exactly at the cell faces.

The source term, which consists of two items, must also be discretized. The pressure term is dependent on both time and space, and must therefore be discretized in both time and space. Similar to the other primitive and conservative variables, the pressure is defined at the center of each cell. Hence, the pressure is taken at cell j at time level n, yielding $p \approx p_j^n$. The area term is constant in time, thus solely of spatial dependency. A simple exact discretization of the area at the cell centres j, using the area at the cell faces, yields $\frac{dA_j}{dx} \approx \frac{1}{\Delta x}\left(A_{j+\frac{1}{2}} - A_{j-\frac{1}{2}}\right)$. Combining, the discretization of the source term becomes

$$\mathbf{S}_j^n = \begin{bmatrix} 0 \\ p_j^n \frac{(A_{j+\frac{1}{2}} - A_{j-\frac{1}{2}})}{\Delta x} \\ 0 \end{bmatrix} \,. \tag{4.5}$$

The complete finite volume discretization of the governing equations hence yields

$$\mathbf{U}_j^{n+1} = \mathbf{U}_j^n - \frac{\Delta t}{\Delta x}\left(\mathbf{F}_{j+\frac{1}{2}}^n - \mathbf{F}_{j-\frac{1}{2}}^n\right) + \Delta t \mathbf{S}_j^n \,, \tag{4.6}$$

with

$$
\mathbf{U}_j^n = \begin{bmatrix} \rho A \\ \rho u A \\ \rho E A \end{bmatrix}_j^n , \qquad
\mathbf{F}_{j\pm\frac{1}{2}}^n = \begin{bmatrix} \rho u \\ (\rho u^2 + p) \\ (\rho E + p)u \end{bmatrix}_{j\pm\frac{1}{2}}^n A_{j\pm\frac{1}{2}} , \qquad
\mathbf{S}_j^n = \begin{bmatrix} 0 \\ p_j^n \frac{(A_{j+\frac{1}{2}} - A_{j-\frac{1}{2}})}{\Delta x} \\ 0 \end{bmatrix} . \tag{4.7}
$$

Here, $\mathbf{U}_j^n$ is discretized directly in the cell centers j. The numerical flux functions $\mathbf{F}_{j\pm\frac{1}{2}}^n$, which are functions of the flux given in (4.2), must be detailed by a spatial discretization scheme as discussed in 3.3. The area in the flux terms is taken directly at the cell faces and may thus be treated separately, subsequently differentiating between the flow properties and the geometry. Lastly, the source term $\mathbf{S}_j^n$ is discretized as presented in equation (4.5). In addition to choosing a spatial discretization method, an appropriate time-stepping scheme must also be implemented for simulation.

4.2.1 Grid generation

The numerical model presented is a finite volume method. Accordingly, the standard finite volume grid, described in figure 3.1, is used. This means that the domain is divided into finite cells where the domain boundaries are given at the first and last cell faces. For the finite volume domain $\Omega_j = [x_{j-\frac{1}{2}}, x_{j+\frac{1}{2}}]$ with $j = 1, 2, ..., NJ$, the left boundary is given at cell face $x_{\frac{1}{2}}$ and the right boundary at cell face at $x_{NJ+\frac{1}{2}}$.

The conservative variables, ρ, ρu, ρE, and the primitive variables, u and p, are given at the cell centers x_j. The geometric variable, i.e. the area, is defined along the x-axis for the entire domain and may hence be taken both exactly at the cell faces and at the cell centers according to discretizational needs.

The temporal and spatial discretization steps are computed using simple geometric relations and computational flow relations. For NJ number of cells, the spatial step size Δx is set by NJ and the boundaries of the flow domain $\Omega = [x_{min}, x_{max}]$, such that $\Delta x = \frac{x_{max} - x_{min}}{NJ}$. The temporal step size is determined by the definition of the Courant number $C = a\frac{\Delta t}{\Delta x}$, where the coefficient is set to the spectral radius $a = |u| + c$, where u is the flow velocity and c the speed of sound. The initial Courant number is set in accordance with the CFL condition for stability. The temporal step size is thus determined as $\Delta t = \frac{C\Delta x}{|u|+c}$. To ensure that the given numerical end time t_{end} is not overstepped, the number of time steps NT is limited by a ceiling function and the step size corrected accordingly, i.e. $NT = ceil\frac{t_{end}}{\Delta t}$ and $\Delta t = \frac{t_{end}}{NT}$.

4.3 Initial and boundary conditions

Flow assumptions and simplifications have already been presented and discussed in section 4.1. Also, the physical boundaries of the governing equations have been detailed in section 2.2.4. However, to complete the model the initial and boundary conditions must be numerically handled, requiring more flow feature assumptions. Firstly, the flow in the nozzle is assumed to be isentropic, that is of constant entropy. The respiratory flow may, however, not be assumed isentropic, meaning the assumption only holds for the application of the flow to the nozzle geometry. The model flow is also assumed to behave as a perfect gas. These two assumptions are reasonable simplifications of air at standard

conditions, and are also required for the exact solution of flows in a converging-diverging nozzle.

4.3.1   Initial condition

Initially, it is assumed that there is no directional flow, i.e. the flow is at rest. When the velocity is zero, the stagnation condition is achieved. Hence, the primitive variables are set to the stagnation condition as the initial conditions for the model.

$$\mathbf{V}_{IC} = \begin{bmatrix} \rho_0 \\ 0 \\ p_0 \end{bmatrix} \tag{4.8}$$

Making use of the perfect gas relation $\rho E = \frac{p}{\gamma - 1} + \frac{1}{2}\rho u^2$, the conservative variables at time equals zero become

$$\mathbf{U}_{IC} = \begin{bmatrix} \rho_0 \\ 0 \\ \frac{p_0}{\gamma - 1} \end{bmatrix} A . \tag{4.9}$$

As stated, initially the flow is at rest with zero flow velocity. Accordingly, the flow velocity must be initiated by the pressure forces due to pressure differences between the inlet and the outlet of the domain.

4.3.2   Steady boundaries

Steady boundary conditions are used to simulate non-oscillating flow through the nozzle, i.e. one-directional flow. This corresponds to simulating only inspiratory or expiratory flow. The boundary conditions detailed below are used to simulate respiratory flow in the positive x-direction, meaning inhalation of air.

Inflow boundary

The leftmost boundary is given by the exact flux function at the left face $x_{j-\frac{1}{2}}$ of the first finite volume cell Ω_1.

$$\mathbf{F}_L = \mathbf{F}_{\frac{1}{2}} = \begin{bmatrix} \rho u A \\ \left(\rho u^2 + p\right) A \\ \left(\rho E + p\right) u A \end{bmatrix}_{in} \tag{4.10}$$

The constant enthalpy of the flow is implemented at the inflow and is determined by the initial condition, yielding

$$H_{in} = H_0 . \tag{4.11}$$

To account for the values in the flux at the inlet, the boundary conditions are applied detailing the pressure, density, and velocity from which all the required variables can be determined. First, the pressure at the inflow boundary is extrapolated from the first cell corresponding to the approximation of the characteristic boundary condition described in section 2.2.4. The density at the leftmost face is found through the isentropic relation given in equation (2.12). From the enthalpy definition $H = c_p T + \frac{u^2}{2}$ and the constant

enthalpy property given by the initial condition (4.11), the inflow velocity is derived. Thusly, the inflow boundary conditions are given as

$$p_{in} = p_1, \qquad \rho_{in} = \rho_0 \left(\frac{p_{in}}{p_0} \right)^{\frac{1}{\gamma}}, \qquad u_{in} = \sqrt{2 c_p (T_0 - T_{in})}, \qquad (4.12)$$

where the inflow temperature T_{in} is given through the perfect gas law $T_{in} = \frac{p_{in}}{\rho_{in} R}$, p_0 denotes the stagnation pressure and T_0 the stagnation temperature both determined by the initial condition. The area is taken exactly at the boundary.

Outflow boundary

The outflow boundary is, similarly as at the inflow, numerically handled by the exact flux function at the right face $x_{j+\frac{1}{2}}$ of the last finite volume cell Ω_{NJ}.

$$\mathbf{F}_R = \mathbf{F}_{NJ+\frac{1}{2}} = \begin{bmatrix} \rho u A \\ (\rho u^2 + p) A \\ (\rho E + p) u A \end{bmatrix}_{out} \qquad (4.13)$$

At the nozzle exit, both the density and the momentum are extrapolated from the last cell Ω_{NJ} in accordance with the approximation of the characteristic boundary conditions given in section 2.2.4. As discussed in sections 2.2.1 and 4.1, the pressure at the nozzle exit drives the flow in accordance with simulation of respiratory flow. Correspondingly, the pressure at the outflow boundary is set equal to the ambient pressure outside the domain on the right-hand side. The outflow boundary conditions for steady boundaries are thus given as

$$\rho_{out} = \rho_{NJ}, \qquad (\rho u)_{out} = (\rho u)_{NJ}, \qquad p_{out} = p_{amb}. \qquad (4.14)$$

All required values may be derived from the provided conditions. Moreover, the area is taken exactly at the boundary.

4.3.3   Unsteady boundaries

To simulate the cycles of respiratory flow, i.e. both inspiration and expiration as a function of time, the driving pressure forces must oscillate with respect to time. This is numerically implemented with the use of ghost cells, which values are not updated by numerical methods. The first and the last finite volume cells Ω_1 and Ω_{NJ} are thus not updated by numerical time-stepping. The ghost cell values are, however, taken into account by the approximate Riemann solver when calculating the numerical fluxes at the inner cell faces. In this way, the boundary conditions of the flow given in the ghost cells affect the flow which is simulated in the inner cells.

For a constant geometry with NJ cells, the ghost cell method is described in figure 4.1. The outer cells marked in green at $j = 1$ and $j = NJ$, are ghost cells and thus not updated by the solver. The inner cells are updated using information from the ghost cells obtained by the fluxes at the two faces as indicated in the figure; $\mathbf{F}_{\frac{3}{2}}$ and $\mathbf{F}_{NJ-\frac{1}{2}}$.
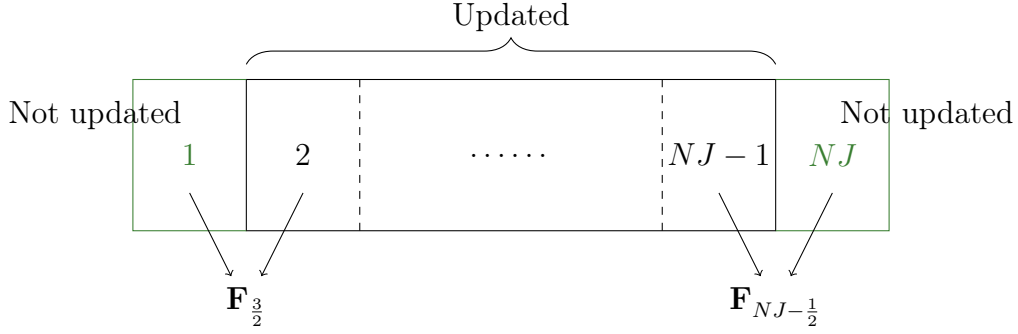
Figure 4.1: Implementation with ghost cells.

The left boundary

In the left ghost cell, the boundary corresponding to the surroundings is set. In contrast to the steady inflow boundary, the left most face does not need to be defined. Additionally, the Riemann solver takes care of the right face of the left most cell $\mathbf{F}_{\frac{3}{2}}$, as described above. Thus, the left ghost cell is set to keep the stagnation condition of the surroundings defined by the initial conditions. Subsequently, the first cell is set as follows

$$\mathbf{U}_1 = \begin{bmatrix} \rho_0 \\ 0 \\ \frac{p_0}{\gamma-1} \end{bmatrix} A_1 \,. \tag{4.15}$$

The right boundary

In the right ghost cell at $j = NJ$, approximate conditions of the lungs are set. As previously discussed, the flow is driven solely by pressure forces. For this reason, lowering the pressure p_{NJ} at $j = NJ$, i.e. in the lung, below the stagnation pressure p_0 of the surroundings will initiate a rarefaction wave traveling to the left simulating inspiratory flow. Simulation of expiratory flow is done by increasing the pressure p_{NJ} above the stagnation pressure p_0. For this purpose, the pressure in the last cell is set by a time-varying sine-function with a vertical shift corresponding to the stagnation pressure, thus yielding

$$p_{NJ} = p_0 - \sin(\omega t)\delta p \,, \tag{4.16}$$

where ω is the angular frequency, t is the time, and δp is the pressure amplitude.

   The pressure amplitude is chosen specifically for each test to correspond with the stagnation pressure of the problem to ensure that the flow operates in the specified range following the pressure relation $\frac{p_{NJ}}{p0}$. The use of a sine-function to describe the respiratory cycle is in accordance with in vivo measurements from Naftali et al. 1998 [38], as detailed in the literature review. The velocity in the cell NJ is assumed to be zero, letting the pressure be the only driving force of the flow. Thus, p_{NJ} can be considered the time-dependent stagnation pressure in the lung. The density is set by the isentropic relation from equation (2.12) determined by the oscillating pressure. This yields the following conditions in cell NJ

$$\mathbf{U}_{NJ} = \begin{bmatrix} \rho_0 \left(\frac{p_{NJ}}{p_0} \right)^{\frac{1}{\gamma}} \\ 0 \\ \frac{p_{NJ}}{\gamma-1} \end{bmatrix} A_{NJ} \,. \tag{4.17}$$

5 | Numerical Results

5.1 Test case: Sod shock tube with constant cross-sectional area

To verify that the correct governing equations have been implemented in the model, a test case with a constant cross-sectional area is considered. When a constant cross-sectional area is imposed for the quasi-1D model, the geometric source term is effectively removed due to the discretization of the source term. For this reason, the quasi-1D Euler equations should yield the same solution as the 1D Euler equations when applied to a constant area. The Sod shock tube problem is therefore solved using the 1D Euler equations discretized with the Rusanov scheme with extrapolation boundaries and explicit Euler time-stepping. The results are compared to the solution obtained when applying the quasi-1D Euler equations with the same numerical discretizations and extrapolation boundaries to the Sod shock tube problem. By comparing the two solutions of the same test, verification of the implementation may be achieved.

5.1.1 Setup

The description of the setup for the Sod shock tube problem is an adaption of work presented in Hansen 2018 [16].
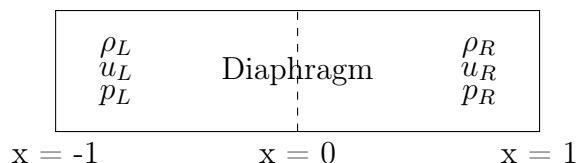
Figure 5.1: Physical description of the Sod shock tube.

The Sod shock tube problem is a widely used test case for numerical flow models to verify and compare different numerical schemes. It is particularly often used for validation of solution schemes for the Euler equations [15].

The shock tube consists of a straight cylindrical finite pipe with a diaphragm placed in the middle, here at $x = 0$. The diaphragm separates the fluid on the right and left side of the tube. The same gas is held on both sides of the diaphragm although at different states which are defined by the initial condition of the test case. When the diaphragm bursts, a shock wave propagates in the low pressure region, the right side, and then a contact discontinuity follows. In the high pressure region on the left, a rarefaction wave traveling to the left expands the flow reducing the pressure.

To simulate the gas at two different pressure states, initial conditions are set making sure that the pressure on the right side of the diaphragm is lower than that on the left. The

initial velocity is zero on both sides. The complete initial condition with dimensionless variables is detailed in table 5.1. In addition, the gas is assumed perfect, and the ratio of specific heats is set to $\gamma = 1.4$.

Table 5.1: Initial conditions for the Sod shock tube problem.

ρ_L	ρ_R	u_L	u_R	p_L	p_R
8	1	0	0	10	1

The computational grid is defined by NJ spatial steps, in this case the number of cells, and NT time steps. The spatial step size Δx is determined through the relationship described in section 4.2.1, in this case $\Delta x = \frac{2}{NJ}$. The number of time steps NT and the temporal step size Δt are, also as described in section 4.2.1, determined by the Courant number C, the spectral radius $SR = |u| + c$, and the end time t_{end}. The values of these three variables are determined heuristically with the goal of ensuring convergence and stability of the scheme. In this case, the Courant number is initially set to 1, the spectral radius to 2.5, keeping in mind that the initial flow velocity is zero, and the end time to 0.3.

The value of the spectral radius is determined by an upper bound on the calculated value after simulation. While upholding stability of the scheme, that is $C_j \leq 1$, the maximum value of the spectral radius, $SR_{max} = max_j \left[|u_j| + \left(\sqrt{\gamma \frac{p_j}{\rho_j}} \right) \right]$, was found to be 2.45. Initializing the spectral radius to a lower value with the same Courant number leads to an unstable scheme, hence the value of 2.5 is chosen in order to guarantee the stability of the scheme.

The short time frame of $t_{end} = 0.3$ ensures that all three expected discontinuities, previously described, are observed. When stepping longer in time, moving towards convergence of the conservative variables and a steady state solution, the flow discontinuities fully develop and cannot be observed at the last time step. Although full convergence and steady state is not reached, the scheme is stable and the CFL condition, $C = SR \frac{\Delta t}{\Delta x} \leq 1$, is satisfied with the largest local Courant number satisfying the condition.

The values given for Δt and NT in table 5.2 have been modified using the ceiling function to ensure that the end time t_{end} is not overstepped.

Table 5.2: Initial flow and grid variables for simulation of the Sod shock tube problem.

NJ	Δx	C	SR	t_{end}	Δt	NT
800	0.0025	1	2.5	0.3	0.001	300

The implementation of the quasi-1D Euler equations is very similar to that of the 1D Euler equations. For the numerical time stepping, there is no change in the implementation other than that the vector of conservative variables also includes the area. When implementing the numerical flux schemes, the area at the cell centers is first removed by division and then taken exactly at the faces of the finite volume cells. When analyzing the results at the last time step, the area at the cell midpoints is again canceled out, yielding results that may be directly compared to that of the 1D Euler equations. The shock tube is imitated by setting the area to an arbitrary nonzero constant at all values of x along the x-axis; here the area is set to 10.

5.1.2   Results

The solution at $t_{end} = 0.3$ with $NJ = 800$ computed with explicit Euler time stepping with the Rusanov scheme is presented in figure 5.2. The solution obtained with the quasi-1D Euler equations is denoted in the legend by "Quasi-1D", while the solution procured with the standard 1D Euler equations is denoted as "1D".

(a) Density

(b) Velocity

(c) Pressure

(d) Mach number
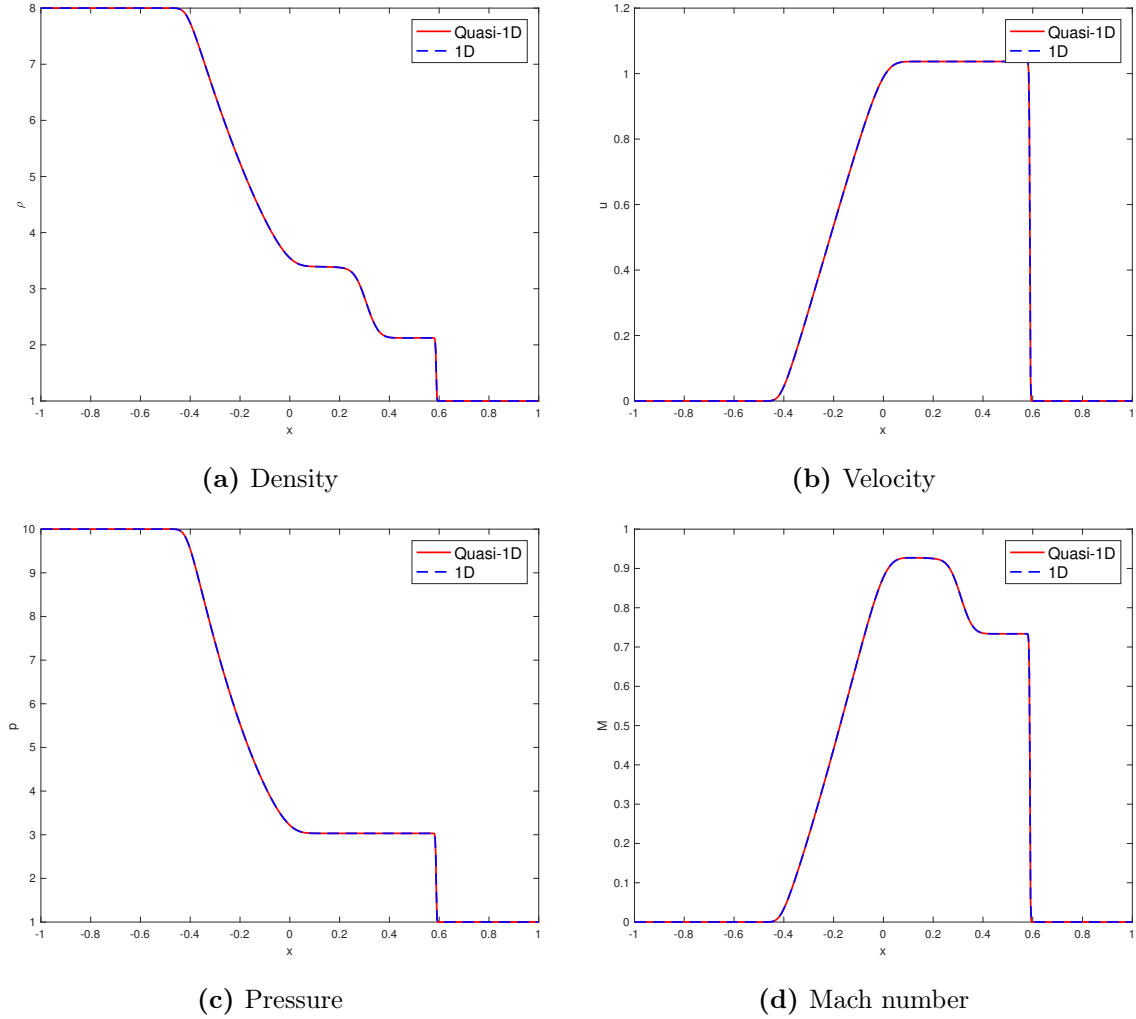
Figure 5.2: Results for the Sod shock tube discretized with the explicit Euler method with the Rusanov scheme for $NJ = 800$ at $t_{end} = 0.3$.

At first sight, the solution obtained using the quasi-1D Euler equations matches that of the 1D Euler equations with very high accuracy. For both simulations, the expected flow phenomena are visualized. On the left-hand side, approximately for $-0.4 \leq x \leq 0$, the expansion wave is clearly seen in all the subfigures. The density, as seen in figure 5.2a, and the pressure, as seen in figure 5.2c, both decrease in value following the wave. Simultaneously, the velocity increases, as seen in figure 5.2b, causing the Mach number to increase accordingly as observed in figure 5.2d.

For $0 \leq x \leq 0.6$, the velocity and the pressure, as seen in figures 5.2b and 5.2c, are of constant value. In the same spatial interval, the density and the Mach number exhibit changes and jumps. Because the velocity and the pressure are continuous while the density

is discontinuous with a jump in specific mass, the definition of a contact discontinuity is fulfilled [29][17], and therefore the expected contact discontinuity is observed.

At $x = 0.6$ a shock is present, visualized by the discontinuous variation that all the flow properties exhibit.

5.1.3   Convergence of models

As stated in 5.1.2, at first sight from the results in figure 5.2, the computations performed with the quasi-1D Euler equations seem to generate results with the same level of accuracy as those obtained with the standard 1D Euler equations. However, the convergence of the models and the error between them must be considered before a conclusion of verification may be drawn.

The error between the two models is estimated with the two-norm, defined as follows

$$||\mathbf{E}(\mathbf{U})|| = \sqrt{\Delta x \sum_{j=1}^{NJ} \mathbf{E}(\mathbf{U})^2}\,, \qquad \mathbf{E}(\mathbf{U}) = \mathbf{U}_{Quasi-1D} - \mathbf{U}_{1D}\,.$$

Looking at the error of the primitive variables $\mathbf{V}$, that is the density, the velocity, and the pressure of the flow, the errors should be very small in order to prove convergence of the two models. The errors of the primitive variables are given in table 5.3.

Table 5.3: Error of primitive variables for Sod shock tube comparing quasi-1D Euler equations to 1D Euler equations discretized with the explicit Euler method with the Rusanov scheme for $NJ = 800$.

$||\text{E}(\rho)||$	1.5904×10^{-15}
$||\text{E}(\text{u})||$	5.3067×10^{-16}
$||\text{E}(\text{p})||$	1.9027×10^{-15}

The errors of the primitive variables are of order 10^{-15} and smaller, proving the convergence of the two numerical models. Thereupon, it is verified that the implementation of the numerical model presented in section 4, in the event that the cross-sectional area is constant and simple extrapolation boundary conditions are imposed, solves a standard flow problem with the same accuracy as the 1D Euler equations.

5.2 Test case: Transonic converging-diverging nozzle flow

In order to verify the implementation and the performance of the numerical model with varying cross-sectional area with the discussed Laval nozzle geometry, a transonic converging-diverging nozzle flow problem is considered. The model may be verified by comparing the computed solution to the exact analytical solution which is iteratively obtained from the exact flow relations for the Laval nozzle as discussed in section 2.2.2.

The specific test case considered is presented in the case *Steady, Inviscid Flow in a Converging-Diverging Verification (CDV) Nozzle* edited by Slater 2008 [46], published in the NPARC Alliance Verification and Validation Archive [47]. The NPARC Alliance, short for National Program for Applications-Oriented Research in CFD, is a partnership between the NASA Glenn Research Center and the Arnold Engineering Development Center.

The test case provides a specific geometrical function for the area of a converging-diverging nozzle, an initial stagnation condition for the flow and an exit pressure. With these values, the boundary conditions may be determined as stated in section 4.3.

Comparison data is given at 51 cell faces corresponding to computations of the exact analytical solution. However, this data is not taken into account in this thesis due to the limited number of data points. Instead, the exact analytical solution has been implemented, as detailed in section 2.2.2, and computations performed for a 128 times finer grid than the given comparison data.

Figure 5.3: Converging-diverging verification nozzle geometry.
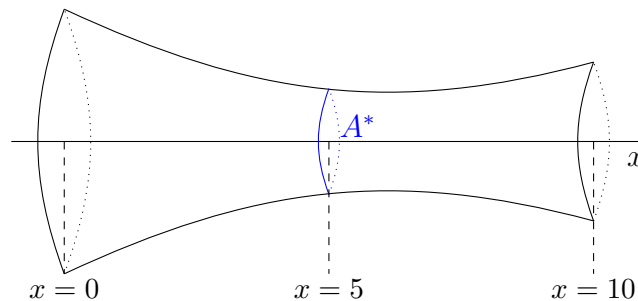
5.2.1 Setup

The initial stagnation condition and the ambient pressure at the nozzle exit specific to this test case are given in table 5.4.

Table 5.4: Initial stagnation condition and ambient pressure for transonic converging-diverging nozzle flow.

p_0	$10\,\text{kPa}$
T_0	$298\,\text{K}$
p_{amb}	$8.9\,\text{kPa}$

Following the discussion of the numerical handling of the initial and steady boundary conditions in section 4.3, the stagnation density must also be specified. This is done using the ideal gas law $\rho_0 = \frac{p_0}{RT_0}$. Likewise, the initial speed of sound reads $c_0 = \sqrt{\gamma R T_0}$. To complete the boundary conditions and initial condition, the isentropic flow variables must also be set, herein the ratio of specific heats γ, the specific gas constant R, and the specific heat at constant pressure c_p, all for standard air properties. The specific heat at constant pressure is calculated from the first two values following $c_p = \frac{\gamma R}{\gamma - 1}$. The flow variables are tabulated in table 5.5.

Table 5.5: General flow variables for air at standard conditions.

γ	1.4
R	$298 \, \text{J} \, \text{kg}^{-1} \, \text{K}^{-1}$
c_p	$1004.5 \, \text{J} \, \text{kg}^{-1} \, \text{K}^{-1}$

The geometry of the nozzle, visualized in figure 5.3, follows the mathematical description

$$A = 1.75 - 0.75 * cos((0.2x - 1.0) * \pi) \qquad x \leq 5 \qquad (5.1)$$
$$A = 1.25 - 0.25 * cos((0.2x - 1.0) * \pi) \qquad x > 5 \,, \qquad (5.2)$$

where $x \in [0, 10]$. Accordingly, the area at the inlet, throat and exit yields $A_{x=0} = 2.5$, $A_{x=5} = 1$ and $A_{x=10} = 1.5$ respectively.

When computing the solutions, the area is initially taken into the vector of the conserved variables following equation (4.2). Time-stepping is thus computed for the vector containing the area. In the flux computation, the area is first removed through division and later added back and taken directly at the cell faces as described in equation (4.7). The flux computation is, for this reason, computed solely for the conservative variables given as $\tilde{\mathbf{U}} = \frac{\mathbf{U}}{\mathbf{A}}$ where $\mathbf{A}$ is a matrix with the area in all rows.

For a chosen number of cells NJ, the spatial step size Δx, following section 4.2.1 yields $\Delta x = \frac{10}{NJ}$. To ensure stability, the initial Courant number and spectral radius are heuristically determined, thus determining the time step size. For computed Courant numbers $C \geq 0.6$ at $t_{end} = 2$, the model experiences stability issues when discretized with the explicit Euler method with the Rusanov scheme. This corresponds to a maximal spectral radius $SR = |u| + c$ of value 550, where c is the speed of sound. As a result, the initial Courant number is chosen as 0.6 and the initial spectral radius is chosen as 600. The spectral radius may also be found using the exact solution by determining the maximal spectral radius obtained with the exact solution. This yields $SR_{Exact,max} = max_j \left[|u_{j,Exact}| + \sqrt{\gamma \frac{p_{j,Exact}}{\rho_{j,Exact}}} \right] = 598$, in keeping with the set value of 600. The temporal step size Δt and the number of time steps may then be determined following the relations in section 4.2.1. By trial and error, the numerical end time is chosen as $t_{end} = 2$ where convergence of the conserved variables is found, and thereby steady state is achieved. The initial simulation values are tabulate in table 5.6.

Example code for this test case is found in appendix A.1.

Table 5.6: Initial flow and grid variables for simulation of transonic CDN flow.

NJ	Δx	C	SR	t_{end}	Δt	NT
3200	0.0031	0.6	600	2	3.1250×10^{-6}	640000

5.2.2 Results for first order discretization

The flow solution obtained from simulations with first order discretization using the explicit Euler method with the Rusanov scheme is presented and compared with the exact nozzle solution for the given initial condition and geometry. Figure 5.4 details the results of the pressure and Mach number distributions obtained with $NJ = 3200$ cells at $t_{end} = 2$, where the results from the respiratory model are denoted by the red line with legend "Computed" and the exact solution is denoted by the blue dashed line with legend "Exact". The first order discretization gives acceptable results with $NJ = 3200$ cells with what looks to be from figure 5.4 rather small errors when compared with the exact solution. However, the spatial resolution needed for accuracy of results with first order discretization schemes is much higher than expected.

| (a) Pressure | (b) Mach number |
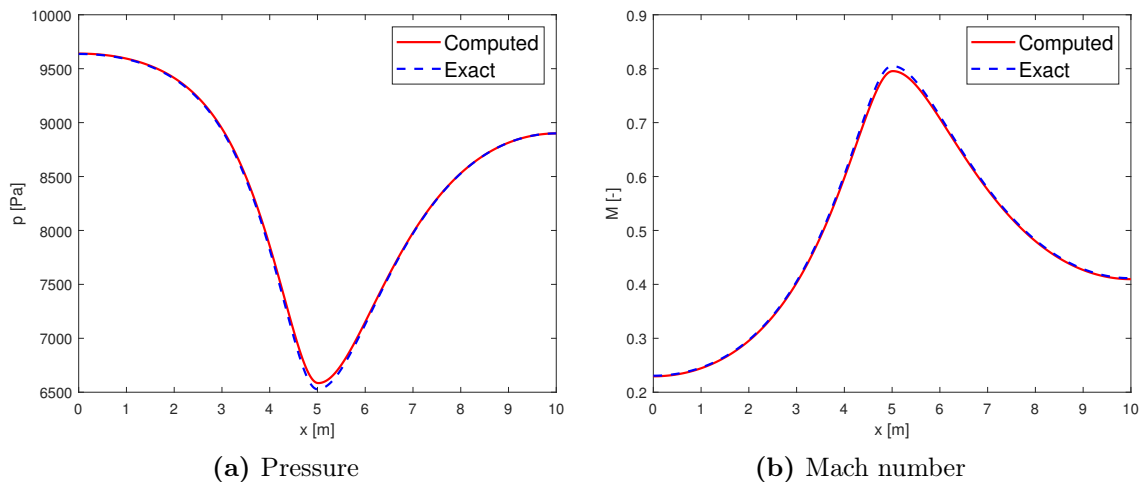
Figure 5.4: Results for the transonic CDN discretized with the explicit Euler method with the Rusanov scheme for $NJ = 3200$ at $t_{end} = 2$.

In figure 5.4a, it is observed that the outflow boundary condition is satisfied at t_{end}, therein the computed pressure in the last cell is $p_{NJ} = 8.9\,\text{kPa}$ corresponding to the ambient pressure given in table 5.4. Assuming an extrapolation to the exit cell face, it can be concluded that the boundary condition is satisfied.

As seen in figure 5.4b, the Mach number at the throat of the nozzle is approaching unity with $M^* = 0.8050$ calculated from the exact equations. Thus, the flow is transonic. The computed result yields $M^* = 0.7955$, also a transonic speed relatively near the value of the exact solution.

The solution presented is stable, with the largest Courant number at t_{end} satisfying the CLF condition $C \leq 0.6$ discussed in 5.2.1. Convergence of the conservative variables is also obtained with all the errors decreasing over five decades by $t = t_{end}$, thus confirming that steady state has been reached. The convergence history is shown in figure 5.5 where
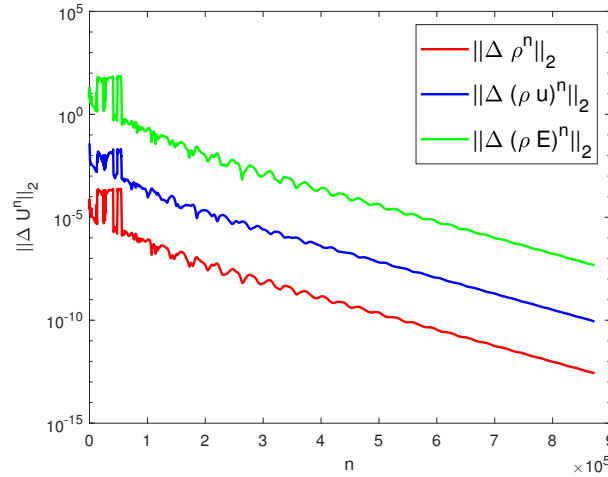
Figure 5.5: Convergence history of the conserved variables for first order discretization with $NJ = 3200$.

n is the time level and the error is defined as $||\Delta U^n||_2 = \sqrt{\Delta x \sum_0^{NJ}(\Delta U^n)^2}$ with $\Delta U^n = U^{n+1} - U^n$.

At the inlet, the enthalpy was set constant $H_{in} = H_0$. It is also expected that the enthalpy will be constant for the entire flow following the continuity and the energy equations. The computed results show this to be true as $\frac{||H-H_0||_2}{H_0} = 3.1888 \times 10^{-4}$ for $NJ = 3200$.

5.2.3   Grid convergence study for first order discretization

From the results presented, it is found that a grid of 3200 cells is needed in order to obtain a solution with relatively small errors. In contrast, Sesterhenn et al. 1993 [44] found results with acceptable errors with as few as 100 cells for 1D, although this was for low Mach number flow and thus may not be directly compared to this transonic case. Nevertheless, it is noteworthy that the number of cells needed for accuracy is thirty times higher than what might be expected.

To investigate the performance of the model with respect to the spatial resolution, a grid convergence study has been completed. In accordance with the presented results, the grid convergence also focuses on the two primitive variables: the density and the Mach number.

The errors of a primitive variable V for different grid refinement levels are computed with respect to the exact solution following

$$err = V - V_{Exact}.$$

In figure 5.6, the errors of the pressure and the Mach number along the nozzle x-axis for different grids are presented. It is shown that as the number of cells doubles, the errors rapidly decrease. It is also clear from the figure that the errors are largest at the throat of the nozzle, that is at $x = 5$. The large difference between the errors found for coarser grids, coupled with the fact that it takes a very fine grid of 3200 cells in order to obtain acceptable results, indicates that the model is grid dependent up until very fine grids. A more detailed discussion of the grid dependency follows in the discussion section.

The errors of all the primitive variables including the Mach number are tabulated in table 5.7. Furthermore, the grid convergence rate is presented. The convergence rate k is defined as

$$k = \frac{log\left(\frac{\|err\|_2^B}{\|err\|_2^A}\right)}{log\left(\frac{\Delta x^B}{\Delta x^A}\right)},$$

where A refers to a grid that is finer than B, and the error is defined as above. For first order discretization methods, such as the explicit Euler method with the Rusanov scheme used here, the expected grid convergence rate is unity.

(a) Error of pressure

(b) Error of Mach number
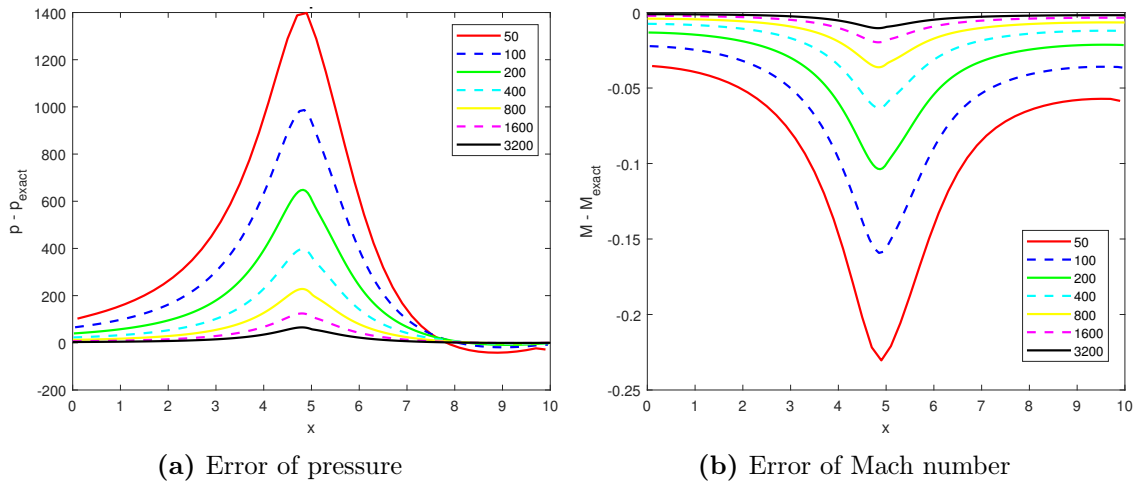
Figure 5.6: Error of primitive variables for the transonic CDN flow with first order discretization for different grid refinements.

As seen in table 5.7, the expected grid convergence rate of unity corresponding to the first order accuracy of the discretization methods used is obtained when going toward a grid with 3200 cells.

The errors found may be better understood when seen in comparison to the exact solution Thus, the maximal absolute relative error $RE(V)_{max} = \left(\left|\frac{\|E(V)\|_2}{V_{Exact}}\right|\right)_{max}$ has been computed and presented as percentages in table 5.8.

It is interesting to note, as seen in table 5.8, that the relative errors are consistently smaller for the Mach number than for the pressure, although the two properties are dependent on each other. Furthermore, the relative error of the pressure for $NJ = 50$ is very large with a value of over 20%.

The relative error of the enthalpy $RE(H) = \frac{\|H-H_0\|_2}{H_0}$ for different grid refinement levels and the corresponding convergence rates are given in table 5.9

The expected grid convergence rate of 1 is observed also for the enthalpy. Additionally, the small relative errors of the enthalpy prove that the boundary condition imposed at the inlet is satisfied.

Table 5.7: Error of primitive variables and grid convergence rate for transonic CDN flow with first order discretization.

NJ	$||E(\rho)||_2$	$k(\rho)$	$||E(u)||_2$	k(u)
3200	6.796×10^{-4}	0.9368	3.8613	0.9454
1600	1.301×10^{-3}	0.8895	7.4356	0.9045
800	2.410×10^{-3}	0.8210	13.919	0.8458
400	4.258×10^{-3}	0.7355	25.016	0.7727
200	7.089×10^{-3}	0.6416	42.739	0.6933
100	1.106×10^{-2}	0.5458	69.106	0.6139
50	1.614×10^{-2}	-	105.76	-

NJ	$||E(p)||_2$	k(p)	$||E(M)||_2$	k(M)
3200	74.4046	0.9396	0.01304	0.9430
1600	142.701	0.8944	0.02507	0.9004
800	265.269	0.8290	0.04679	0.8391
400	471.253	0.7475	0.08372	0.7631
200	791.180	0.6584	0.14207	0.6806
100	1248.71	0.5686	0.22772	0.5988
50	1851.94	-	0.34487	-

Table 5.8: Relative errors of primitive variables for transonic CDN flow with first order discretization.

NJ	$RE(p)_{max}[\%]$	$RE(M)_{max}[\%]$
3200	0.9883	0.4206
1600	1.8818	0.8187
800	3.4554	1.5576
400	6.0185	2.8647
200	9.8199	5.0471
100	14.995	8.4520
50	21.338	13.373

Table 5.9: Relative errors of enthalpy and grid convergence for transonic CDN flow with first order discretization.

NJ	$RE(H)[\%]$	k(H)
3200	0.03189	0.9753
1600	0.06269	0.9563
800	0.12164	0.9281
400	0.23146	0.8916
200	0.42940	0.8507
100	0.77435	0.8180
50	1.36520	-

5.2.4   Results for higher order discretization

Seeking to improve upon the results obtained with the first order methods, the same test case is simulated using SSP Runge-Kutta time-stepping with MUSCL extrapolation on the conservative variables. The simulation setup as described in section 5.2.1 is mostly kept as is. However, due to the higher order methods tolerating higher Courant numbers while still maintaining stability, the initial Courant number is heuristically set to $C = 0.8$ with $SR = 600$, thus yielding larger time step sizes and fewer time steps needed to reach convergence at $t_{end} = 2$. For clarity, the updated initial simulation variables are expressed in table 5.10.

Table 5.10: Initial flow and grid variables for simulation of transonic CDN flow with SSP RK method and MUSCL scheme.

NJ	Δx	C	SR	t_{end}	Δt	NT
800	0.01250	0.8	600	2	1.6667×10^{-5}	120000

In figure 5.7, the results from the simulation with higher order discretization methods are presented for $NJ = 800$ cells at $t_{end} = 2$. As expected, more accurate results are obtained for coarser grids than for simulations using first order discretization methods. To the naked eye, the computed results from the respiratory model lie exactly on the same line as the exact solution.

The exact Mach number at the nozzle throat is still $M^* = 0.8050$. The results obtained from simulation yield $M^* = 0.8048$, which is an error of 0.0244%. This proves a higher accuracy of the results in comparison to those obtained with the explicit Euler method with Rusanov fluxes.

Furthermore, the boundary conditions are satisfied. As seen in figure 5.7a, the pressure at the outflow, if extrapolated from the last cell yields $p_{NJ} = p_{amb}$. For the inflow, the enthalpy condition $H = H_0$ is checked. The computed results yield $\frac{||H-H_0||_2}{H_0} = 9.9921 \times 10^{-6}$, thus proving that the boundary condition is satisfied.

(a) Pressure   (b) Mach number
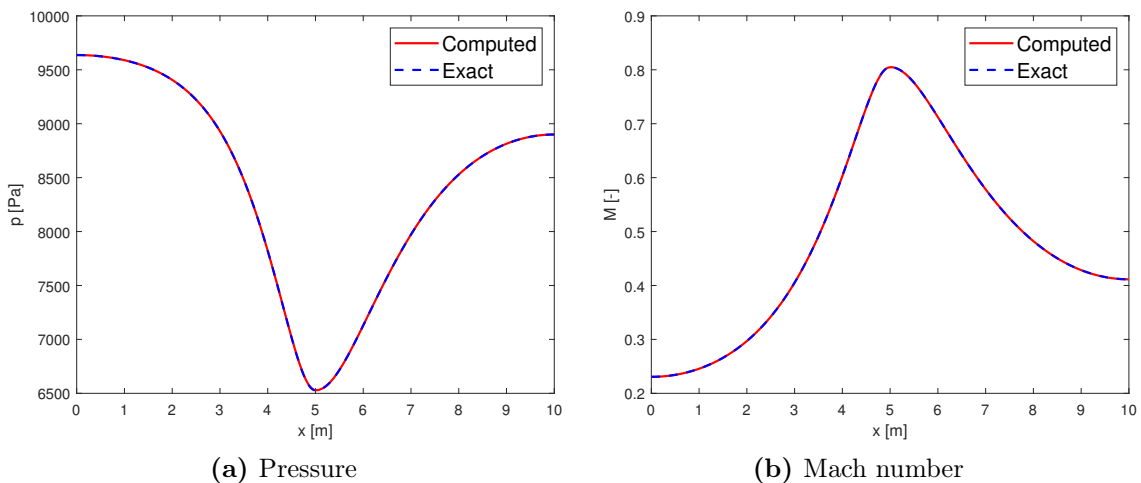
Figure 5.7: Results for the transonic CDN discretized with the SSP RK method and the MUSCL scheme for $NJ = 800$ at $t_{end} = 2$.

Steady state is also proved by the convergence history of the conservative variables, which decays five decades with respect to the numerical time step $n \in [0, NT]$ as seen in figure 5.8.
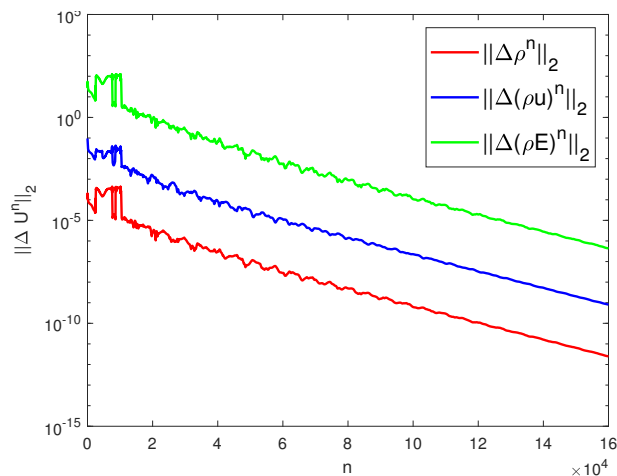
Figure 5.8: Convergence history of the conserved variables for higher order discretization with $NJ = 800$.

5.2.5 Grid convergence study for higher order discretization

To investigate the performance of the method further, a grid convergence study is executed. As seen from the results so far, the model performs better, as expected, when discretized with the higher order methods, here the SSP Runge-Kutta method with MUSCL extrapolation of the conservative variables.

(a) Error of pressure

(b) Error of Mach number
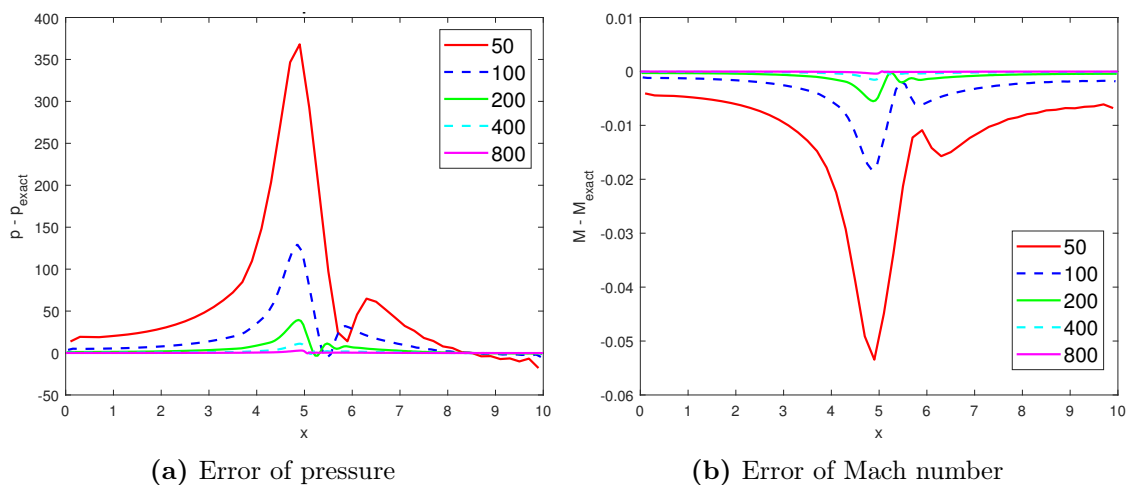
Figure 5.9: Error of primitive variables for the transonic CDN flow with higher order discretization for different grid refinements.

In figure 5.9, the errors of the primitive variables, the pressure and the Mach number, with respect to the exact solution are presented. As for the results from first order discretization, the errors are largest around the throat of the nozzle. However, for the

higher order discretization, a rather large jump is seen directly after the throat of the right-hand side, especially for coarser grids.

Following the definition of the grid convergence rate given in section 5.2.3, the errors of the primitive variables and the convergence rates for the higher order discretization are given in table 5.11. The expected grid convergence rate corresponds to the order of accuracy for the MUSCL scheme $\mathcal{O}(\Delta x^2)$. As seen in table 5.11, the expected convergence rate of 2 is found when approaching $NJ = 800$ cells.

Table 5.11: Error of primitive variables and grid convergence rate for transonic CDN flow with higher order discretization.

| NJ	$\|E(\rho)\|_2$	$k(\rho)$	$\|E(u)\|_2$	k(u)
800	1.713×10^{-5}	1.9830	0.08077	1.9923
400	6.772×10^{-5}	1.9548	0.32136	1.9753
200	2.625×10^{-4}	1.8840	1.26362	1.9223
100	9.690×10^{-4}	1.7140	4.78942	1.7739
50	3.179×10^{-3}	-	16.3781	-

NJ	$\|E(p)\|_2$	k(p)	$\|E(M)\|_2$	k(M)
800	1.8168	1.9851	2.791×10^{-4}	1.9910
400	7.1923	1.9601	1.109×10^{-3}	1.9719
200	27.985	1.8914	4.352×10^{-3}	1.9145
100	103.82	1.7257	1.641×10^{-2}	1.7604
50	343.37	-	5.558×10^{-2}	-

Again, it is interesting to look at the relative errors of the pressure and the Mach numbers, that is $RE(V)_{max} = \left(|\frac{\|E(V)\|_2}{V_{Exact}}|\right)_{max}$, where $E(V) = V - V_{Exact}$. The error percentages are given in table 5.12.

Table 5.12: Relative errors of primitive variables for transonic CDN flow with higher order discretization.

NJ	$RE(p)_{max}[\%]$	$RE(M)_{max}[\%]$
800	0.0452	0.0004
400	0.1692	0.0032
200	0.6003	0.0323
100	1.9660	0.2275
50	5.6163	1.4797

As seen for the first order discretization, the Mach number yields smaller relative errors than the pressure. Furthermore, the relative errors for the coarsest grid with $NJ = 50$ is not more than 6% compared to the exact solution. From the relative errors, it may be concluded that the model applied to a converging-diverging nozzle with transonic flow performs well when using higher order discretization methods.

In table 5.13, the relative errors of the enthalpy and the corresponding grid convergence rate is shown. The small relative errors prove that the inlet boundary condition is satisfied.

Table 5.13: Relative errors of enthalpy and convergence rate for transonic CDN flow with higher order discretization.

NJ	$RE(H)[\%]$	k(H)
800	$9.993{\times}10^{-4}$	1.9921
400	$3.975{\times}10^{-3}$	1.9733
200	$1.561{\times}10^{-2}$	1.9471
100	$6.019{\times}10^{-2}$	1.8858
50	$2.224{\times}10^{-1}$	-

The expected grid convergence rate of two is also observed. It is interesting to note that the relative enthalpy errors are much smaller than for the primitive variables. This is also observed for the first order discretization. Furthermore, the relative errors of enthalpy for higher order discretization are about 10^2 times smaller than for the first order discretization.

5.2.6   Discussion

The results obtained with first order discretization, in this case the explicit Euler method with the Rusanov scheme, show that the model with steady boundaries performs poorly for coarse grids, and that a grid with 3200 finite volume cells is needed to obtain results that have a relative error of under 1% compared to the exact flow solution. The large errors for coarse grids, and the number of required cells for accurate results indicate that the model, when applied to the transonic CDN test case, experiences a spatial resolution issue. This may be due to the discretization of the source term and its interaction with the flux discretization. For further work, the discretization of the source term should be revisited with well-balanced methods in mind.

Although the relative errors obtained are rather high, the expected grid convergence rate of 1 is achieved as seen in table 5.7. Additionally, the boundary conditions of the model are satisfied. This is proved by the pressure at the right outflow boundary corresponding to the imposed ambient pressure, and by the enthalpy of the entire flow being kept almost constant with a relative error of 1.4% for the coarsest grid with $NJ = 50$ as seen in table 5.9. On the other hand, the model exhibits stability issues as the method is only stable for Courant number up to 0.6, whereas the expected stability condition for explicit Euler method with Rusanov fluxes when applied to the 1D Euler equations is 1. The decreased stability range may stem from the source term in the quasi-1D Euler equations.

For higher order discretization, here using the SSP Runge-Kutta method with MUSCL extrapolated conservative variables, the model yields more accurate results for coarser grids. A grid of 800 cells gives very accurate results with relative errors under 0.05% when compared to the exact solution. Additionally, the required grid size for relative errors under 1% is 200 cells, that is 16 times fewer cells than for the results from first order discretization. The grid convergence rate tends towards the expected value of 2, stemming from the accuracy of the MUSCL scheme. However, as seen in figure 5.9, a jump in the errors of primitive variables is observed at the throat of the nozzle. This may be due to discontinuities in the first derivatives of the area function given in equation (5.1) as Δx tends towards zero. As for the first order methods, the model experiences

stability issues for higher order discretization methods at lower Courant numbers than when the same methods are applied to the 1D Euler equations. Again, the source term in the quasi-1D Euler equations is thought to be the instigator of the issue. Furthermore, the boundary conditions at the inlet and outlet are satisfied, evaluated by the pressure at the outflow boundary and the enthalpy error for the entire flow, respectively.

The model exhibits spatial resolution issues and stability issues for both first order and for higher order discretization methods. However, in both cases, the imposed boundary conditions are satisfied and the expected grid convergence rate is obtained. As expected, the spatial resolution issues improve when using higher order spatial discretization with the MUSCL scheme, although the strong spatial dependency of the solution is still present as illustrated in figure 5.10. For future work, it is therefore recommended to look into the
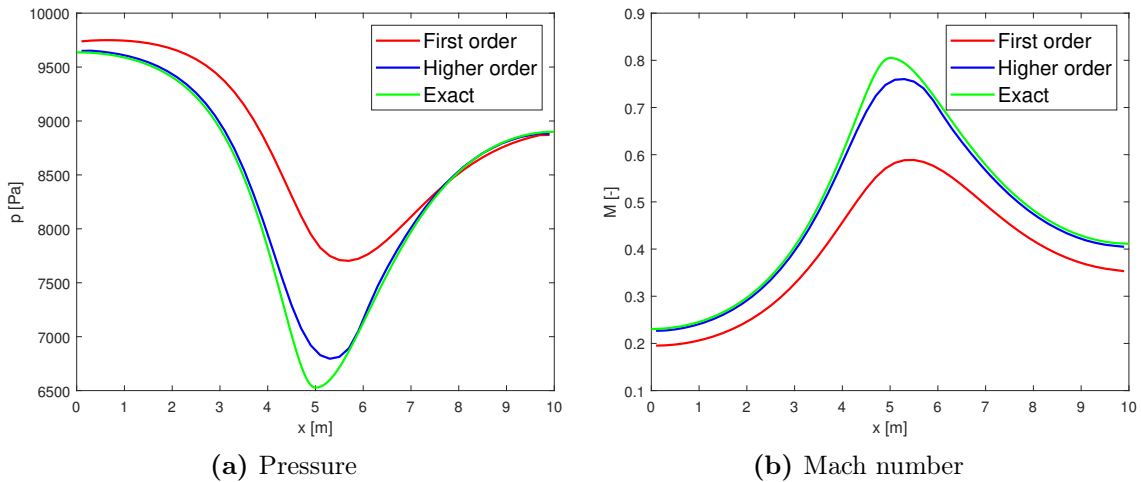

(a) Pressure   **(b)** Mach number

Figure 5.10: First order vs. higher order discretization with $NJ = 50$ at $t_{end} = 2$.

spacial dependency by investigating the effects of different flux solvers in particular, and as previously states, looking into well-balanced methods to improve the discretization of the source term.

Although more accurate results are obtained when using higher order discretization, the computational cost is also larger and must be considered, especially if the model is to be extended to 2D or 3D. CPU times for the first and higher order discretizations at differed grid refinements are seen in table 5.14. The times provided are only for the actual simulation, not including computation of convergence history data, which for comparison takes over 100 times longer. For the fine grid with $NJ = 3200$, simulation including the convergence history data takes approximately 12 hours. The simulations are performed using MATLAB 2018 on a stationary computer with a base speed of 3.4 GHz and 4 cores.

Table 5.14: CPU time [s] for simulation of transonic CDN flow for specific grid refinements.

NJ	200	400	800
First order	6.767	15.9991	42.3475
Higher order	20.5811	56.3726	159.9929

In general, the model performs well when applied to a transonic converging-diverging nozzle flow. Acceptable results are obtained, especially or higher order discretization, although these very fine grids are required. The model solves the transonic CDN flow with highly acceptable accuracy when discretized with higher order methods, although a spatial resolution issue is still observed. Stability issues pertaining to the range of the stability condition are present, although these are not of major significance. The spatial resolution issues may stem from the discretization of the source term as determined by the model, or one cannot rule out an implementation issue in regards to the spatial discretization. However, due to the accuracy of the results obtained when using the SSP RK method with MUSCL extrapolation of the conservative variable, it may be concluded that the model is verified for solving transonic flow in a converging-diverging nozzle.

5.3 Test case: Low Mach number converging-diverging nozzle flow

Because human respiratory flow is a subsonic flow with low Mach numbers [27][38], it is relevant to test the performance of the proposed model for a low Mach number flow. Still applied to a converging-diverging nozzle, the exact flow solution may be computed, thus the model may be verified for solving low Mach number flow. The steady boundary conditions detailed in 4.3 are applied.

5.3.1 Setup

With the goal of simulating low Mach number flow, the flow setup is determined by a chosen critical Mach number. Choosing $M^* = 0.0804$, the pressure ratio that drives the flow to obtain this throat condition is found using the exact flow solution, thus yielding $\frac{p_{amb}}{p0} = 0.998$. Keeping the dimensional form from the transonic case, the initial condition and the ambient pressure is set as presented in table 5.15.

Table 5.15: Initial stagnation condition and ambient pressure for low Mach number converging-diverging nozzle flow.

p_0	$10\,\text{kPa}$
T_0	$293\,\text{K}$
p_{amb}	$9.98\,\text{kPa}$

The spatial step size Δx is set, as before by $\Delta x = \frac{10}{NJ}$ for the given geometry seen in figure 5.3. As for the first two test cases, the CFL condition is found heuristically and set accordingly. Additionally, the spectral radius is set by finding the maximal spectral radius from the exact solution determined by $SR_{Exact,max} = max_j \left[|u_{j,Exact} + \sqrt{\gamma \frac{p_{j,Exact}}{\rho_{j,Exact}}} \right]$, which yields $SR = 370$. Setting the spectral radius above this value should ensure small enough time steps for stability. For this reason, the spectral radius is heuristically set to 500. The flow is found to be stable with convergence toward steady state for $C \leq 0.08$, and the initial Courant number is set to 0.1 accordingly. Due to the small Courant number, the time step Δt is also small compared to that of the transonic test case. Subsequently, the numerical end time must be larger to reach convergence and is thusly set as $t_{end} = 10$.

Table 5.16: Initial flow and grid variables for simulation of low Mach number CDN flow.

NJ	Δx	C	SR	t_{end}	Δt	NT
400	0.025	0.1	500	10	5.00×10^{-6}	2000000

The geometry of the nozzle is the same as for the transonic case, given by equation (5.1) describing the area as a function of x.

Due to the significant improvement of the performance of the model in the transonic CDN test case when discretized with higher order methods, a higher order discretization is also implemented for this test case. As previously, the SSP Runge-Kutta method with MUSCL extrapolation on the conservative variables is used.

5.3.2   Results

The results from simulation of the low Mach number CDN flow with $NJ = 400$ at $t_{end} = 10$ are presented in figure 5.11.

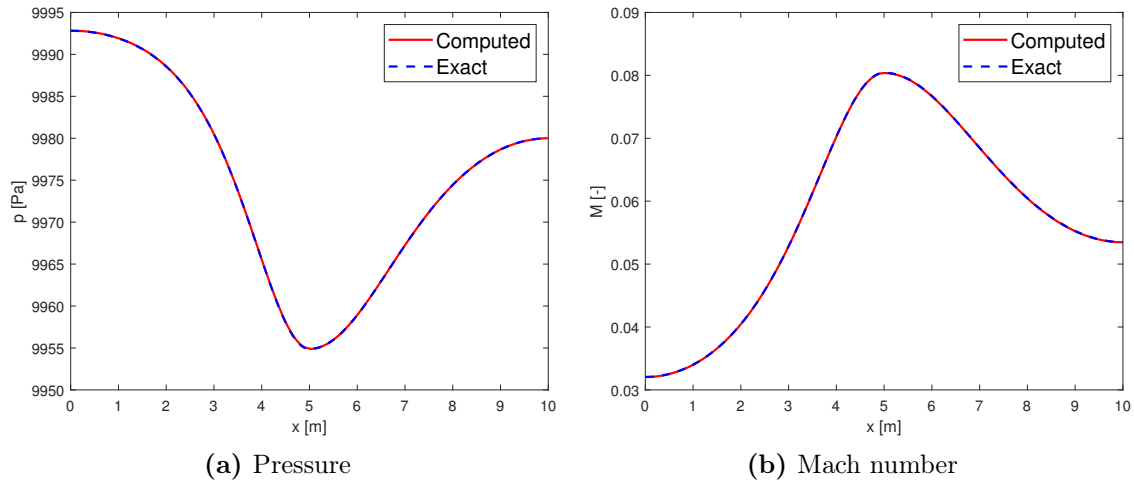<p align="center">(a) Pressure   (b) Mach number</p>

Figure 5.11: Results for low Mach number CDN discretized with the SSP RK method with the MUSCL scheme for $NJ = 400$ at $t_{end} = 10$.

By visual inspection of the results, the pressure and the Mach number distributions computed with the model lie exactly on top of those of the exact solution. Investigation of the numerical results shows the same. The set Mach number which is determined by the exact solution, is also obtained by the simulation with $M^*_{Exact} = M^* = 0.0804$.

The boundary conditions of the model are satisfied. At the outlet, extrapolated from the last cell, the pressure is found to be $p_{NJ} = p_{amb} = 99.8\,\text{kPa}$, thus satisfying the outflow boundary condition. For the inlet, the constant enthalpy condition $H = H_0$ is investigated. At $t_{end} = 10$ it is found that $\frac{||H - H_0||_2}{H_0} = 1.6537 \times 10^{-6}$ thus indicating that the condition is satisfied for the entire flow.

Convergence toward the steady state solution is also obtained, and is visualized by the convergence history of the conservative variables shown in figure 5.12 at $t_{end} = 10$, where n is the current time step. The errors of the conservative variables are defined as $||\Delta U^n||_2 = ||U^{n+1} - U^n||_2$. The history shows that steady state is obtained by the decay of ten decades for all variables.

5.3.3   Grid convergence study

To investigate the test case further, a grid convergence study is performed. The errors of the pressure and the Mach number compared to the exact solution are presented in figure 5.13 for different grid refinements. The error is defined as $V - V_{Exact}$.

In figure 5.13, it is observed that the largest errors appear around the throat of the nozzle. The error of the pressure, as seen in figure 5.13a, is largest just before the throat, and then exhibits a jump at the throat seen for all the grid refinement levels, although it is more severe for the coarsest grid of $NJ = 50$. The same jump is not observed for the error of the Mach number seen in figure 5.13b.
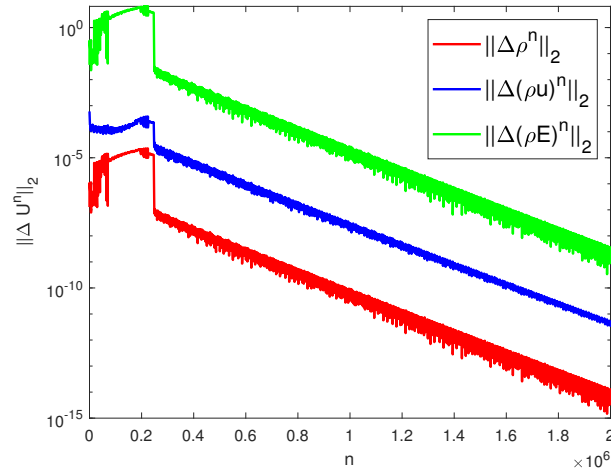
Figure 5.12: Convergence history of conservative variables for low Mach number CDN flow with $NJ = 400$ at $t_{end} = 10$.

(a) Error of pressure

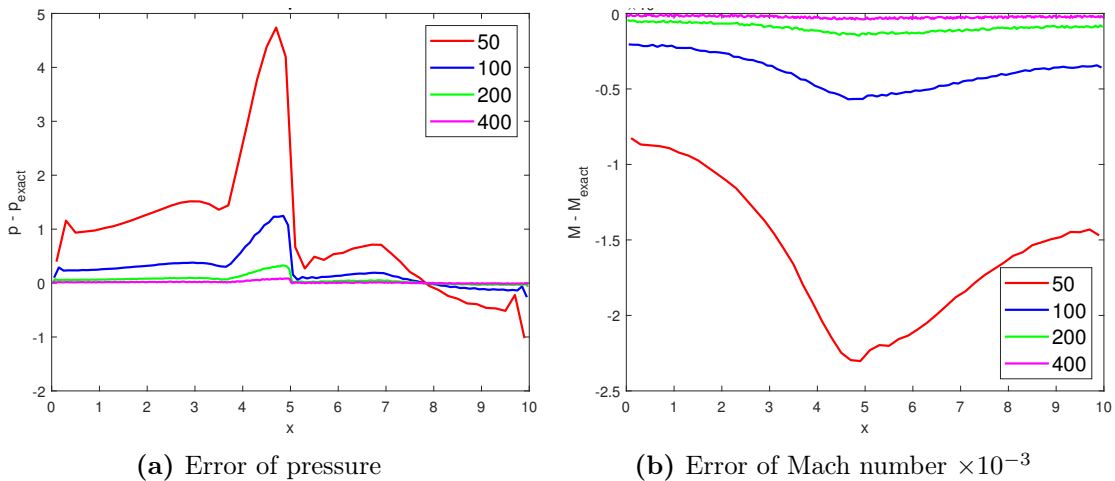**(b)** Error of Mach number $\times 10^{-3}$

Figure 5.13: Error of primitive variables for low Mach number CDN flow with higher order discretization for different grid refinements.

The grid convergence rate is calculated following the relation presented in section 5.2.3. The expected rate for a grid independent solution is two due to the MUSCL scheme being of second order of accuracy. As seen from the values in table 5.17, the expected grid convergence rate is found. The errors of primitive variables are also shown.

The convergence rate of two is already obtained when going from a grid of 50 cells to a grid of 100 cells, in keeping with the expected results cf. Sesterhenn et al. 1993 [44]. However, the convergence rate decreases slightly for the finer grids.

The relative errors obtained with the simulated results are presented in table 5.18. The errors are defined as $RE(V)_{max} = (|\frac{V - V_{Exact}}{V_{Exact}}|)_{max} * 100$, thus given as percentages [%].

The relative errors for the Mach number are larger than those for the pressure, which is in contrast to the results obtained for the transonic case. The largest relative error is of only 2.6%, indicating that the model with steady boundary conditions yields highly accurate results when applied to a low Mach number converging-diverging nozzle and

discretized with higher order methods.

In table 5.19, the relative errors of the enthalpy for different grid refinement levels, as well as the grid convergence rate are given. The very small relative errors of the enthalpy proves that the inflow boundary condition is satisfied.

Table 5.17: Error of primitive variables and grid convergence rate for low Mach number CDN flow with higher order discretization.

NJ	$\|E(\rho)\|_2$	$k(\rho)$	$\|E(u)\|_2$	k(u)
400	6.564×10^{-7}	1.9979	0.02647	2.0111
200	2.622×10^{-6}	2.0471	0.10670	2.0268
100	1.084×10^{-5}	2.0850	0.43479	2.0313
50	4.597×10^{-5}	-	1.77724	-

NJ	$\|E(p)\|_2$	k(p)	$\|E(M)\|_2$	k(M)
400	0.07916	1.9783	7.780×10^{-5}	2.0111
200	0.31191	2.0073	3.136×10^{-4}	2.0267
100	1.25391	1.9800	1.278×10^{-3}	2.0301
50	4.94662	-	5.223×10^{-3}	-

Table 5.18: Relative errors of primitive variables for low Mach number CDN flow with higher order discretization.

NJ	$RE(p)_{max}[\%]$	$RE(M)_{max}[\%]$
400	0.0009	0.0186
200	0.0033	0.1314
100	0.0125	0.6317
50	0.0476	2.5744

Table 5.19: Relative errors of enthalpy and convergence rate for low Mach number CDN flow with higher order discretization.

NJ	$RE(H)[\%]$	k(H)
400	1.654×10^{-4}	2.0289
200	6.749×10^{-4}	1.9778
100	2.658×10^{-3}	1.8652
50	9.685×10^{-3}	-

5.3.4 Discussion

The results for low Mach number flow in a converging-diverging nozzle discretized with the SSP Runge-Kutta method with the MUSCL scheme show a very high level of accuracy for a grid of 400 cells. Accurate results are also obtained already for 100 cells with relative errors under 1%. As seen in table 5.17, the expected grid convergence rate of 2 is obtained already going form 50 to 100 cells. When refining the grid further, the convergence rate decreases somewhat for the primitive variables. This may be due to rounding errors which are encountered once the grid becomes so fine that the previously dominant spatial truncation errors, for MUSCL $\mathcal{O}(\Delta x^2)$, become insignificant. In addition, the risk for rounding errors is larger for low Mach number flow than for flow with higher speeds.

Similar to the results obtained for the transonic case, a jump in the errors is observed at the throat of the nozzle. Again, this may be due to discontinuities of the first derivatives of the area function as Δx tends towards zero. However, in contrast to the transonic case, the jump is only seen in the error of the pressure and not for the Mach number.

The solution for low Mach numbers, comparatively to the transonic case, exhibits stability issues yielding a small range of Courant numbers ensuring stability of the model. Here, stability is found for $C \leq 0.08$; however, it is expected that the model could reach at least $C = 1$ and still be stable in accordance with findings from literature. Sesterhenn et al. in *Flux-vector splitting for compressible low Mach number flow* 1993 [44] test three different methods applied to a converging-diverging nozzle with a grid of 100 cells. All three methods use incoming characteristic boundary conditions imposing the entropy and total enthalpy in a reservoir, i.e. s_0 and H_0. The steady inflow boundary condition for the proposed model is an approximation of the characteristic incoming boundary conditions, cf. section 4.3. In Sesterhenn et al. 1993 [44], three different outflow boundary conditions are tested. Relevant for comparison is the scheme derived from Abarbanel et al. 1989 [1] where the conservative variables ρ and ρu are extrapolated at the outlet, and with the given exit pressure determine the value of ρE. The scheme is discretized with the explicit Euler method in time with a first order spatial method analogous to Roe's scheme. Results show that the Abarbanel scheme is stable or Courant number up to $C = 1.3$.

These findings may not be directly compared to the results for the prescribed model in this thesis, due to the exact characteristic boundary conditions in comparison with the approximations detailed in section 2.2.4. Still, it is interesting to note the importance of the choice of boundary conditions when dealing with low Mach number flow with respect to the influence on the convergence history and the stability of the scheme. For further information on the influence of the boundary conditions of low Mach number flow, see Müller 1996 [36].

Although the model encounters stability issues, the convergence history in figure 5.12 shows very good convergence towards steady state with the conservative variables decaying almost ten decades during the simulation time. Additionally, the set boundary conditions of the model are satisfied as seen in the results detailing the pressure in the last cell and the relative errors of the enthalpy.

CPU times for higher order discretization at differed grid refinements are seen in table 5.20. The times provided are only for the actual simulation, not including computation of convergence history data. For the fine grid with $NJ = 3200$, simulation including the convergence history data takes approximately 1 hour. The simulations are performed using MATLAB 2018 on a stationary computer with a base speed of 3.4 GHz and 4 cores.

Table 5.20: CPU time [s] for simulation of low Mach number CDN flow for specific grid refinements.

NJ	100	200	400
Higher order	1.8652	22.6179	59.0861

In conclusion, the model with steady boundaries discretized with SSP Runge-Kutta time-stepping and MUSCL fluxes yields a verified solution of the low Mach number flow in a converging-diverging nozzle due to the high level of agreement with the exact analytical solution. This is an important result which points to the model's ability to resolve respiratory flow, as physically the airway flow is in the low Mach number regime.

5.4 Test case: Oscillating flow for a constant cross-sectional area

To model the respiratory cycle, the unstable boundary conditions described in section 4.3 are taken into account. Simulation of a respiratory cycle is, as discussed, driven by a varying pressure in the rightmost cell of the domain. This is done, as presented in section 4.3.3, by implementing the boundary conditions as ghost cells on either side of the domain. Thus, in the last cell, the pressure is varied with a sine-function to generate oscillating flow simulating both inspiratory and expiratory flow through the domain. The ratio of specific heats is set to 1.4 for air at standard properties. The solution is obtained with explicit Euler time-stepping with the Rusanov method.

5.4.1 Setup

In order to focus on the flow phenomena and mechanics of the respiratory flow cycle, the variables in this test case are dimensionless. Therefore, the initial stagnation condition, which dictates the values of the left ghost cell $\mathbf{U}_1$, is set as presented in table 5.21.

Table 5.21: Initial stagnation condition for oscillating low Mach number flow.

ρ_0	u_0	p_0
1	0	1

At the right-hand side of the domain, the time-dependent stagnation pressure of the lung is modeled by the sine-function discussed in section 4.3.3. In keeping with the physics of respiratory flow, the flow is kept in the low Mach number regime controlled by the domain of the pressure relation, yielding $\frac{p_{amb}}{p0} \in [0.990, 1]$. For this reason, the pressure amplitude of the sine-function is set as $\delta p = 0.01$ yielding the correct flow regime. The angular frequency of the sine-function is chosen as $\omega = 2\pi$, yielding the frequency, and thus the period of the function, to be $f = \frac{\omega}{2\pi} = 1$. Hence, the flow completes one cycle of respiratory flow at $t = 1$. This yields the pressure function as follows

$$p_{NJ} = p_0 - \sin(2\pi t)0.01 \, .$$

The values of the right ghost cell $\mathbf{U}_{NJ}$ are thus accounted for.

The geometry is in this case kept constant with the cross-sectional area determined as $A(x) = 1$. The domain of the problem is determined by $x \in [0, 1]$.

The grid and simulation values are determined following section 4.2.1. For NJ cells the spatial step size yields $\Delta x = \frac{1}{NJ}$ due to the grid domain. The maximal spectral radius is found heuristically to be $SR = 1.18$, and thus initially set to 1.2. The Courant number is initially set to 1 as no stability issues are found and the solution is stable for the expected CFL condition $C \leq 1$ when the explicit Euler method with the Rusanov method is used for discretization. The temporal step size Δt and the number of time steps NT for simulation of one cycle with $t_{end} = 1$ are found through the relations given in section 4.2.1. This yields the initial flow and grid variables found in table 5.22.

Table 5.22: Initial flow and grid variables for simulation of oscillating low Mach number flow.

NJ	Δx	C	SR	t_{end}	Δt	NT
100	0.01	1	1.2	1	0.0083	121

5.4.2   Results

The results of the simulation are shown in figure 5.14, where the subfigures show the pressure and the Mach numbers at different times in order to visualize the cyclic respiratory flow. In all the subfigures, the values in the ghost cells at $j = 1$ and $j = NJ$ are illustrated in red. These results show the values of the boundaries representing the surroundings and the lung driving the flow. The values in the ghost cells are not physical

At time equals zero, as seen in figures 5.14a and 5.14b, the initial stagnation condition determines the flow, thus the flow, as observed, is at rest. Due to the period of the sine-function of the pressure driving the flow, the inspiratory flow is seen in the time-span $t \in [0, 0.5]$ and the expiratory flow is seen in the time-span $t \in [0.5, 1]$.

In figures 5.14c and 5.14d, the pressure and the Mach number at time $t = 0.25$ are shown, respectively. It is observed that as the pressure at the right boundary decreases below the stagnation pressure at the left boundary, a rarefaction wave is generated traveling towards the left. Consequently, the velocity of the flow increases, which is illustrated by the increase seen for the Mach number. The flow is traveling in the positive x-direction simulating inspiratory flow.

At time $t = 0.5$ the sine-function varying the pressure has completed a half period, and the pressure at the right boundary is equal to the stagnation pressure at the left boundary. In figures 5.14e and 5.14f, the tail of the expansion wave initiated by the pressure decrease is observed. The simulation of the inspiratory flow is thus complete.

The sine-function now increases after $t = 0.5$, thus increasing the pressure at the right boundary above the stagnation pressure at the left boundary. This generates a rarefaction wave traveling towards the right simulating expiratory flow, as seen in figure 5.14g. The flow velocity is now negative representing that the flow is traveling in the negative x-direction, i.e. towards the left, out of the lungs and into the surroundings through the nose. Subsequently, the Mach number at time $t = 0.75$, when the pressure at the right boundary has peaked, is negative, indicating flow in the negative x-direction. The physical value of the Mach number will be the absolute value.

At time $t = 1$, the pressure at the right boundary again equals the stagnation pressure at the left boundary and thus one cycle of respiratory flow is complete. As seen in figures 5.14i and 5.14j, a tail of the expansion wave moving toward the right is captured.

As time continues after $t = 1$, the pressure at the right boundary will again decrease and later increase as already observed. The flow will thus continue to move in the positive and the negative x-direction in cycles, just as does respiratory flow.
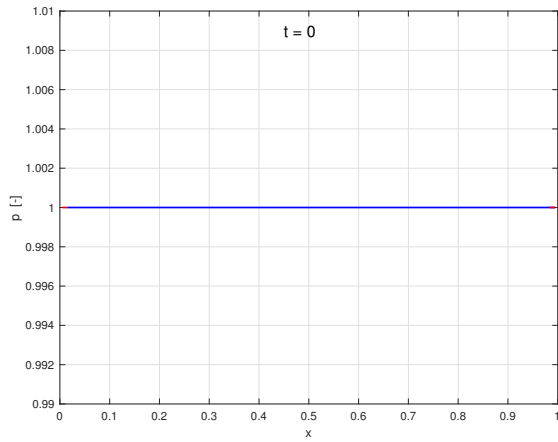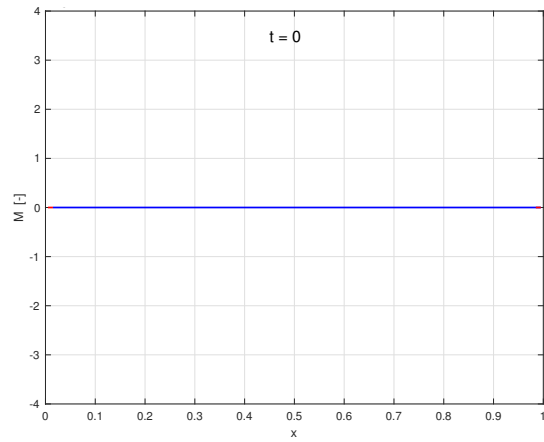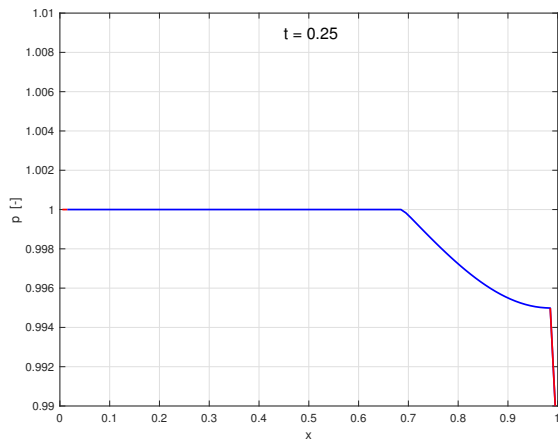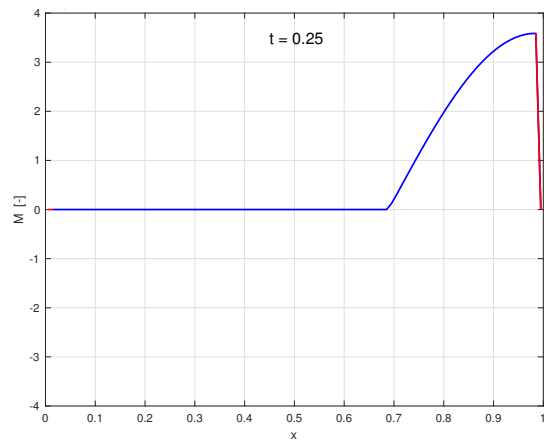
(a) Pressure t=0

(b) Mach number $\times 10^{-3}$ t=0

(c) Pressure t=0.25

(d) Mach number $\times 10^{-3}$ t=0.25
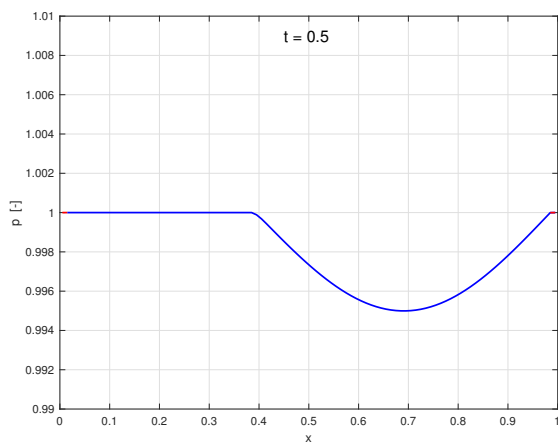
(e) Pressure t=0.5

(f) Mach number $\times 10^{-3}$ t=0.5

Figure 5.14: Results for oscillating flow with a constant cross-sectional area.
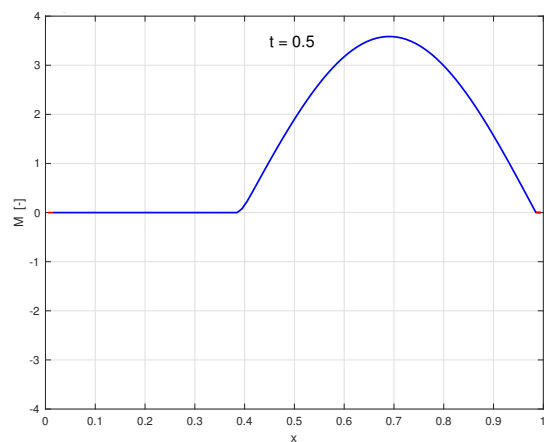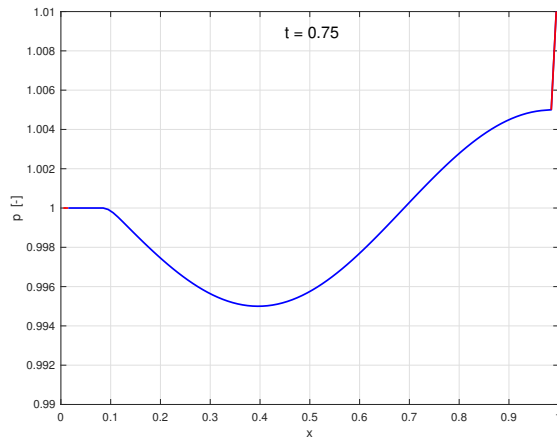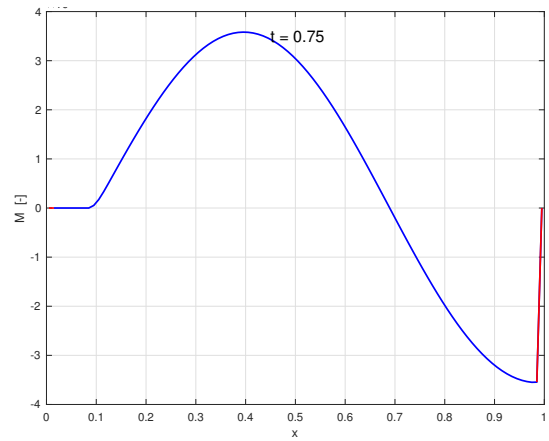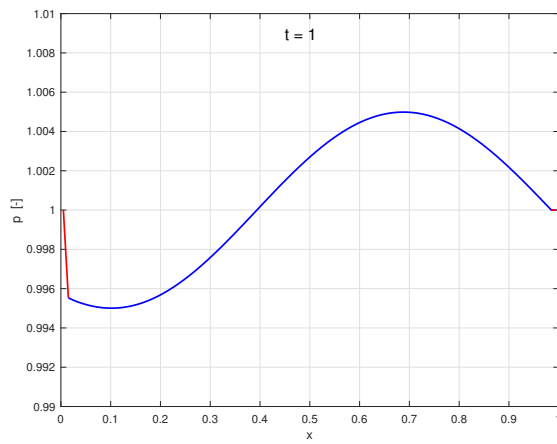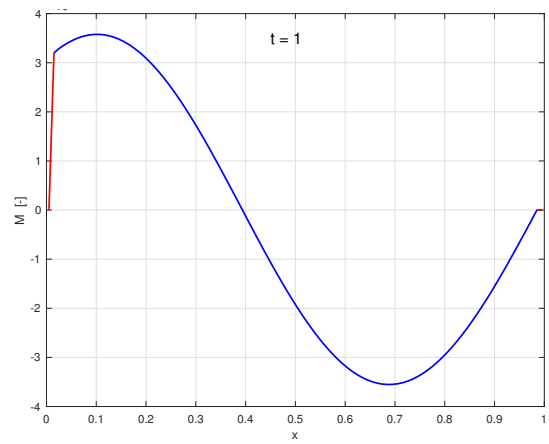
(g) Pressure t=0.75

(h) Mach number $\times 10^{-3}$ t=0.75

(i) Pressure t=1

(j) Mach number $\times 10^{-3}$ t=1

Figure 5.14: Results for oscillating flow with a constant cross-sectional area.

5.4.3 Discussion

As seen from the results described above, the model with unsteady boundary conditions discretized with first order methods applied to a domain with a constant area yields a solution where the expected flow phenomena are observed. The simulations performed manage to detail both the inspiratory and expiratory flow phases as determined by the varying pressure boundary condition at the right domain boundary. It is important to note that the negative values of the Mach number are not physical, but stem from the negative velocity obtained when the flow is moving in the negative x-direction, i.e. out from the respiratory system, and is shown as a negative value for illustrative purposes.

The expected flow features are observed with a grid of 100 cells, indicating that the spatial resolution issues encountered when the model is applied to a converging-diverging nozzle, as in test cases 5.2 and 5.3, have been resolved. Furthermore, the stability condition is as expected for explicit Euler method with Rusanov fluxes when applied to the 1D Euler equations with the CFL condition yielding stability for $C \leq 1$. In contrast to the CDN test cases, the constant cross-sectional area effectively eliminates the source term of the model due to the discretization of the area term as seen in section 4.2. This speaks to the fact that the source term is thought to be one of the reasons for the stability issues found for stable CDN flow.

For realistic modeling of respiratory flow, there is little agreement found in the reviewed literature regarding the choice of how to model the unsteady boundary conditions of the breathing cycle. As stated in the literature review 1.1.3, Calay et al. 2002 [2] argue that because of the lack of information regarding the specific pressure variations in the lung, a pressure boundary condition is not a good choice for modeling the unsteady respiratory flow. Instead, the article argues that a velocity boundary condition based on measurements of the tidal volume is a better choice due to the option of validation with in vivo measurements. On the other hand, a more recent publication by Lee et al. 2010 [30] finds that a pressure boundary condition yields results that show ample agreement with a target time-varying flow rate acquired by in vivo measurements. Physically, the time-varying tidal volume, velocity, and pressure are linked through the Boyle-Mariotte law as described in section 1.1.1. As more data is obtained from in vivo measurements, the choice between different time-dependent boundary conditions for realistic modeling of respiratory flow may become more clear, or at least be further researched. For the purpose of this thesis, however, the choice of a time-dependent stagnation pressure boundary condition seems a reasonable choice for a first, simple model due to the high level of agreement between simulated results and the expected flow phenomena.

The choice to vary the oscillating boundary condition following a sine-function is in accordance with the reviewed literature [33][30][21][38]. In Lee et al. 2010 [30], a satisfactory level of agreement between the simulated flow rate generated by the sinusoidal pressure boundary condition and patient specific measurement data is found.

The variable choice for the angular frequency, and thus the period of the sinusoidal cycle, is here determined with non-dimensionality and visibility in mind. Tidal volume values and frequencies of breath may be measured with in vivo methods yielding realistic properties for the unsteady boundary condition, as found in Rubenstein et al. 2016 [43] and Naftali et al. 1998 [38]. In vitro measurements can also detail expected flow velocities for different flow rates as in Engelhardt et al. 2016 [7]. Generally, there is agreement that the frequency of breath is 12-15 cycles per minute at normal breathing conditions. In

accordance with literature, the average tidal volume moved during one cycle of breath is $v_T = 500$ ml yielding an approximate average flow rate of $6000 - 7500$ ml min^{-1} [30][43][38]. For further development of the proposed respiratory flow model, more realistic dimensional variables for the unsteady boundary conditions could be implemented. In addition, the choice to use a time-varying pressure boundary condition could be revisited. If accurate in vivo or in vitro measurement data of the pressure variation in the lungs becomes more easily available, a more realistic pressure boundary condition could be obtained and potentially validated. Otherwise, the use of the tidal volume or the flow velocity for the varying boundary condition might be considered.

Although many respiratory flow models only pertain to steady flow, the study discussed in 1.1.3 by Hörschler, Schröder et al. 2010 [20], shows discrepancies between results obtained from steady solution and those obtained from unsteady simulations when compared with experimental data. In addition, Lee et al. 2010 [30] find a magnified difference for flow characteristics in the expiration phase when comparing steady and unsteady models. For this reason, it may be concluded that although steady models of inspiratory and expiratory flow yield useful results, the goal of a comprehensive complete model for respiratory flow must include unsteady boundary conditions such that the flow phenomena occurring at the transition from inspiration to expiration are included.

Overall, the proposed model with an unsteady pressure boundary condition yields solutions exhibiting the expected flow phenomena when applied to a simple geometry with a constant area. For this reason, it may be concluded that the proposed model with unsteady boundary conditions is a good first step towards a more complex and comprehensive model for simulation of cyclic respiratory flow.

6 | Conclusions

The objective of this thesis is to research respiratory flow, its modeling, and simulation, to propose and implement a simplified model including initial and boundary conditions, and to compare simulation results of the proposed model with the discussed literature.

The proposed model is governed by the compressible quasi-1D Euler equations where the source term is evaluated exactly. A simple initial geometry of a converging-diverging nozzle is implemented with initial stagnation conditions. Boundary conditions for steady and unsteady flow simulation are presented. The steady flow is determined by a given pressure outflow condition, and the unsteady flow is governed by a time-varying stagnation pressure condition. The model is evaluated in four test cases: **a)** a Sod shock tube, **b)** a converging-diverging nozzle with steady transonic flow, **c)** a converging-diverging nozzle with steady low Mach number flow, and **d)** a constant area with unsteady oscillating flow.

a) The implementation of the governing equations is verified by comparison with the solutions of the 1D Euler equations when applied to the classical Sod shock tube problem. The quasi-1D model for a constant cross-sectional area with simple extrapolation boundaries exhibits a near perfect agreement with the results from the 1D flow equations. It can be concluded that the governing equations of the proposed model solve a classical flow problem with a high level of accuracy when compared with standard 1D flow equations.

b) The proposed model with initial stagnation conditions and steady boundary conditions is applied to a converging-diverging nozzle with transonic steady flow. The geometry of the nozzle and the chosen ambient pressure to stagnation pressure ratio is found in Slater 2008 [46]. The performance of the model is analyzed by comparison with the exact analytical solution of the Laval nozzle. Simulations are performed with both first order and higher order discretization methods, in this case, the explicit Euler method with the Rusanov scheme and the SSP Runge-Kutta method with MUSCL extrapolated conservative variables. For both first and higher order discretization, the expected grid convergence rate is observed. There is, however, a strong spatial dependency yielding large relative errors for coarser grids, especially for the first order method. The imposed steady boundary conditions are satisfied for both discretization methods. Accurate results with relative errors lower than 1% when compared with the exact solution are obtained for 3200 and 800 cells for the first order and higher order discretizations, respectively. Stability issues indicating a smaller stability range than expected are found for both discretizations and are thought to stem from the source term and its discretization. Due to the accuracy of the simulation results for the higher order discretization in comparison to the exact analytical solution, verification of the model with steady boundaries for transonic flow with a varying cross-sectional area is obtained.

c) The proposed model with initial stagnation conditions and steady boundary conditions is also applied to a steady low Mach number flow in a converging-diverging nozzle. The simulated results are compared with the exact analytical flow solution. The discretization is done with the higher order SSP Runge-Kutta method with MUSCL extrapolation

of the conservative variables. Simulation results find a very high level of accuracy when compared to the exact solution. Relative errors under 1% for a grid with 100 cells are obtained, thus the model applied to steady low Mach number flow performs much better than when applied to transonic steady flow. The expected grid convergence rate is achieved and possible rounding errors are observed for the finer grids. As for the transonic case, the steady low Mach number case also exhibits some stability issues likely due to the source term. Additionally, jumps in the errors of primitive variables are observed, possibly caused by discontinuities in the first derivatives of the area function. The imposed boundary conditions are satisfied when the solution converges toward steady state. Comparisons to work by Sesterhenn et al. 1993 [44] are discussed and conclude that characteristic boundary conditions could potentially improve the results for low Mach number flow. The small relative errors found in comparison to the exact flow solution yield verification of the proposed model with steady boundary conditions as an appropriate flow solver for low Mach number flow with a varying a cross-sectional area.

d) The proposed model with initial stagnation conditions and unsteady boundaries is applied to a low Mach number flow with a constant cross-sectional area. No exact solution for verification is available. However, the consistency of the solution with empirically expected flow phenomena may be analyzed. A rarefaction wave traveling to the left simulating inspiration, and a rarefaction wave traveling to the right simulating expiration are both observed following the sinusoidal variation of the time-dependent stagnation pressure boundary condition. The flow direction is also reflected in the value of the velocity, and subsequently the Mach number where positive values correspond to inspiratory flow and negative values visualize the expiratory flow moving in the negative x-direction. Arguments for the choice of a sinusoidal pressure boundary condition rather than a tidal volume or velocity boundary condition are given and discussed. Significant accordance between a sinusoidal time-varying pressure boundary and measurement data is found in the reviewed literature [21][27][30][33]. Additionally, realistic average properties of the frequency of breath and the tidal volume are discussed in comparison with the chosen dimensionless variables.

Concluding remarks: Generally speaking, the proposed model with its initial and boundary conditions for simulation of respiratory flow, is in satisfactory accordance with the exact solutions and a posteriori knowledge presented for the different test cases. The source term in the quasi-1D Euler equations seems to affect both spatial dependency and stability of the simulations when applied to test cases that include a varying cross-sectional area. For the test cases with constant areas, in which the source term is eliminated due to its discretization, these issues are not present. However, convergence towards steady state is still obtained for all the steady test cases. Although some issues are encountered, the proposed model seems an appropriate first simplified model with significant accuracy of solutions for the given test cases, and sufficient accordance of the simplifications, assumptions and the chosen initial and boundary conditions with the reviewed literature.

7 | Future outlook

Suggestions for further work and improvements for the proposed respiratory flow model are listed below:

- Both the spatial resolution issue for the first order discretization of the transonic CDN nozzle flow and the stability issues encountered for both transonic and low Mach number CDN flow should be investigated further in connection with the discretization of the source term and its influence on the overall spatial discretization. Thus, it is advised that well-balanced methods, specifically designed to deal with the unbalance between general flux discretization and source terms, are investigated further and possibly prescribed.

- In the present model, approximations of characteristic steady boundary conditions are imposed. However, for stability and accuracy purposes, it is suggested that characteristic steady boundary conditions are considered.

- From the literature review and the discussion following the oscillating flow test case, it is clear that different types of unsteady boundary conditions driving the flow may be considered. The time-varying stagnation pressure boundary condition chosen for the proposed model is not easily validated with experimental data due to in vivo measurements not being easily available at the moment. However, both in vivo and in vitro measurements of the inflow velocity and flow rate are available, thus yielding time-dependent tidal volume or velocity boundary conditions interesting. For further development of the proposed model, it is suggested that the different types of unsteady boundary conditions are considered and simulation results compared.

- To achieve a more comprehensive and realistic model, it is suggested that transport phenomena in the airways are taken into account. A first step could be to adjust the model to account for the change in the molar mass of the air that happens during the respiratory cycle as oxygen is exchanged with alveoli in the lungs and carbon dioxide is removed, thus affecting the mass continuity. Secondly, other transport phenomena such as heat and moisture exchange with the flow in the turbinates in the nasal cavity might be considered.

- A large step toward gaining a more realistic model would be to implement a more complex and physical geometry. A first step could be to focus on just one part of the airways, such as the central airways, with simplifying assumption. For later work, it is recommended to extract geometric information from CT images, as seen in the literature review. Once an otherwise comprehensive model is in place, it is suggested to extend the model to 3D.

Bibliography

[1] ABARBANEL, S., DUTH, P., AND GOTTLIEB, D. Splitting methods for low Mach number Euler and Navier-Stokes equations. *Computers and Fluids 17*, 1 (1989), 1–12.

[2] CALAY, R. K., KURUJAREON, J., AND HOLDØ, A. E. Numerical simulation of respiratory flow patterns within human lung. *Respiratory Physiology and Neurobiology 130* (2002), 201–221.

[3] CALMET, H., GAMBARUTO, A. M., BATES, A. J., VÁZQUEZ, M., HOUZEAUX, G., AND DOORLY, D. J. Large-scale CFD simulations of the transitional and turbulent regime for the large human airways during rapid inhalation. *Computers in Biology and Medicine 69* (2016), 166–180.

[4] CENGEL, Y. A., AND CIMBALA, J. M. *Fluid Mechanics: Fundamentals and Applications*, 3rd ed. Mc Graw Hill Education, Boston, 2014. SI units.

[5] DAWSON, J. Solution to exercise 9 - TEP4135: Engineering Fluid Mechanics, NTNU, 2014.

[6] EITEL, G., FREITAS, R. K., LINTERMANN, A., MEINKE, M., AND SCHRÖDER, W. Numerical simulation of nasal cavity flow based on a lattice-Boltzmann method. In *New Results in Numerical and Experimental Fluid Mechanics VII. Notes on Numerical Fluid Mechanics and Multidisciplinary Design*, A. Dillmann, G. Heller, M. Klaas, H.-P. Kreplin, W. Nitsche, and W. Schröder, Eds., vol. 112. Springer, Berlin, Heidelberg, 2010, ch. Biomedical Flows, pp. 513–520.

[7] ENGELHARDT, L., RÖHM, M., MAVOUNGOU, C., SCHINDOWSKI, K., SCHAFMEISTER, A., AND SIMON, U. First steps to develop and validate a CFPD model in order to support the design of nose-to-brain delivered biopharmaceuticals. *Pharmaceutical Research 33*, 6 (2016), 1337–1350.

[8] FEDKIW, R. *Lecutre notes on TVD RK*. CME 306/CS 237C: Numerical Solution of Partial Differential Equations, Standford University, 2005. http://web.stanford.edu/class/cs237c/Lecture2.pdf.

[9] FINCK, M., HÄNEL, D., AND WLOKAS, I. Simulation of nasal flow by lattice Boltzmann methods. *Computers in Biology and Medicine 37*, 6 (2007), 739–749.

[10] FREDERICH, O., AMTSFELD, P., HYLLA, E., THIELE, F., PUDERBACH, M., KAUCZOR, H.-U., WEGNER, I., AND MEINZER, H.-P. Towards numerical simulation and analysis of the flow in central airways. In *New Results in Numerical and Experimental Fluid Mechanics VII. Notes on Numerical Fluid Mechanics and Multidisciplinary Design*, A. Dillmann, G. Heller, M. Klaas, H.-P. Kreplin, W. Nitsche, and W. Schröder, Eds. Springer, Berlin, Heidelberg, 2010, pp. 497–504.

[11] FREITAS, R. K., AND SCHRÖDER, W. Numerical investigation of the three-dimensional flow in a human lung model. *Journal of Biomechanics 41*, 11 (2008), 2446–2457.

[12] FRITSCH, H., AND KÜHNEL, W. *Color Atlas of Human Anatomy, Vol. 2: Internal Organs*, 6th ed. Thieme, Stuttgart, 2014.

[13] GARCIA, G. J. M., RHEE, J. S., SENIOR, B. A., AND KIMBELL, J. S. Septal deviation and nasal resistance: An investigation using virtual surgery and computational fluid dynamics. *American Journal of Rhinology and Allergy 24*, 1 (2010), e46–e53.

[14] GOSSE, L. *Computing Qualitatively Correct Approximations of Balance Laws*. SEMA SIAMI Springer Series. Springer, Milano, 2013.

[15] HÄNEL, D. *Computational Fluid Dynamics I + II*. Aerodynamisches Institut, RWTH Aachen, 2017.

[16] HANSEN, A. H. S. Mach-uniform method for compressible flow simulation. Project work, NTNU, 2018.

[17] HIRSCH, C. *Numerical Computation of Internal and External flow: The Fundamentals of Computational Fluid Dynamics*, 2 ed. Butterworth-Heinemann, 2007.

[18] HÖRSCHLER, I., BRÜCKER, C., SCHRÖDER, W., AND MEINKE, M. Investigation of the impact of the geometry on the nose flow. *European Journal of Mechanics - B/Fluids 25*, 4 (2006), 471–490.

[19] HÖRSCHLER, I., MEINKE, M., AND SCHRÖDER, W. Numerical simulation of the flow field in a model of the nasal cavity. *Computers and Fluids 32* (2003), 39–45.

[20] HÖRSCHLER, I., SCHRÖDER, W., AND MEINKE, M. On the assumption of steadiness of nasal cavity flow. *Journal of Biomechanics 43* (2010), 1081–1085.

[21] ISHIKAWA, S., NAKAYAMA, T., WATANABE, M., AND MATSUZAWA, T. Visualization of flow resistance in physiological nasal respiration. *Arch Otolaryngol Head Neck Surg. 132*, 11 (2006), 1203–1209.

[22] KESSLER, R., RÜTTEN, M., AND PENNECOT, J. Simulation of the flow in a human nose. In *New Results in Numerical and Experimental Fluid Mechanics VII. Notes on Numerical Fluid Mechanics and Multidisciplinary Design*, A. Dillmann, G. Heller, M. Klaas, H.-P. Kreplin, W. Nitsche, and W. Schröder, Eds. Springer, Berlin, Heidelberg, 2010, ch. Biomedical Flows, pp. 521–528.

[23] KHARAT, S. B., DEOGHARE, A. B., AND PANDEY, K. M. Development of human airways model for CFD analysis. *Materials Today: Proceedings 5* (2018), 12920–12926.

[24] KIM, S. K., NA, Y., KIM, J.-I., AND CHUNG, S.-K. Patient specific CFD models of nasal airflow: Overview of methods and challenges. *Journal of Biomechanics 46* (2013), 299–306.

[25] KINGMAN, P. S. Overview of obstructive sleep apnea in adults, 2019. www.uptodate.com/contents/overview-of-obstructive-sleep-apnea-in-adults.

[26] KINGMAN, P. S. Patient education: Sleep apnea in adults (beyond the basics), 2019. www.uptodate.com/contents/sleep-apnea-in-adults-beyond-the-basics.

[27] KLEINSTREUER, C., AND ZHANG, Z. Airflow and particle transport in the human respiratory system. *Annual Review of Fluid Mechanics 42*, 1 (2010), 301–334.

[28] KRENKEL, L., WAGNER, C., WOLF, U., SCHOLZ, A., TEREKHOV, M., RIVOIRE, J., AND SCHREIBER, W. Protective artificial lung ventilation: Impact of an endotracheal tube on the flow in a generic trachea. In *New Results in Numerical and Experimental Fluid Mechanics VII. Notes on Numerical Fluid Mechanics and Multidisciplinary Design*, A. Dillmann, G. Heller, M. Klaas, H.-P. Kreplin, W. Nitsche, and W. Schröder, Eds. Springer, Berlin, Heidelberg, 2010, ch. Biomedical Flows, pp. 505–512.

[29] LANEY, C. B. *Computational Gasdynamics*. Cambridge University Press, 1998.

[30] LEE, J.-H., NA, Y., KIMA, S.-K., AND CHUNG, S.-K. Unsteady flow characteristics through a human nasal airway. *Respiratory Physiology and Neurobiology 172* (2010), 136–146.

[31] LEVEQUE, R. J. *Finite Volume Methods for Hyperbolic Problems*. Cambridge Texts in Applied Mathematics. Cambridge University Press, 2002.

[32] LINTERMANN, A., MEINKE, M., AND SCHRÖDER, W. Fluid mechanics based classification of the respiratory efficiency of several nasal cavities. *Computers in Biology and Medicine 43* (2013), 1833–1852.

[33] LINTERMANN, A., AND SCHRÖDER, W. A hierarchical numerical journey through the nasal cavity: from nose-like models to real anatomies. *Flow Turbulance Combust 102* (2017), 89–116.

[34] MARIEB, E. N. *Essentials of Human Anatomy and Physiology*, 7th ed. Benjamin Cummings, 2002.

[35] MISCHRA, S. *Finite volume schemes for scalar conservation laws*. Lecture Notes: Numerical methods for partial differential equations, ETH Zürich, 2014. https://www2.math.ethz.ch/education/bachelor/lectures/fs2014/other/n_dgl/chap8.pdf.

[36] MÜLLER, B. Influence of inlet and outlet boundary conditions in internal flow computations at low Mach numbers. *ECCOMAS 96; Published in 1996 in John Wiley and Sons, Ltd.* (1996).

[37] MÜLLER, B. Introduction to computational fluid dynamics. Lecture notes for the course Computational Heat and Fluid Flow, NTU, 2017.

[38] NAFTALI, S., SCHROTER, R. C., SHINER, R. J., AND ELAD, D. Transport phenomena in the human nasal cavity: A computational model. *Annals of Biomedical Engineering 26*, 5 (1998), 831–839.

[39] Oeltze-Jafra, S., Meuschke, M., Neugebauer, M., Saalfeld, S., Lawonn, K., Janiga, G., Hege, H.-C., Zachow, S., and Preim, B. Generation and visual exploration of medical flow data: Survey, research trends and future challenges. *Computer Graphics forum 38*, 1 (2019), 87–125.

[40] Peppard, P., Young, T., Barnet, J., Palta, M., Hagen, E., and Hla, K. Increased prevalence of sleep-disordered breathing in adults. *American Journal of Epidemiology 177*, 9 (2013), 1006–1014.

[41] Pletcher, R., Tannehill, J., and Anderson, D. *Computational Fluid Mechanics and Heat Transfer*, 3rd ed. CRC Press, Boca Raton, 2013.

[42] Riazuddin, V. N., Zubair, M., Abdullah, M. Z., Ismail, R., Shuaib, I. L., Hamid, S. A., and Ahmad, K. A. Numerical study of inspiratory and expiratory flow in a human nasal cavity. *Journal of Medical and Biological Engineering 31*, 3 (2011), 201–206.

[43] Rubenstein, D. A., Yin, W., and Frame, M. D. *Biofluid Mechanics - An Introduction to Fluid Mechanics, Macrocirculation, and Microcirculation*, 2 ed. Academic Press, 2016.

[44] Sesterhenn, J., Müller, B., and Thomann, H. Flux-vector splitting for compressible low Mach number flow. *Computers and Fluids 22*, 4/5 (1993), 441–451.

[45] Shapiro, A. H. *The Dynamics and Thermodynamics of Compressible Fluid Flow*, vol. I. The Ronald Press Company, New York, 1953.

[46] Slater, J. W. *Converging-Diverging Verification (CDV) Nozzle*, 07 2008. https://www.grc.nasa.gov/WWW/wind/valid/cdv/cdv.html.

[47] Slater, J. W. NPARC Alliance Verification and Validation Archive, 2015. https://www.grc.nasa.gov/WWW/wind/valid/archive.html.

[48] Thompson, P. A. *Compressible-Fluid Dynamics*. Series in Advanced Engineering. McGraw-Hill Book Company, 1972.

[49] Toro, E. F. *Riemann Solvers and Numerical Methods for Fluid Dynamics - A practial Introduction*, 3rd ed. Springer, 2009.

[50] Young, T., Palta, M., Dempsey, J., Peppard, P., Nieto, F., and Hla, K. Burden of sleep apnea: rationale, design, and major findings of the Winsonsin Sleep Cohort study. *WMJ 108*, 5 (2009), 246–249.

[51] Zachow, S., Steinmann, A., Hildebrandt, T., Weber, R., and Heppt, W. CFD simulation of nasal airflow: towards treatment planning for functional rhinosurgery. *International Journal of Computer Assisted Radiology and Surgery 1* (2006), 165–167.

[52] Zierep, J. *Theoretische Gasdynamik*, 3rd ed. G. Braun, Karlsruhe, 1976.

[53] Zwicker, D., Yang, K., Melchionna, S., Brenner, M. P., Liu, B., and Lindsay, R. W. Validated reconstructions of geometries of nasal cavities from CT scans. *Biomedical Physics and Engineering Express 4*, 4 (2018), 045022.

Appendices

A.1 Example code for transonic CDN flow discretized with the explicit Euler method with the Rusanov scheme and steady boundary conditions

Listing A.1: Transonic CDN flow - main code

```matlab
%% Transonic converging-divergning nozzle flow

%   Solution of the Quasi-1D Euler euqtions for a Laval nozzle with a given
%   geometry by the test case "Steady, Inviscid Flow in a
%   Converging-Diverging Verification (CDV) Nozzle" published by the NPARC
%   Alliance

%   Written by Anna Helene S. Hansen
%   In connection with a master thesis for NTNU Trondheim Spring 2019

%% Initialising the flow and grid for simulation

clear all;
close all;

% Global parameters
global p0
global T0
global p_amb

% User input - driving flow conditions
p0 = 10000;     % Pa
T0 = 289;       % K
p_amb = 8900;   % Pa

% Isentropic variables
gamma=1.4;
gami=gamma-1;
R = 287;
cp = gamma*R/gami;

% Initial Stagnation condition
r0 = p0/(R*T0);
u0 = 0;
c0 = sqrt(gamma*T0*R);

% Functions for simulation
fhandle1 = @ flux_ex;
fhandle2 = @ flux_ex_muscl;

% Grid initialization
x_min=0;
x_max=10;
nj= 100;
dx=(x_max-x_min)/nj;

tend=2;
CFL = 0.6; % Stability issues for higher values
sr = 600; % Chosen heuristically
```

```matlab
dt= CFL*dx/sr;
nt=ceil(tend/dt);
dt=tend/nt;

% cell midpoints
x=x_min+([1:nj]-0.5)*dx;
%cell faces
xf = (x_min:dx:x_max);

% Crosssectional area A(x) at midoints
A = zeros(nj,1);
for i = 1:nj
    if x(i) <= 5.0
      A(i) = 1.75 - 0.75 * cos( ( 0.2 * x(i) - 1.0 ) * pi );
    else
      A(i) = 1.25 - 0.25 * cos( ( 0.2 * x(i) - 1.0 ) * pi );
    end
end

% at faces
Af = zeros(nj+1,1);
for i = 1:nj+1
    if xf(i) <= 5.0
      Af(i) = 1.75 - 0.75 * cos(( 0.2 * xf(i) - 1.0 ) * pi );
    else
      Af(i) = 1.25 - 0.25 * cos(( 0.2 * xf(i) - 1.0 ) * pi );
    end
end


% Initial condition for convservative solution vector
U = zeros(nj,3);
U(:,1) = r0;
U(:,2) = r0*u0;
U(:,3) = (p0/gami)+ 0.5*r0*u0^2;
U0 = U;

% Setup of solution vector UA
Am = kron(A,ones(1,3));
UA = U0.*Am;

%% Simulation
for n=1:nt
  % time
  t=(n-1)*dt

  % numerical simulation
  UA=explicit_euler(fhandle1, nj, dx, dt, t, UA, A, Af);

  %{
  % cfl stability check for every time step
  pA = gami*(UA(:,3)-0.5.*UA(:,2).^2./UA(:,1));
  c = sqrt(gamma*pA./UA(:,1));
  cfl(:,n) = (abs(UA(:,2)./UA(:,1)) +  c)*dt/dx ;
  %}

  % variables needed to check convergence history, nj*nt matrices
  R_c(:,n) = UA(:,1)./A;
  RU_c(:,n) = UA(:,2)./A;
  RE_c(:,n) = UA(:,3)./A;

end

disp(['U_computed_for_nj_=',num2str(nj)])

%% Check convergence

NT = nt;
dR = R_c(:,2:NT)-R_c(:,1:NT-1);
dR_norm = sqrt(dx*sum(dR.^2,1));
```

```
dRU = RU_c(:,2:NT) − RU_c(:,1:NT−1);
dRU_norm = sqrt(dx*sum(dRU.^2,1));
dRE = RE_c(:,2:NT)−RE_c(:,1:NT−1);
dRE_norm = sqrt(dx*sum(dRE.^2,1));
x_norm = (1:1:NT−1);

%% Post−processing

% Solution vector without area
U = UA./Am;

% primitive variables
r = U(:,1);
u = U(:,2)./U(:,1);
p = gami*(U(:,3)−0.5.*U(:,2).^2./U(:,1));
c = sqrt((gamma*p./r));
M = u./c;

% stability check
SR = abs(u) + c;
C = (u+c).*dt./dx;
C_max = max(C);


%% Figures
% plots of the different primitive variables may easily be produces
% EXAMPLE:

set(0,'DefaultLineLineWidth',1.5);


figure(1)
hold off
plot(x,r)
xlabel('x')
ylabel('\rho')
l=legend('Computed_solution');
title('Density')
set(l,'Fontsize',14)
```

Listing A.2: Explicit Euler time-stepping

```
% Explicit Euler method for solving Quasi−1D Euler equations
% with user specified spatial discretization

% function Unew = explicit_euler (fhandle, N, h, k, t, UA, A, Af)

% in : fhandle = spatial discretisation method for residual
%      N   =  number of cells
%      h   =  space increment
%      k   =  time increment
%      t   =  time instant
%      UA  =  solution [ rA, ruA, rEA] at old time level
%      A   = area at cell midpints
%      Af = area at cell faces


% out: Unew = solution of u_t = residual(t,U) at new time level
%             with fhandle residual discretization

 function Unew = explicit_euler (fhandle, N, h, k, t, UA, A, Af)


  Unew = UA + k*residual (fhandle, N, h, k, UA, A, Af);
```

Listing A.3: Residual

```
% Residual for solvin Quasi−1D Euler equations with source term and
% with given flux discretization methods with BCs

% function r = residual (fhandle, N, h, k, UA, A, Af)

% in : fhandle =  given flux discretization method with BCs
%       N  =   number of cells
%       h  =   space increment
%       k  =   time increment
%       UA =   solution vector [ rA, ruA, rEA] at old time level
%       A  =   area at cell midpoint
%       Af =   area at cell faces

% out: r   =   residual

function r = residual (fhandle,N, h, k, UA, A, Af)

   fl = fhandle (N, h, k, UA, A, Af);
   r = −(fl(2:N+1,:) − fl(1:N,:))./h + source(N,h,UA,A,Af);
```

Listing A.4: Source term

```
% Source terms for Quazi−1D Euler equations
% function S = source (N, h, k, UA, A, Af)

% in :
%       N  =   number of cells
%       h  =   space increment
%       k  =   time increment
%       UA =   solution [ rA, ruA, rEA] at old time level
%       A  =   area at cell midpoints
%       Af =   area at cell faces

% out: S = source

function S = source (N, h, UA, A, Af)

   S = zeros(N,3);
   gami = 0.4;
   presA=gami*(UA(:,3)−0.5.*UA(:,2).^2./UA(:,1)); %at cell midpoints

   S(:,1) = 0;
   S(:,2) = (presA./A).*(Af(2:N+1)−Af(1:N))./h; % where Af is at the cell faces
   S(:,3) = 0;
```

Listing A.5: Rusanov flux function with steady boundary conditions

```
% Rusanov flux for solving Quasi−1D Euler equations
% with steady BCs for nozzle inflow/outflow

% function flux_ex = flux_ex (N, h, k, UA, A, Af)
%
% in : N   =   number of cells
%      h   =   space increment
%      k   =   time increment
%      UA  =   solution [ rA, ruA, rEA] at old time level or previous stage
%      A   =   area at cell midpoint
%      Af  =   area at cell faces

% out: flux_ex = fluxes at all faces

function flux_ex = flux_ex (N, h, k, UA, A, Af)

    global p0
    global p_amb
    global T0

   % Input
   gamma=1.4;
```

```matlab
gami = gamma-1;
R = 287;
cp = gamma*R/gami;

r0 = p0/(R*T0);

pA=(gami)*(UA(:,3)-0.5.*UA(:,2).^2./UA(:,1)); % pA with area
sr = abs(UA(:,2)./UA(:,1))+sqrt(gamma*pA./UA(:,1)); % spectral radius
srm = max(sr(1:N-1),sr(2:N)); %A has canceled out


% Taking A exact at (j+1/2)
A_matrix = kron(A,ones(1,3));

U_tilde = UA./A_matrix; %Without A
f_tilde = flux_function(U_tilde);

% INFLOW BOUNDARY
p_in = pA(1)/A(1);
r_in = r0*(p_in/p0)^(1/gamma);
T_in = T0*(p_in/p0)^(gami/gamma);

T = max(0,T0-T_in);
u_in = sqrt(2*cp*T);

flux_ex(1,1) = r_in*u_in * Af(1);
flux_ex(1,2) = (r_in*u_in^2 + p_in) * Af(1);
flux_ex(1,3) = ((p_in/gami + 0.5*r_in*u_in^2)+p_in)*u_in * Af(1);

% INTERIOR with Rusanov
flux_ex(2:N,:) =Af(2:N).*(0.5*(f_tilde(1:N-1,:)+f_tilde(2:N,:)
              - kron(srm,ones(1,3)).*(U_tilde(2:N,:)-U_tilde(1:N-1,:))));

% OUTFLOW BOUNDARY
flux_ex(N+1,1) = f_tilde(N,1)*Af(N+1);
flux_ex(N+1,2) = ((U_tilde(N,2)^2/U_tilde(N,1)) + p_amb)*Af(N+1);
flux_ex(N+1,3) = ((p_amb/gami + 0.5*U_tilde(N,2)^2/U_tilde(N,1))
              + p_amb)*UA(N,2)/UA(N,1)*Af(N+1);
```

Listing A.6: Flux function

```matlab
% Flux function of quai-1D Euler equations

% function fl = flux_function(U)

% in :   U =   state vector [ rA, ruA, rEA]
% out:   f =   flux vector [ ruA, ru^2A + pA, (rE + p)uA ]


function f = flux_function(UA)

  gamma=1.4;
  gami=gamma-1;

  presA=gami*(UA(:,3)-0.5.*UA(:,2).^2./UA(:,1));

  f1 = UA(:,2);
  f2 = UA(:,2).^2./UA(:,1) + presA;
  f3 = (UA(:,3) + presA).*UA(:,2)./UA(:,1);
  f = [f1, f2, f3];
```

A.2   Example code for exact solution of tranonic CDN flow

Listing A.7: Main setup for exact solution

```matlab
%% Computation of exact solution for the Laval nozzle
%% Setup
% initial values
global p0
global T0
global p_amb

% User input for tranonic case- driving flow conditions
p0 = 10000;    % Pa
T0 = 289;      % K
p_amb = 8900;  % Pa

% Grid setup
nj_ex=6400;
x_max = 10;
x_min = 0;
dx_ex=(x_max-x_min)/nj_ex;

% cell midpoints
x_ex=x_min+([1:nj_ex]-0.5)*dx_ex;
%cell faces
xf_ex = (x_min:dx_ex:x_max);

% Crosssectional area A(x) at midoints
A_ex = zeros(nj_ex,1);
for i = 1:nj_ex
    if x_ex(i) <= 5.0
     A_ex(i) = 1.75 - 0.75 * cos( ( 0.2 * x_ex(i) - 1.0 ) * pi );
    else
     A_ex(i) = 1.25 - 0.25 * cos( ( 0.2 * x_ex(i) - 1.0 ) * pi );
    end
end
% at faces
Af_ex = zeros(nj_ex+1,1);
for i = 1:nj_ex+1
    if xf_ex(i) <= 5.0
     Af_ex(i) = 1.75 - 0.75 * cos(( 0.2 * xf_ex(i) - 1.0 ) * pi );
    else
     Af_ex(i) = 1.25 - 0.25 * cos(( 0.2 * xf_ex(i) - 1.0 ) * pi );
    end
end

%% Simulation
% Exact solution from isentropic flow relations
U_ex = exact_nozzle(nj_ex,A_ex,Af_ex);

%% Post processing
r_ex = U_ex(:,1);
u_ex = U_ex(:,2)./U_ex(:,1);
pres_ex = gami*(U_ex(:,3)-0.5.*U_ex(:,2).^2./U_ex(:,1));
M_ex = u_ex./sqrt(gamma*pres_ex./r_ex);

disp('Exact_solution_computed')
```

Listing A.8: Computation of exact solution

```
% Exact solution for a nozzle using isentropic relations

% Function U = exact_solution
% in:   N = number of cells
%       A = area at cell midpionts
%       Af = area at cell faces
% out:
%       U =

function U = exact_nozzle(N,A,Af)

global p0
global T0
global p_amb

% Flow variables
gamma = 1.4;
gami = gamma -1;
gamp = gamma +1;
R = 287;
cp = gamma*R/gami;

% stagnation properties
r0 = p0/(R*T0);
c0 = sqrt(gamma*p0/r0);

% Calculation of critical area from the exit values
M_e = sqrt(((p_amb/p0)^-(gami/gamma)-1)*2/gami);
A_crit = Af(N+1)/( 1/M_e * (1 + (gami/(gamma+1))*(M_e^2-1))^((gamma+1)/(2*gami)));


% Get out M(x) and therefore T(x), p(x), r(x) and u(x) - and construct U
% matrix from these vectors
M = mach(N,A,A_crit);
f = (1 + 0.5*gami*M.^2).^-1;
T = T0 * f;
p = p0 * f.^(gamma/gami);
r = r0 * f.^(1/gami);
u = sqrt(gamma*R.*T).*M;

U1 = transpose(r);
U2 = transpose(r.*u);
U3 = transpose(p./gami + 0.5*r.*u.^2);

U = [U1,U2,U3];
end

function M = mach(N,A,A_crit)
gamma = 1.4;
gami = gamma-1;

M_low = 0;
M_high = 1;
tol = 10^-5;

for n = 1:N
    fun = @(M) 1/M * (1 + (gami/(gamma+1))*(M^2-1))^((gamma+1)/(2*gami))*A_crit/A(n) - 1;
    M(n) = bisection(fun,M_low,M_high,tol);
end

end
```

Listing A.9: Bisection method

```
function  m = bisection(f, low, high, tol)

% Evaluate both ends of the interval
y1 = feval(f, low);
y2 = feval(f, high);
i = 0;

% Display error and finish if signs are not different
if y1 .* y2 > 0
    disp('Have_not_found_a_change_in_sign._Will_not_continue...');
    m = 'Error'
    return
end

% Work with the limits modifying them until you find
% a function close enough to zero.

while (abs(high - low) >= tol)
    i = i + 1;
    % Find a new value to be tested as a root
    m = (high + low)./2;
    y3 = feval(f, m);
    if y3 == 0
        %fprintf('Root at x = %f \n\n', m);
        return
    end

    % Update the limits
    if y1 .* y3 > 0
        low = m;
        y1 = y3;
    else
        high = m;
    end
end
```

A.3 Risk evaluation

Risk evaluation is not applicable for this strictly theoretical work.